

## AN ABSTRACT OF THE PROJECT REPORT OF

Lucas Thompson for the degree of Master of Science in Civil Engineering presented on June 8, 2018.

Title: Structural Effects of Hydraulic Loading and Drainage of Ecoroofs and Preliminary Consideration of Associated Design Loading Scenarios

Abstract approved:

---

Christopher C. Higgins

As ecoroofs have become more widespread throughout the U.S., it has become increasingly important to understand their structural behavior. The purpose of this research was to investigate the load effects exerted on a roof structure with an ecoroof during rain events and the subsequent drainage period, with the intention of using this information in the development of a structural specification for the design of ecoroofs. Research consisted of the construction of a full-scale ecoroof specimen, with a slope of 0.25/12, which was subjected to four tests where structural behavior was observed. Two tests investigated structural effects while the ecoroof freely drained, and two observed the structural effects while the drain was blocked and water was impounded on the ecoroof. Following experimental

research, a model was used to investigate the second-order effects associated with hydraulically loaded ecoroofs, and a moment amplification factor was developed to aid in the consideration of second-order effects during the ecoroof structural design process. Experimental results showed that structural responses were minimal during events where free drainage occurred. Analytical results showed that the moment amplification for sloped hydraulically loaded roofs converges towards the moment amplification value associated with a flat roof with the same structural characteristics as the height of the impounded water on the roof increases. Additionally, second-order moment amplification is inversely related to  $EI/L^4$ . Recommendations for design center around the adaptation of a new load category, termed a transient water live load, which accounts for the difference in load between the ecoroof at a drained state, and at a saturated state.

©Copyright by Lucas Thompson  
June 8, 2018  
All Rights Reserved

Structural Effects of Hydraulic Loading and Drainage of Ecoroofs and Preliminary  
Consideration of Associated Design Loading Scenarios

by  
Lucas Thompson

A PROJECT REPORT

submitted to

Oregon State University

in partial fulfillment of  
the requirements for the  
degree of

Master of Science

Presented June 8, 2018  
Commencement June 2018



Master of Science Project Report of Lucas Thompson presented on June 8, 2018

APPROVED:

---

Major Professor, representing Major Name

---

Head of the School of Civil and Construction Engineering

---

Dean of the Graduate School

I understand that my project report will become part of the permanent collection of Oregon State University libraries. My signature below authorizes release of my project report to any reader upon request.

---

Lucas Thompson, Author

## ACKNOWLEDGEMENTS

That this report is finished is due to much outside support that I've received over the duration of this research. I would first like to thank my advisor, Dr. Chris Higgins, for his advice, insight, and for helping me see the forest for the trees. Dr. Judy Liu and Dr. Andre Barbosa, the remaining members of my committee, were flexible and accommodating, and for that I am very appreciative. In addition to Dr. Higgins, I would like to thank Jeff Gent for his construction wiles and expertise; because of him I have become firmly acquainted with the wisdom of selecting the right tool for the job. Chris Reinhardt's advice was invaluable as I quickly familiarized myself with the basics of sprinkler system design.

This project was not a one-man effort, for which I am very grateful, so I would also like to extend my deepest thanks to Ben Carroll, Parker Murphy, Spenser Maunu, Lance Parson, and Hunter Anderson for their willingness to partake of the misery that is hammer-drilling. Nico Matus, although he arrived too late to get sucked into the morass of construction efforts, was always available for beer and commiseration, a truly important function. And Sharoo Shrestha, for sticking it out for two years with me in the lab, some excellent advice when I was unsure how to proceed with this report, and for helping with what had to be the worst concrete pour west of the Mississippi in 2016.

Finally, to my parents, Shawn and Carrie, and sister, Kelsey, along with Patrick Beaulieu-Hardin, Parker Malenke, and Max Kleger, thank you for being an open ear, at times a necessary distraction, and reminding me of the reasons to succeed.

## TABLE OF CONTENTS

LIST OF FIGURES .....	xi
LIST OF TABLES.....	xiii
LIST OF APPENDIX FIGURES.....	xiii
LIST OF APPENDIX TABLES .....	xiv
CHAPTER 1-INTRODUCTION.....	1
1.1 – Ecoroof Background.....	1
1.2 – Purpose of Research .....	1
1.3 – Outline of Work Completed.....	3
CHAPTER 2-BACKGROUND.....	5
2.1 – Ecoroof Background.....	5
2.1.1 Ecoroof History .....	5
2.1.2-Ecoroof Classifications.....	6
2.1.3-Extensive Ecoroofs.....	6
2.1.4-Intensive Ecoroofs.....	7
2.1.5-Semi-Intensive.....	8
2.1.6-Typical Extensive Ecoroof Cross-Section .....	9
2.1.7-Growing Substrate.....	10
2.1.8-Filter Fabric.....	10
2.1.9-Drainage Layer.....	10
2.1.10-Insulation .....	11
2.1.11-Root Barrier.....	11
2.1.12-Waterproofing .....	12
2.1.13-Investigated Benefits .....	12
2.1.14-Mitigation of the Urban Heat Island Effect.....	12
2.1.15-Stormwater Management.....	13
2.1.16-Air Quality .....	14
2.2 – Ecoroof Loads Background.....	15
2.2.1-Ecoroof Dead and Live Loads.....	15
2.2.2-Ecoroof Rain Loads.....	17
2.2.3-Load Combinations Involving Rain Loads .....	18

2.2.4-Ponding.....	19
CHAPTER 3-EXPERIMENTAL DESIGN AND METHODOLOGY.....	24
3.1 – Ecoroof Structural System Construction.....	24
3.1.1-Ecoroof Structural System .....	24
3.1.2-Lateral Bracing.....	25
3.1.3-Parapet Walls .....	27
3.2 - Ecoroof Component Selection .....	28
3.3 - Sprinkler System Design and Construction .....	33
3.4 – Instrumentation.....	37
3.4.1-Strain Gages .....	37
3.4.2-Strain Gage Data Analysis Process .....	39
3.4.3-Notes on the East and West Beams .....	41
3.4.4-Calculation of Moment and Shear Using Strain Gage Pairs .....	41
3.4.5-String Pots.....	42
3.4.6-Flow Meter.....	43
3.4.7-Soil Moisture Sensors.....	44
3.4.8-Water Level Sensors.....	44
3.4.9-Outflow Measurement .....	44
3.4.10-End Rotation Sensor.....	44
3.5-Ecoroof Dead Load Determination .....	45
3.6 – Loading Calibration.....	45
3.7-Ponding Tests.....	46
3.7.1-Ponding: Unevenly Distributed Water.....	46
3.7.2-Ponding: Evenly Distributed Water.....	47
3.8-Rain Events.....	48
3.8.1-Natural Rain Event .....	48
3.8.2-Simulated 1-hr Design Rain Event .....	48
3.9-Moment Amplification Factor (Beta).....	48
3.9.1-Moment Amplification Factor Introduction.....	48
3.9.2-Description of Model Used to Investigate Beta .....	49
3.9.3-Derivation of Flat Roof Beta Equation.....	51

3.9.4-Calculation of Experimental Beta .....	55
CHAPTER 4-DRAINAGE TESTING RESULTS .....	56
4.1-Program of Testing.....	56
4.2 – General Discussion .....	56
4.3-Water Level .....	60
4.4-Soil Moisture Content .....	63
4.4.1-Moisture Sensor Calibration .....	63
4.4.2-Soil Moisture Content.....	63
4.1 – Displacements .....	72
4.1.1-Primary Beam Displacements .....	72
4.1.2-Midspan Displacements.....	77
4.1.3-Support Displacements .....	82
4.4-Primary Member Forces .....	83
4.4.1-Midspan Flange Strain and Stress .....	83
4.4.2-Midpoint Moment.....	86
4.5-Downslope End Rotation.....	90
4.6-Ecoroof Load .....	90
4.6.1-Soil Density.....	90
4.6.2-Roof Weight as a Whole.....	91
4.7-Moment Amplification (Beta).....	91
4.7.1-Beam Calibration Results .....	91
4.7.2-Flat Roof Beta .....	92
4.7.3-Sloped Roof Beta .....	93
4.7.4-Experimental Beta .....	98
Chapter 5 – Summary of Results and Conclusions .....	99
5.1-Summary of Work Done .....	99
5.2-Experimental Conclusions.....	99
5.3-Analytical Conclusions.....	100
5.4-Design Recommendations .....	101
5.5-Proposed Future Research .....	102
References .....	103

Appendix B – ASTM E2397 In-Depth Explanation and Procedure .....	118
Appendix C – Analysis and Discussion of Kim Kilroy’s Research.....	124
Appendix D – Derivation of Formula Used to Determine Mechanical Strain.....	129

## LIST OF FIGURES

Figure 1: Extensive Ecoroof atop Ford Company’s Final Assembly Building in Dearborn, MI. ( <a href="http://www.greenroofs.com/projects/pview.php?id=12">http://www.greenroofs.com/projects/pview.php?id=12</a> ) .....	7
Figure 2: Latter-Day Saint Conference Center with Intensive Ecoroof, Salt Lake City, UT. ( <a href="https://www.templesquare.com/explore/conference-center/">https://www.templesquare.com/explore/conference-center/</a> ) .....	8
Figure 3: Semi-Intensive Ecoroof at the Central Branch of the Philadelphia Free Library. ( <a href="http://www.greenroofs.com/projects/pview.php?id=1383">http://www.greenroofs.com/projects/pview.php?id=1383</a> ).....	9
Figure 4: Typical Extensive Ecoroof Cross-Section (Kilroy, Direct Shear Interface Friction and Linear Motion Shaking Response of Ecoroofs, Pg. 12).....	9
Figure 5: Drainage Panel Example ( <a href="http://interlocbuild.co.uk/shop/80-drainage-60mm-drainage-layer-tig060-black-intensive.html">http://interlocbuild.co.uk/shop/80-drainage-60mm-drainage-layer-tig060-black-intensive.html</a> ) .....	11
Figure 6: AISC Figure A-2.1 (AISC 360-10, Pg. 16.1-190) .....	21
Figure 7: AISC Figure A-2.2 (AISC 360-10, Pg. 16.1-191) .....	22
Figure 8: Ecoroof structural member double angel shear connection .....	25
Figure 9: Characteristic Winkel bearing configuration .....	26
Figure 10: Western bridging on the W12x26 beam. ....	27
Figure 11: Wooden parapet walls and supporting plates at southwest roof corner.....	28
Figure 12: Geosynthetic fiber drainage layer portion.....	29
Figure 13: Polyester filter fabric, attached to drainage layer portion.....	30
Figure 14: Retention layer portion. ....	31
Figure 15: Ecoroof plants and growing substrate. ....	32
Figure 16: Dummy irrigation system piping.....	33
Figure 17: Figure 1611.1 from the Oregon Structural Specialty Code-Map of 1-hr rainfall with 100-yr return period. (Oregon Structural Specialty Code, pg 373).....	34
Figure 18: Rainfall simulation sprinkler system nozzle configuration.....	35
Figure 19: Pressure measurement set-up. ....	36
Figure 20: Sprinkler System Pipe Configuration.....	37
Figure 21: Strain Gage Layout.....	38
Figure 22: Midpoint Flange Strain (Raw and Temperature-Adjusted) vs Time.....	40
Figure 23: 1/9 Point Flange Strain (Raw and Temperature-Adjusted) vs Time .....	41
Figure 24: String Pot Layout. ....	42
Figure 25: String Pot Pin Connection .....	43
Figure 26: Undelected Roof-Loads Used for 1st-Order Moment Calculations.....	49
Figure 27: Deflected Roof-Loads Used for 2nd-Order Moment Calculations .....	50
Figure 28: Flat Roof Second-Order Effects Free-Body Diagram .....	52

Figure 29: Example Shape 1.....	57
Figure 30: Example of Shape 2.....	58
Figure 31: Example of Shape 3.....	59
Figure 32: Example of Shape 4.....	60
Figure 33: Downslope Parapet Wall Water Elevation (Ponding Flooding Input Test).....	61
Figure 34: Downslope Parapet Wall Water Elevation (Ponding Uniform Input Test).....	61
Figure 35: Downslope Parapet Wall Water Elevation (Natural Rain Event) .....	62
Figure 36: Downslope Parapet Wall Water Elevation (Simulated 1-hr Event) .....	62
Figure 38: Non-zeroed Moisture Content vs Time (Ponding Flooding Input Test).....	64
Figure 39: Non-zeroed Moisture Content vs Time (Ponding Uniform Input Test) .....	65
Figure 40: Non-zeroed Moisture Content vs Time (Natural Event Test).....	66
Figure 41: Non-Zeroed Moisture Content vs Time (Simulated 1-hr Rain Event Test).....	66
Figure 42: Zeroed Moisture Content vs Time (Ponding Flooding Input Test).....	67
Figure 43: Zeroed Moisture Content vs Time (Ponding Uniform Input Test).....	68
Figure 44: Zeroed Moisture Content vs Time (Natural Event Test) .....	69
Figure 45: Zeroed Moisture Content vs Time (Simulated 1-hr Rain Event Test).....	69
Figure 46: Zeroed Moisture Content vs Downslope Parapet Wall Water Elevation (Ponding Flooding Input Test).....	71
Figure 47: Zeroed Moisture Content vs Downslope Parapet Wall Water Elevation (Ponding Uniform Input Test) .....	72
Figure 48: Displacement vs Time (Ponding Flooding Input Test).....	73
Figure 49: Displacement vs Time (Ponding Uniform Input Test) .....	73
Figure 50: Displacement v Time (Natural Rain Event).....	74
Figure 51: Displacement vs Time (Simulated 1-hr Rain Event).....	75
Figure 52: Displacement vs Downslope Parapet Wall Water Elevation (Ponding Flooding Input Test) .....	76
Figure 53: Displacement vs Downslope Parapet Wall Water Elevation (Ponding Uniform Input Test) .....	77
Figure 54: Midspan Displacements vs Time (Ponding Flooding Input Test).....	78
Figure 55: Midspan Displacements vs Time (Ponding Uniform Input Test) .....	78
Figure 56: Midspan Displacements vs Time (Natural Event Test).....	79
Figure 57: Midspan Displacements vs Time (Simulated 1-hr Rain Event Test) .....	80
Figure 58: Midspan Displacements vs Downslope Parapet Wall Water Elevation (Ponding Flooding Input Test).....	81
Figure 59: Midspan Displacement vs Downslope Parapet Wall Water Elevation (Ponding Uniform Input Test) .....	81
Figure 60: Support Displacements vs Time (Ponding Flooding Input Test).....	82
Figure 61: Support Displacements vs Time (Ponding Uniform Input Test).....	83
Figure 62: Midspan Bottom Flange Stress/Strain vs Time (Ponding Flooding Input Test) .....	84
Figure 63: Midspan Bottom Flange Stress/Strain vs Time (Ponding Uniform Input Test).....	84
Figure 64: Midspan Bottom Flange Stress/Strain vs Time (Natural Event Test) .....	85



Figure 65: Midspan Bottom Flange Stress/Strain vs Time (Simulated 1-hr Rain Event Test)	85
Figure 66: Midpoint Moment vs Time (Ponding Flooding Input Test)	86
Figure 67: Midpoint Moment vs Time (Ponding Uniform Input Test)	87
Figure 68: Midpoint Moment vs Time (Natural Event Test)	87
Figure 69: Midpoint Moment vs Time (Simulated 1-hr Rain Event Test)	88
Figure 70: Midpoint Moment vs Downslope Parapet Wall Water Elevation (Ponding Flooding Input Test)	89
Figure 71: Midpoint Moment vs Downslope Parapet Wall Water Elevation (Ponding Uniform Input Test)	89
Figure 72: Downslope End Rotation vs Time (Ponding Flooding Input Test)	90
Figure 73: Calibration Load Moment Distribution	92
Figure 74: Flat Roof Beta vs $EI/L^4$	92
Figure 75: Beta vs $EI/L^4$ for flat roof and roof with a slope of 0.25/12, with varying dead loads	93
Figure 76: Beta vs Secondary Drain Height for Roofs with Slope 0.25/12 and Varying Dead Loads	94
Figure 77: Deflected Shapes for a Roof with a 0.25/12 Slope, 20 and 100 psf Dead Loads, with Secondary Drain Height of 1 inch	95
Figure 78: Deflected Shapes for a Roof with a 0.25/12 Slope, 20 and 100 psf Dead Loads, with Secondary Drain Height of 5 inches	96
Figure 79: Beta vs $EI/L^4$ for Flat Roof and Roofs with 100 psf Dead Load and Varying Slope	97
Figure 80: Expanded View of Bottom-Left Corner of Figure 77	97
Figure 81: Beta vs Secondary Drain Height for Roofs with 30 psf Dead Load and Varying Roof Slopes	98

## LIST OF TABLES

Table 1: Program of Testing	3
Table 2: Description of Common Plot Appearances	57
Table 3: Soil Moisture Sensor Calibration Data	63
Table 4: Ecoroof Soil Unit Weights	91
Table 5: Ecoroof Unit Weights	91

## LIST OF APPENDIX FIGURES

Figure A 1: Northwestern connection between W40x324 and W21x111 crossbeam	106
Figure A 2: Shake Table Anchor Formation	107
Figure A 3: Linear Motion Rail on Top of and in Parallel with W40x324 Shake Table Framing Beam	109
Figure A 4: Linear Motion Rail Layout	110

Figure A 5: Linear Motion Bearing Mounted on Linear Motion Rail .....	111
Figure A 6: W12x106 Drawings, Displaying Cope and Hole Arrangement (Drawing Courtesy of Fought and Company).....	112
Figure A 7: Northern End Bearing Plate Supporting One End of a W12x106 Beam .....	113
Figure A 8: Downslope Connection Between W12x106 and W21x111 .....	114
Figure A 9: Upslope Connection between W12x106 and W21x111, with Stacking Plates to Create Roof Slope .....	115
Figure A 10: Actuator Beam Set-up and Connection .....	116
Figure A 11: Bolted Connection between Actuator Piston and Shake Table Cross-Beam	117
Figure A 12: Relative Soil Displacement vs Peak Table Velocity (from Kim Kilroy's Thesis).....	127

## LIST OF APPENDIX TABLES

Table A 1: Ecoroof Dead and Live Load Component Calculations According to ASTM E2397 .....	118
Table A 2: Direct Shear Interface Friction Testing Results for Dry and Submerged Ecoroof Components.....	124
Table A 3: Motion Type and Corresponding Mean and Maximum Average Pressures....	128

## CHAPTER 1-INTRODUCTION

### 1.1 – Ecoroof Background

According to the EPA a green roof, also known as an ecoroof for the purposes of this project report, is, most simply, “a vegetative layer grown on a rooftop” (EPA, 2017). Ecoroofs offer a variety of benefits over traditional hard roofs, including reduced stormwater quantity, avoidance of stormwater infrastructure, improved air quality, and reduced urban heat island effect (MacMullan, Reich, Puttman, & Rodgers, 2008). These benefits, in tandem with a desire to mitigate the detrimental environmental effects that accompany urban development, have led to increasingly wide adoption of ecoroofs in cities across the U.S. For example, from 2008 until 2012, Portland, Oregon offered an ecoroof incentive program that lead to the construction of more than 130 ecoroofs (Environmental Services, 2017). However, increased ecoroof usage, in combination with recent, prominent ecoroof failures, makes the state of U.S. structural design standards pertaining to ecoroofs an increasingly important topic to be addressed.

### 1.2 – Purpose of Research

Since the beginning of the decade, there have been several serious ecoroof failures that have indicated the need for further research to be conducted investigating their structural behavior. On February 13, 2011, an ecoroof section approximately 700'x50' collapsed in St. Charles, Illinois. (Fountain, 2011) The roof, which was part of what was labelled the “largest sloping green roof in North America” was initially believed to have failed due to drainage issues. (Walberg, 2011) Two and a half years later, on November 21, 2013, an ecoroof atop a supermarket in Riga, Latvia collapsed, causing more than 50 casualties. Most recently, on May 20, 2016, the 1400 m<sup>2</sup> ecoroof covering the sports center at Hong

Kong City University collapsed, due to faulty drainage allowing the buildup of excess stormwater. (Cheung, 2016)

Currently, there is no definitive standard that guides the structural design of ecoroofs in the U.S. Given the prominence and severity of these failures, it is apparent that the development of such a standard is necessary, especially due to the increasing popularity of ecoroofs in the U.S. The purpose of this research was to investigate the forces exerted on the roof structure ecoroof both during rain events and in the drainage periods that follow, in order to gain a better understanding of ecoroof behaviors that could potentially control design choices. This knowledge will then be used in the development of the aforementioned structural standard for ecoroof design.

The research in this report makes up the third phase of a four phase project that is investigating the soil properties and structural behavior of ecoroofs. Phase one was completed by Travis Kraupa, and consisted of taking soil samples from 18 ecoroofs around Portland, OR, and then characterizing said soils according to the results of static and cyclic simple shear tests, and their liquefaction potential (Kraupa, Stuedlein, Mason, & Higgins, 2016). Kim Kilroy completed the second project phase, examining the soil-system response in the presence of periodic motion. This examination took the form of two different investigations. The first of these investigations determined the coefficient of friction between the layered components that make up an ecoroof, which in turn provided insight to where and when sliding will most likely occur when an ecoroof is subject to lateral motion. The second of these investigations involved the construction of a small shake table, which was then used to subject model ecoroofs to differing lateral motions, with the intent of determining the potential and behavior of soil decoupling during seismic

events (Kilroy, 2015). Phase 4 will consist of large scale shake table tests, using the ecoroof and shake table that were constructed during the research completed for this report.

### 1.3 – Outline of Work Completed

This research began with the construction of a large, unidirectional shake table, on the southwest side of the O.H. Hinsdale Wave Research Laboratory. The ecoroof used for this phase's tests was built on top of this shake table. Further information pertaining to the design and construction of the shake table can be found in Appendix A, however, the large scale shake table tests are outside of the scope of this report, and shall not be mentioned further in the main report body. Tests were conducted on a monolithic ecoroof, wherein each layer that made up the roof covered the entire available roofing area. The ecoroof was constructed according to industry standards in order to ensure that real-world ecoroof behavior was accurately simulated. Once the ecoroof had been constructed and instrumented on the shake table, the tests detailed in Table 1 were conducted.

Table 1: Program of Testing

Test	Description
Load Calibration	A single point load of known magnitude was applied to the center roof girder. Returned instrumentation data was compared to theoretical expectations to ensure that instrumentation was functioning as expected and explore load distribution.
Ponding (Flooding Input)	The ecoroof drain was clogged to prevent drainage, and a large amount of water was collected on the roof from several output locations on the ecoroof surface. This data was used to assess the structural performance of the ecoroof in a more extreme event.
Ponding (Uniform Input)	A similar test to the above, however, water was added to the roof, using the sprinkler system built for the 1-hr rain event test, applying it uniformly over the area.
Natural	Data about the ecoroof's structural behavior was collected during the course of a natural rain event.

Rain Event Observation	
1-hr Rain Event	Sprinklers designed to deliver a set amount of precipitation, uniformly to the ecoroof area, were operated for 1-hr, and the ecoroof's structural behavior during and after this period was monitored.

After testing was complete, data was analyzed to determine the structural behavior of the roof. Additionally, a theoretical model of a hydraulically loaded roof was used to investigate second-order effects, and a moment amplification constant, hereafter called “Beta” was developed that accounted for those effects. Results from testing and the theoretical model were then themselves analyzed to determine the parameters that might control the design of a successful ecoroof structural system.

Following this introduction, Chapter 2 contains background information pertaining to ecoroofs and roof forces. Chapter 3 is a discussion of methodology, comprising examinations of the ecoroof construction, instrumentation of the ecoroof and structural elements supporting it, and the program of testing. Chapter 4 analyzes the data collected during testing, while Chapter 5 concludes this thesis with a summarization of the conclusions made from the data acquired both during testing and from the analytical model, and design recommendations that can be drawn from model and testing results, in addition to the literature review. Further research pertaining to the design of ecoroof structural systems is also suggested.

## CHAPTER 2-BACKGROUND

### 2.1 – Ecoroof Background

#### 2.1.1 Ecoroof History

Ecoroofs have been a part of the built environment in some form since ancient times. The first well-known roof gardens were the Hanging Gardens of Babylon, constructed sometime between the fourth millennium and 600 B.C.E. (Magill, Midden, Groninger, & Therrell, 2011). As time passed, ecoroofs developed to serve either an aesthetic or functional purpose. During the Renaissance, rooftop gardens were often enjoyed by the rich, or the devout. Meanwhile, as the millennium progressed sod roofs were also used in Norway, and on the American frontier to provide insulation (Magill, Midden, Groninger, & Therrell, 2011).

It was during the era of the American Frontier that the genesis of the modern ecoroof occurred in Germany, albeit, somewhat unintentionally. During the 1880s, the roofer H. Koch began placing sand and gravel over the flammable hot tar used for inexpensive roofing, in an attempt to mitigate the fire hazard. As time passed, seeds colonized the roofs, and plants sprouted (Magill, Midden, Groninger, & Therrell, 2011). Nearly a century later, in the 1970s, Germany first marketed eco roof systems on a large scale. These systems were more consciously designed than the German ecoroofs of the 1880s, and included irrigation and means to prevent plant root ingress (Jorg Breuning & Green Roof Service, LLC, 2017). After the initial establishment of the market, it grew quickly, averaging 15 to 20 percent growth a year. In 1989 1 million m<sup>2</sup> of ecoroofs had been installed, and by 1996 that number increased tenfold (Magill, Midden, Groninger, & Therrell, 2011).

Meanwhile, while ecoroofs have become more popular in the U.S. in the last couple of decades, their usage still lags behind that of European countries, like Germany, where it

has been estimated that ecoroofs make up 14% of all flat roofs (Getter & Rowe, 2006). The difference in popularity can be attributed, in part, to the lack of a developed and standardized ecoroof industry in the U.S. As mentioned in the introduction, this research aims to contribute to ecoroof standardization.

#### 2.1.2-Ecoroof Classifications

Typically, ecoroofs are classified based on the amount of growing medium or substrate present, and the types of plants that the roof can sustain. There are three general types of ecoroofs: extensive, intensive, and semi-intensive.

#### 2.1.3-Extensive Ecoroofs

Extensive ecoroofs are generally defined as ecoroofs with a planting depth of less than 6 inches (15.2 cm). They require little, if any maintenance or irrigation, and are usually populated by hardy, drought-tolerant succulents such as *Sedum*, or other grasses and herbs (Getter & Rowe, 2006), with *Sedum* being the most common vegetation choice (Magill, Midden, Groninger, & Therrell, 2011). Figure 1 shows an example of an extensive ecoroof, located at the Ford Company's final assembly building in Dearborn, MI.





Figure 1: Extensive Ecoroof atop Ford Company's Final Assembly Building in Dearborn, MI. (<http://www.greenroofs.com/projects/pview.php?id=12>)

#### 2.1.4-Intensive Ecoroofs

Intensive ecoroofs are generally defined as ecoroofs with a planting medium depth of 6 inches (15.2 cm) or greater. Due to the greater substrate depth, they can accommodate a wider variety of plants than extensive ecoroofs, such as trees and shrubs. They are often accessible to visitors, and are named due to their oftentimes "intense" maintenance requirements (Magill, Midden, Groninger, & Therrell, 2011). Figure 2 contains an example of the intensive ecoroof found atop the Latter Day Saints Conference Center in Salt Lake City, Utah.



Figure 2: Latter-Day Saint Conference Center with Intensive Ecoroof, Salt Lake City, UT.(  
<https://www.temple-square.com/explore/conference-center/>)

#### 2.1.5-Semi-Intensive

As the name implies, a semi-intensive ecoroof is a medium that amalgamates characteristics of both extensive and intensive green roofs. Semi-intensive roofs generally possess growing mediums of depths between 6 and 12 inches, and due to the increased growing medium depth in comparison to extensive ecoroofs, can accommodate a wider variety of plants, including modest shrubs. Generally, semi-intensive ecoroofs can support a more varied ecology and retain more stormwater than their extensive relatives (Jorg Breuning & Green Roof Service, LLC, 2017). The ecoroof atop the central branch of the Philadelphia Free Library is an example of a semi-extensive ecoroof, as can be seen below in Figure 3.



Figure 3: Semi-Intensive Ecoroof at the Central Branch of the Philadelphia Free Library.  
(<http://www.greenroofs.com/projects/pview.php?id=1383>)

This research concentrated on the behavior of extensive ecoroofs, because of their more widespread use, due to building weight restrictions, and extensive ecoroofs' cheaper cost in comparison their intensive brethren (Getter & Rowe, 2006).

#### 2.1.6-Typical Extensive Ecoroof Cross-Section

The components of an ecoroof, shown below in Figure 4, function to allow the development and maintenance of the plant life, while also protecting the building from outside elements, including the plants that it houses.

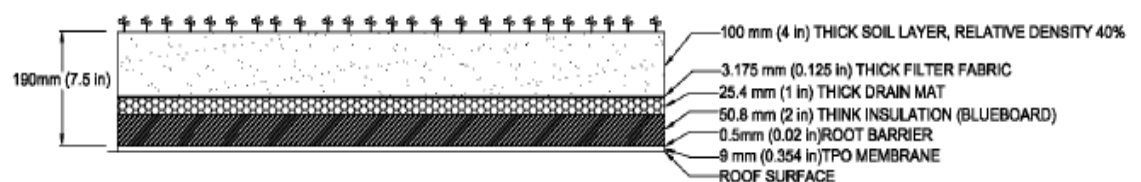


Figure 4: Typical Extensive Ecoroof Cross-Section (Kilroy, Direct Shear Interface Friction and Linear Motion Shaking Response of Ecoroofs, Pg. 12)

What follows is a brief discussion of the components that comprise an ecoroof, and their functions.

#### 2.1.7-Growing Substrate

Growing substrate is the medium that houses the plant roots. While it can be traditional soil, oftentimes it is designed to ensure that it is lightweight, in order to minimize roofing loads. It can be made up of both natural and synthetic materials, including sand, clay, pumice, gravel, crushed clay bricks, crushed or aerated concrete, strofoam, or urea-formaldehyde resin foam. (Magill, Midden, Groninger, & Therrell, 2011)

#### 2.1.8-Filter Fabric

The filter fabric serves primarily as a barrier between the growing substrate and drainage layers, preventing fine substrate particles from migrating beyond the substrate. Filter fabrics are generally cloth geotextiles (Weiler & Scholz-Barth, 2009)

#### 2.1.9-Drainage Layer

Lying below the filter fabric, the drainage layer collects, absorbs and distributes the water that filters through the growing substrate, without being subject to evapotranspiration (Weiler & Scholz-Barth, 2009). There are two prominent types of drainage layers, which can be used in tandem, or separately. A drainage mat generally is between 1/8" and 1" thick, and is made up of webbed plastic that serves to guide the flow of excess water (Weiler & Scholz-Barth, 2009). Drainage panels are the second, more complex type of drainage layer, and are a hard plastic mat containing a waffle-like array of small reservoirs that can hold excess water. There are holes in each reservoir, so that once the excess water reaches a specific elevation, it will be released into the main drainage system (Weiler & Scholz-Barth, 2009). An example of a drainage mat can be seen below in Figure 5.





Figure 5: Drainage Panel Example (<http://interlocbuild.co.uk/shop/80-drainage-60mm-drainage-layer-tig060-black-intensive.html>)

#### 2.1.10-Insulation

As with traditional roofs, ecoroofs also usually contain a layer of insulation to aid with the heating and cooling of the structure. The growing substrate can also provide insulation, however, its insulative properties can vary depending on substrate composition and moisture content (Weiler & Scholz-Barth, 2009), and it is due to these variable properties that additional insulation is often used.

#### 2.1.11-Root Barrier

Root barriers serve to protect any plant roots from piercing or penetrating the waterproofing membrane. Root barriers are commonly polyethylene sheets that reside

directly above the waterproofing membrane. Occasionally, polypropylene geotextiles are used as secondary barriers (Weiler & Scholz-Barth, 2009).

#### 2.1.12-Waterproofing

Waterproofing serves to keep moisture from penetrating the structural envelope. There are three types of waterproofing that are commonly used on low-slope green roofs: single-ply membrane, built-up membrane, or fluid applied-membrane (Weiler & Scholz-Barth, 2009). Single-ply membranes consist of a single sheet of plastic polymers, such as polyvinyl chloride (PVC) or thermoplastic olefin (TPO), adhered to the deck of the roof (Weiler & Scholz-Barth, 2009). Built-up membranes are made up of alternating layers of fiber and molten bitumen, such as polyester and asphalt (Weiler & Scholz-Barth, 2009). Finally, fluid-applied membranes are water-repellant compounds, such as asphalt emulsions or silicone, that are usually applied with sprayers or rollers. They are often used for roofs with uncommon or complex shapes, such as domes (Weiler & Scholz-Barth, 2009).

#### 2.1.13-Investigated Benefits

Aside from aesthetic pleasure, ecoroofs provide a range of benefits that have led to their increasing popularity. Some of the most prominent of these benefits, which will be discussed further, include: mitigation of the urban heat island (UHI) effect, improved stormwater management in comparison to traditional roofs, and air quality enhancement.

#### 2.1.14-Mitigation of the Urban Heat Island Effect

The Urban Heat Island (UHI) Effect, is the discrepancy between the air temperatures in an urban area and the surrounding rural locales. Urban areas have been found to be up to 5.6°C warmer than the nearby countryside (USEPA, Cooling summertime temperatures: Strategies to reduce urban heat islands. , 2003). Warmer urban temperatures are caused due to the abundance of impervious surfaces and buildings, which both prevent the cooling

effect of evapotranspiration from occurring, and also absorb more solar energy in comparison to rural ground covering (Magill, Midden, Groninger, & Therrell, 2011). According to (USEPA, Heat Island Effect, 2017), detrimental effects of UHIs include increased building cooling and energy costs, in addition to increased greenhouse gas emissions, air pollution, and heat-related illness.

Ecoroofs mitigate the UHI Effect by replacing heat-absorbing impervious surface and providing an area for plant life to develop and evapotranspire. As mentioned by (Getter & Rowe, 2006), through evapotranspiration, incoming solar energy is used to evaporate water, preventing it from becoming sensible heat. (Li, Bou-Zeld, & Oppenheimer, 2014) modelled the effects of ecoroofs on urban air temperatures in during a heat wave in the Washington D.C.-Baltimore metro area and found that if 30% of the roofs were converted to ecoroofs, the UHI Effect could be lessened by 1°C. Additionally, they found that as the proportion of ecoroofs increase, the UHI effect decreases nearly linearly (Li, Bou-Zeld, & Oppenheimer, 2014).

#### 2.1.15-Stormwater Management

In addition to the UHI Effect, stormwater runoff is another problem that is exacerbated by the impervious cover of urban areas. Where storm sewers outlet stormwater into the natural drainage basin, the excessive flow, in comparison to the flow that the basin would experience were impervious surface areas not present, can lead to flooding (Getter & Rowe, 2006). Additionally, in older urban areas with combined stormwater and sewage systems, excessive amounts of incoming stormwater can cause the sewer to overflow, and lead to sewage spilling into streams and rivers from unintentional outlets.

Ecoroofs lessen the stormwater demand on sewer systems in two ways. First, by entrapping water in the pore space present in the growing medium, lessening demand on the storm sewer. (Hutchinson, Abrams, Retzlaff, & Liptan, 2003) conducted a study for the city of Portland, OR from 2002 to 2003, in an attempt to better quantify the stormwater benefits that the roofs could provide for the city. They found that the west ecoroof retained 69% of the stormwater that fell on it, on average, over the period from January 2002 to April 2003. From this study, it can be seen that ecoroofs have the potential to significantly decrease the demand of storm sewer systems, allowing smaller and more efficient systems to be used. Second, for stormwater that is not contained in the ecoroof growing medium, it must still travel through the ecoroof growing medium and drainage layers before being passed on to the urban area's storm sewer, leading to decreased flow runoff rates. (Hutchinson, Abrams, Retzlaff, & Liptan, 2003) also measured the effect of the ecoroof on stormwater runoff. They found that for storms with peak rainfall intensities ranging from 0.041 to 0.193 cfs, peak runoff from the ecoroof ranged from 0.008 to 0.012 cfs. This decrease in flow runoff aids in keeping the watershed healthy, by lessening the erosive power of the runoff.

#### 2.1.16-Air Quality

Ecoroofs can also help increase air quality by removing pollutants from the air. (Yang, Yu, & Gong, 2008) quantified the effects of ecoroofs on air quality in the city of Chicago. After conducting a survey of the 170 ecoroofs that were then present in the city, they built a model that calculated the pollutants removed by the roofs through the process of dry deposition. It was found that the 19.8 ha of ecoroofs removed 1675 kg of pollutants. It was additionally found that if the city of Chicago completed the remaining 27.87 ha of ecoroofs that were under development, and if the proportion of intensive to extensive ecoroofs remained constant, a total of 2388 kg of pollutants could be removed from the air.



## 2.2 – Ecoroof Loads Background

### 2.2.1-Ecoroof Dead and Live Loads

One of the primary differences between ecoroofs and traditional roofs are the fluid natures of the dead and live loads between ecoroof occurrences. Planting material thickness, plant type, and soil properties can vary widely between roofs, the latter of which can be observed in the work of (Kraupa, et al, 2016). Consequently, it cannot be assumed that the presence of an ecoroof guarantees the presence of a dead load of a specified magnitude.

Compounding dead load variability, the capacity of planting material and other ecoroof components to hold water creates a live load separate from a rain load that is not considered in the design of traditional roofs.

Guidelines for calculating ecoroof dead and live loads are given in ASTM E2397/E2397M-15, Standard Practice for Determination of Dead Loads and Live Loads Associated with Vegetative (Green) Roof Systems (ASTM International, 2015). The standard defines the dead load as “the weight (of ecoroof components) under drained conditions after new water additions by rainfall or irrigation has ceased” while the “transient water live load” is the difference in weight between the aforementioned condition and “weight when rainfall or irrigation is actively occurring and the drain layer is completely filled with water” (ASTM International, 2015). All loads are calculated in units of lbs/ft<sup>2</sup>. Additionally, the standard assumes that live load will only be present in the ecoroof drain layers.

According to the standard, dead load is generally comprised of two components: unit weight of the ecoroof component, and, if the component can hold water, the unit weight of captured water. In order to determine captured water, ecoroof components are immersed in water for 15 minutes or 24 hours, depending on component. The components are then weighed after they are allowed to drain for 15 minutes or 120 minutes, respectively. Live

load is the difference in weight of the ecoroof components when they are totally saturated, or first removed from water immersion, and their weight at dead load status.

While dead and live load of granular ecoroof components, such as growth media and granular drain layers follows the principals discussed above, dead load is generally calculated by determining the density of the granular component after the aforementioned immersion and drainage process, and multiplying this density by the thickness of the component layer. Live Load is calculated by determining the available air-filled porosity (AFP) in the component, calculating the weight of water that would occupy that space, and taking the difference between the component weight at that state, and the component weight at the dead load state. ASTM E2399/E2399M-15 *Standard Test Method for Maximum Media Density for Dead Load Analysis of Vegetative (Green) Roof Systems* (ASTM International, 2015) provides the processes to use to calculate density and air-filled porosity for granular ecoroof components, while ASTM E2398/E2398-15a *Standard Test Method for Water Capture and Media Retention of Geocomposite Drain Layers for Vegetative (Green) Roof Systems* (ASTM International, 2015) might also require consultation if drainage panels such as the one in Figure 5 are present. A more exhaustive explanation of the dead and live load calculation process can be found in Appendix C.

It was mentioned above that this standard does not consider the possibility of live load occurring outside of the drainage layer. Given that ecoroof growth media is usually porous soil or soil-like media that can hold water, it does not seem conservative that the standard ignores possible load exerted by this media in a saturated state.

Finally, it should be noted that E2397 does not address the loads associated with architectural or aesthetic elements, which are often present on more elaborate intensive ecoroofs.

### 2.2.2-Ecoroof Rain Loads

According to ASCE 7-10, rain loading accounts for the possibility of the obstruction of the primary roof drain, which leads to a build-up of water on the roof. Design rain loads are determined according to the following equation:

$$R = 5.2(d_s + d_h) \quad (2.1)$$

where  $R$  is the rain load on the undeflected roof (lb/ft<sup>2</sup>),  $d_s$  is the depth of water on the undeflected roof to the level of the secondary drainage system (in), and  $d_h$  is the additional depth of water on the undeflected roof above the secondary drain inlet when it is functioning at design flow. 5.2 is the product of the density of water (62.4 lb/ft<sup>3</sup>) and (1/12), which converts the water height from inches to feet, and allows the inputted water heights to be converted to psf. (ASCE, 2013).

Calculation of rain loads on an ecoroof could be complicated by the timing of the rain load occurrence. Provided that traditional roofs have an unrestricted drain and sufficient slope, drainage occurs nearly instantaneously. Due to the pore space in ecoroof soil, and the ability of other ecoroof components to hold water, ecoroofs can retain a portion of the runoff that they are subject to, while also causing drainage to occur over a more prolonged period of time. While ASTM E2397/E2397M-15 considers retained water as a live load, it does not take into consideration the changing shape of the load and possible structural effects associated with it as drainage occurs.

However, if blockage of the primary drain and development of a rain load occurs before the ecoroof has completed draining, second-order effects would be present because of the deflection of structural members due to the initial water that was unable to drain from the ecoroof.

An additional point of confusion could arise from where one considers the surface of the roof to be when determining  $d_s$ . If the excess water that can be held in the soil pore space is treated as a live load in accordance with ASTM E2397/E2397M-15, then the soil surface should also be identified as the roof surface, provided the load combination being considered includes both live load and rain loading. If a load combination considers rain load without live load, then it would be more conservative to identify the decking as the roof surface, to account for water that can be held by the soil and other ecoroof components.

### 2.2.3-Load Combinations Involving Rain Loads

ASCE 7-10 (ASCE, 2013) contains three load combinations that consider rain loading. The combinations are as follows:

$$2) \quad 1.2D + 1.6L + 0.5R$$

$$3) \quad 1.2D + 1.6R + L$$

$$4) \quad 1.2D + 1.0W + L + 0.5R$$

where the given numbering corresponds to the load combination number in the document.

If ecoroof live load is defined according to ASTM E2397/E2397M-15 (ASTM International, 2015) as the transient water live load, and the rain load datum is taken as the ecoroof surface, then the live load should be assumed to occur simultaneously with rain load, because were a rain load present, then the ecoroof would be completely saturated and

as such, a live load would be present as well. Consequently, it would be most appropriate to use a load factor of 1.0 or greater on both the live and rain loads when designing the structural members to support an ecoroof, due to the simultaneous occurrence of both loads. Therefore, load combination 3 is most likely the combination that best represents a realistic loading scenario for ecoroof structural members.

#### 2.2.4-Ponding

Aside from the aforementioned loads, when designing roofs, care must be taken to avoid ponding, "the retention of water due solely to the deflection of relatively flat roofs" (ASCE, 2013). Ponding can lead to the destabilization of a roof, when water retained in the deflection causes the deflection to increase, which then causes more water to run into the deflection, leading to further deflection, and so forth. Guidelines to avoiding ponding instability are provided in ASCE 7-10 and AISC 360-10.

ASCE 7-10 designates portions of a roof that have a slope less than ¼ in./ft., and roofs on which water is retained when the primary drainage system is blocked to be susceptible to ponding. The standard requires that a ponding analysis be conducted to ensure that susceptible roofs or portions of roofs have stiffness adequate to stop them from progressively deflecting as they collect water. (ASCE, 2013)

Meanwhile, AISC 360-10 details two processes that can be used to design for ponding in Appendix 2. In section 2.1, a simplified design process is laid out. This process centers around the calculation of two coefficients,  $C_p$  the coefficient of ponding flexibility for primary roof members, and  $C_s$ , the coefficient of ponding flexibility for secondary roof members. Coefficient calculation is done using the following formulas:

$$C_p = \frac{32L_S L_P^4}{10^7 I_P} \quad (2.2)$$

$$C_S = \frac{32SL_S^4}{10^7 I_S} \quad (2.3)$$

where  $L_S$  is the length of the secondary members (ft),  $L_P$  is the length of the primary members (ft),  $I_P$  is the moment of inertia of the primary members ( $\text{in}^4$ ),  $I_S$  is the moment of inertia of the secondary members ( $\text{in}^4$ ), and  $S$  is the spacing of the secondary members (ft).

Using the calculated ponding flexibility coefficients, if the two following equations are satisfied, then the roof system can be considered stable for ponding:

$$C_P + 0.9C_S \leq 0.25 \quad (2.4)$$

$$I_d \geq 25(S^4)10^{-6} \quad (2.5)$$

Where  $I_d$  is the moment of the inertia of the steel decking that is supported by secondary members.

Section 2.2 provides an "improved design for ponding", where two stress indexes are calculated, one primary members, and one for secondary members. These indexes are used, in combination with the flexibility coefficients  $C_P$  and  $C_S$  from the simplified design process to read from figures A-2.1 and A-2.2, shown below in Figure 6 and Figure 7, shown below:

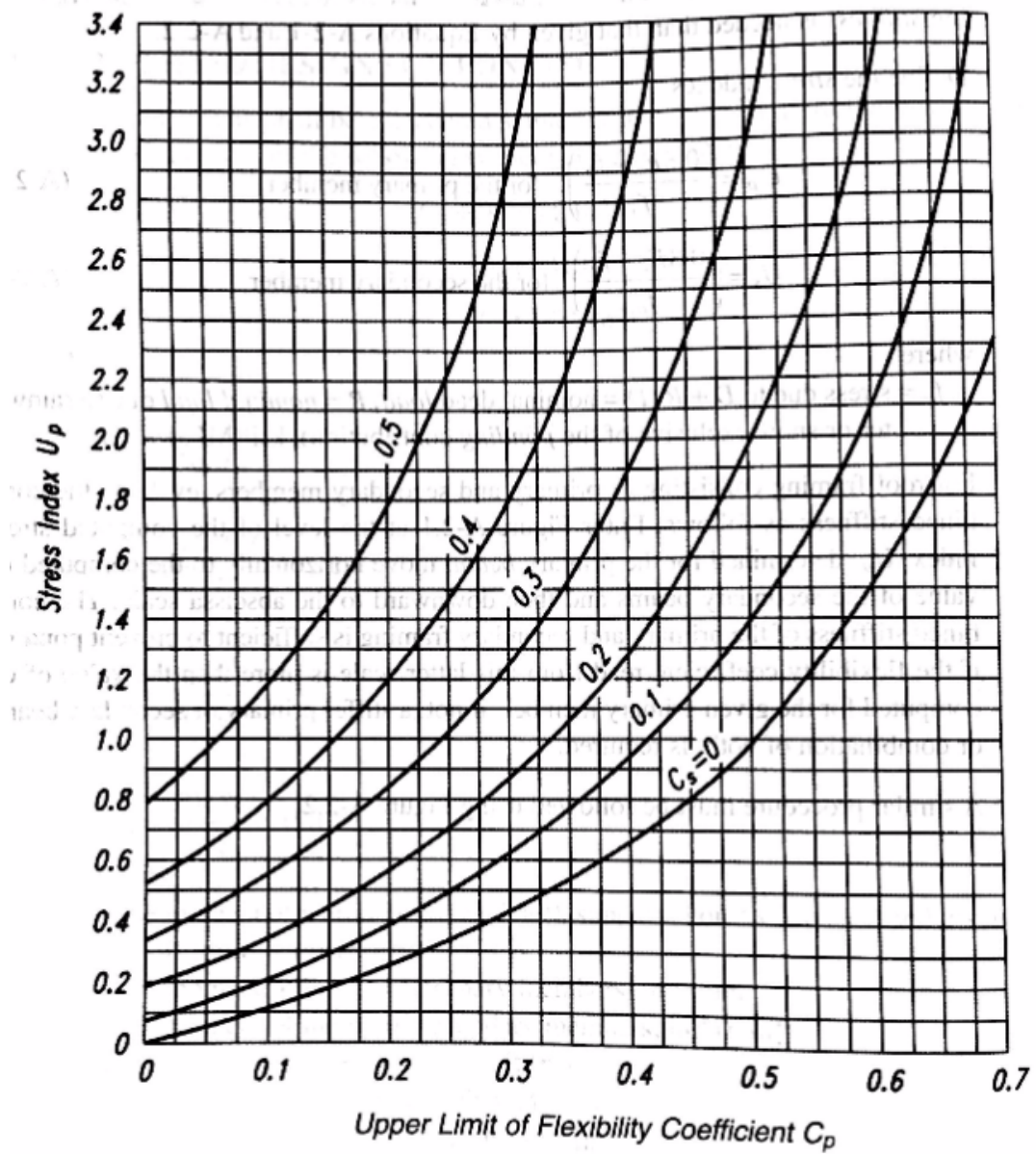


Fig. A-2.1. Limiting flexibility coefficient for the primary systems.

Figure 6: AISC Figure A-2.1 (AISC 360-10, Pg. 16.1-190)

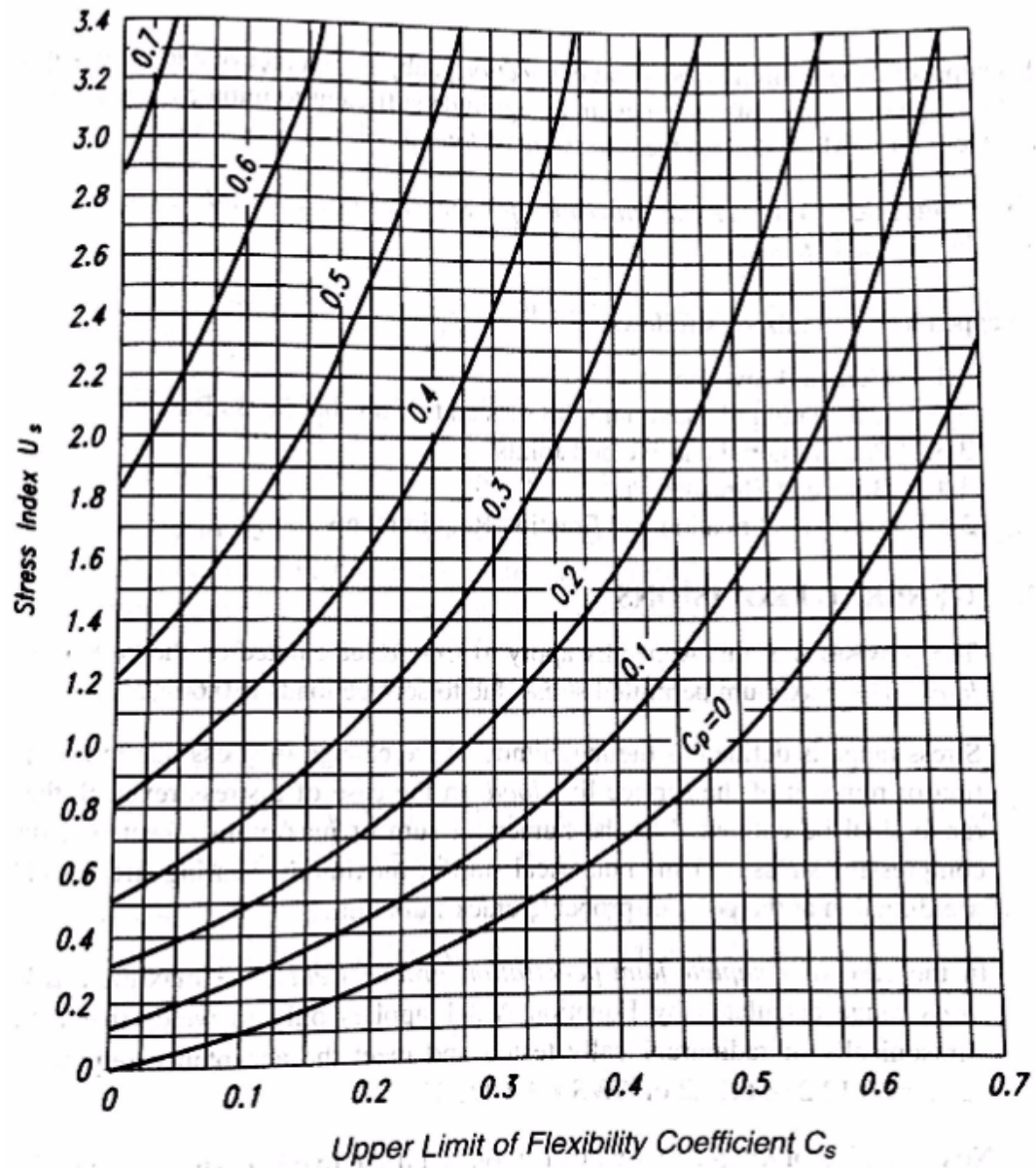


Fig. A-2.2. Limiting flexibility coefficient for the secondary systems.

Figure 7: AISC Figure A-2.2 (AISC 360-10, Pg. 16.1-191)

The figures are entered along the left axis using a calculated stress index, and then traveling across the figure until the flexibility coefficient is reached. At that point, travel



down to the bottom axis to determine the maximum permitted value of either  $C_S$  or  $C_P$ . If both figures are satisfied, then the combined stiffness of the primary and secondary members is adequate to prevent ponding; if the figures are not satisfied, then the design must be done with stiffer members.

## CHAPTER 3-EXPERIMENTAL DESIGN AND METHODOLOGY

### 3.1 – Ecoroof Structural System Construction

#### 3.1.1-Ecoroof Structural System

Elements of the shake table bounded the ecoroof on all four sides. On the east and west sides, 30' long W12x106s were laid so that they rested on both flanges. 12' W21x111s were used as cross beams on the north and south ends of the ecoroof. The structural system supporting the ecoroof consisted of three beams, and was designed with the intention that the center beam act as a typical member in a roofing continuum. As such, the center beam, a W12x26, was approximately twice as stiff as the two outer beams, both W12x16s, to ensure that one-way bending occurred, and that deflection between the three members was relatively uniform. A double angle shear connection was used to connect both ends of each member to a W21x111 cross beam, shown in Figure 8 below. This connection was comprised of two 9" deep L3-1/2 x 3-1/2 x 1/2 angles made from A36 steel. Three 13/16" diameter holes were present on both angle arms, and 3/4" diameter A325 grade heavy hex head structural bolts, with Grade C nuts were used in the connections. It should be noted that the angles selected for use in the connections were relatively deep in comparison to the beam depth (9" vs 12.2" respectively), possibly affecting the fixity of the connection, as discussed further during data analysis.



Figure 8: Ecoroof structural member double angel shear connection.

The north cross beam was elevated 7-1/2", allowing for the creation of the required 1/4" elevation per foot of member length.

Once the W12x26 and two W12x16s had been successfully hung, 20 gage steel decking was puddle welded into place along the top flange of the three beams in a 3/4 pattern, with one weld every 12 inches. 20 gage steel decking was selected because it was a commonly used gage for roofing systems.

### 3.1.2-Lateral Bracing

In order prevent the beams making up the roof system from deflecting laterally, two rollers were installed on the outer edge of each W12x16. Each roller was Winkel bearing that butted up against a 6"x 8" steel plate, that was welded to the top of a flange of a W12x106,

which itself comprised part of the shake table apparatus. Each Winkel bearing came attached to a prefabricated plate, with one threaded hole in each corner. A threaded rod was placed through each hole on the Winkel bearing plate, and ran through a corresponding hole in the web of the closest W12x16 beam. Three nuts were used on each threaded rod: one on each side of the W12x16 beam web, and one on the outside of the Winkel bearing plate. Figure 9 shows the set-up of one of the Winkel bearings.



Figure 9: Characteristic Winkel bearing configuration.

Each Winkel bearing was offset 18" from the centerline of the roof structure.

To ensure that the middle W12x26 beam was braced, two 3"x3"x1/4" angles were welded to it at the midspan; one to the west side of the upper flange, and one to the east side of the upper flange. Each of these angles was then welded to the upper flange of the corresponding W12x16 to create bridging, shown in Figure 10 below.



Figure 10: Western bridging on the W12x26 beam.

### 3.1.3-Parapet Walls

In order to create walls that would function as both containment for the ecoroof and as parapet walls, steel plates that alternated in widths of 2 inches and 4 inches were welded to the flanges of the shake table elements that bounded the ecoroof. Holes were drilled



through these plates, and plywood of 5/8" thickness was bolted to the plates to create the parapet walls. The parapet walls can be observed in greater detail in Figure 11 below.



Figure 11: Wooden parapet walls and supporting plates at southwest roof corner.

### 3.2 - Ecoroof Component Selection

Sheets of Georgia Pacific Densdeck, a gypsum roof board, were laid on top of the 20 gage steel decking to act as a roof cover board, and a thermoplastic polyolefin (TPO) membrane was then adhered to the top of the Densdeck. From the Densdeck, the membrane traveled up, and adhered to the top of the parapet walls, creating a waterproof container for the ecoroof to reside in. A TPO membrane was selected as the waterproofing layer because during phase II of this research, conducted by Kim Kilroy, the interface between the TPO

membrane and the root barrier possessed the smallest interface friction angle of any of the tested interfaces of ecoroof components. Selection of a TPO membrane ensures that when lateral shaking tests occur, the ecoroof system tested will present conditions that might be seen in a typical ecoroof setup that will react most sensitively to lateral shaking.

Directly on top of the TPO membrane was a drainage layer. The drainage layer consisted of a webbed mat of geosynthetic fibers, approximately 3/8" thick, and can be seen in the Figure 12 below.



Figure 12: Geosynthetic fiber drainage layer portion.



Figure 13 shows the polyester filter fabric that was used to separate the growing substrate and drainage layers.

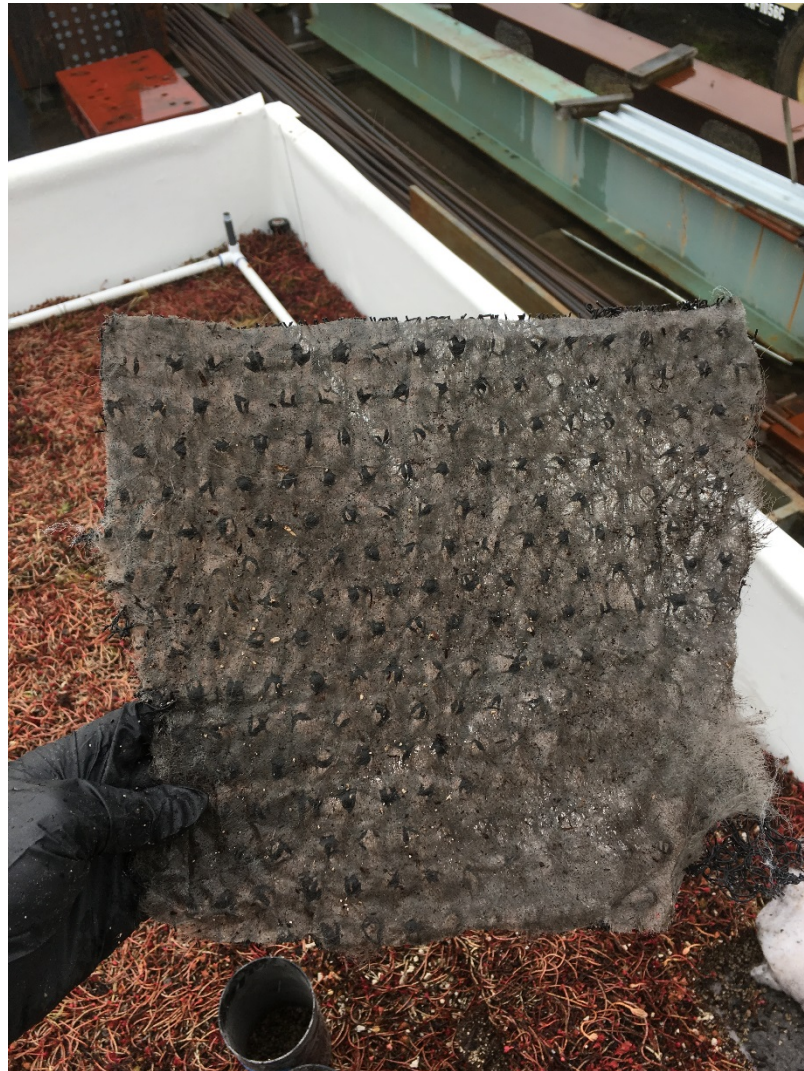


Figure 13: Polyester filter fabric, attached to drainage layer portion. The retention layer was directly above the filter fabric, and served to retain moisture for the plants, while also providing a location for them to take root. (Columbia Green Technologies, 2012). Figure 14 below shows the retention layer.





Figure 14: Retention layer portion.

Growing substrate was placed on top of the retention layer. It was a light, pumice-like material, with a calculated density of  $31.82 \text{ lbs/ft}^3$ . Additionally, the layer of growing media was 4 inches thick, a typical depth for extensive ecoroofs. The growing substrate is showing below in Figure 15.

Plants from the genus *sedum* make up the roof's uppermost layer. Figure 15 below, displays the plants used on the roof during testing.



Figure 15: Ecoroof plants and growing substrate.

It should be noted that although all irrigation was done with an overhead system that will be discussed below, a non-functioning irrigation system was included as part of the ecoroof installation, in order to make sure that the roof adhered as closely to industry standards as possible, a portion of which can be seen in the Figure 16 below.





Figure 16: Dummy irrigation system piping.

### 3.3 - Sprinkler System Design and Construction

In order to investigate the structural effects of ecoroof drainage on the structural system of the roof, a sprinkler system was designed to simulate rainfall events. According to Chapter 8 in ASCE 7-10 (ASCE, 2013), drainage design standards are assigned to local codes.

According to the 2014 Oregon Structural Specialty Code (International Code Council, 2014), design rainfall for rain loads “shall be based on the 100-year hourly rainfall rate indicated in Figure 1611.1, or on other rainfall rates determined from approved local weather data.” Figure 1611.1 is shown below in Figure 17. Additionally, according to the 2017 Oregon Plumbing Specialty Code, primary roof drains are sized based on the same 100 year, 1 hour duration event (International Code Council, 2017).

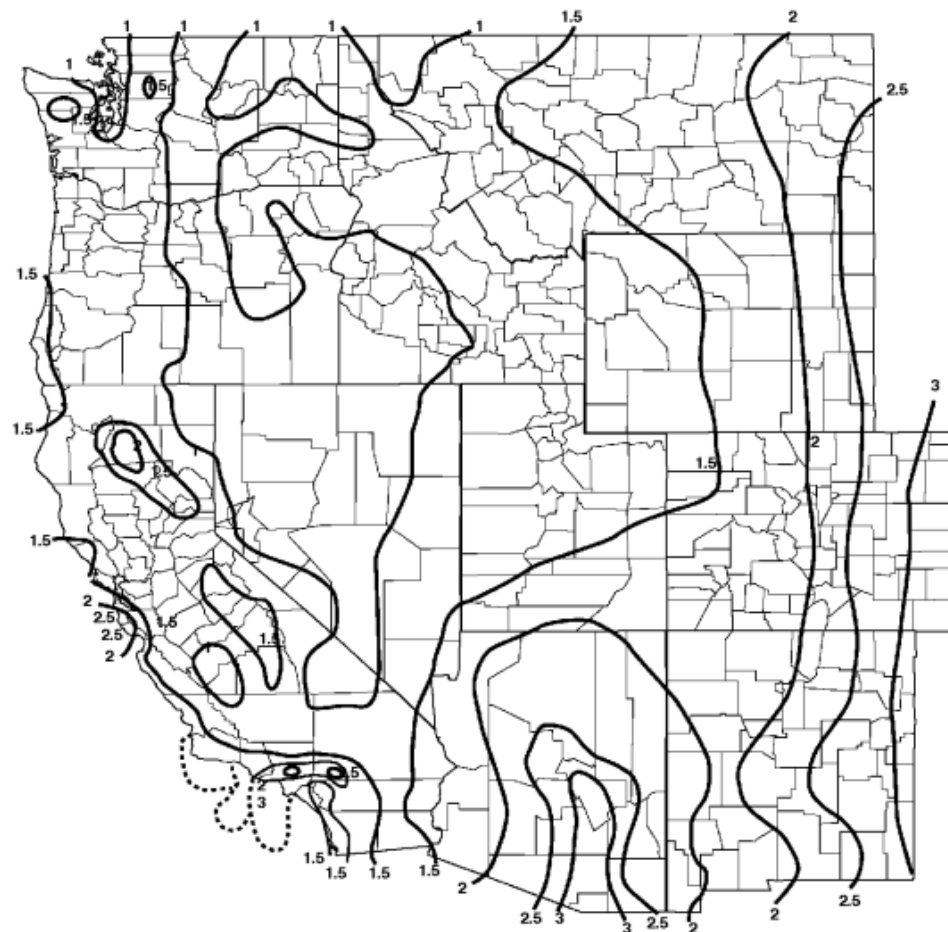


Figure 17: Figure 1611.1 from the Oregon Structural Specialty Code-Map of 1-hr rainfall with 100-yr return period. (Oregon Structural Specialty Code, pg 373)

Using Figure 17, it was determined that sprinkler system would be designed to simulate a storm with an intensity of 1 inch of rainfall per hour, because that is the designated intensity to be used when determining rainfall loading for the majority of the state of Oregon.

Toro Precision Series spray nozzles were initially selected as sprinkler heads for the system due to their advertised ability to delivery 1" of water per hour to a desired area. Using specifications provided on Toro's website, the amount of water that could be delivered by different sprinkler head configurations was calculated. Eventually, the configuration shown below in Figure 18 was decided upon, with each nozzle operating at a pressure of approximately 40 psi.

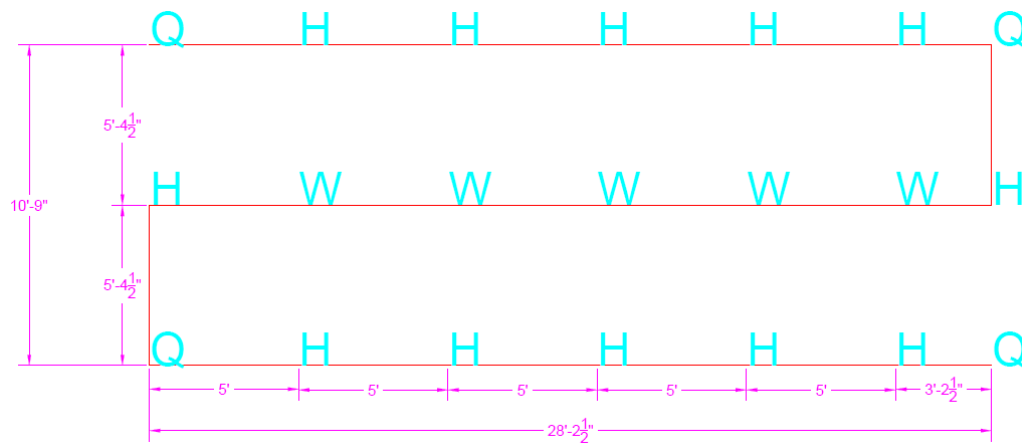


Figure 18: Rainfall simulation sprinkler system nozzle configuration.

The above configuration uses 5' radius sprinkler heads. With the exception of the rightmost sprinklers, the heads are spaced with a 5' separation, so that the throw of each sprinkler overlaps with others. Each letter indicates the location and type of sprinkler. Q's spray in a quarter-circle, H's in a half-circle, and W's a complete circle.



In order for this sprinkler configuration to output 1"/hr, the sprinkler heads were required to operate at 40 psi. To determine if the nearest tap could provide the required amount of water, a T was screwed to the end of a hose that was attached to the tap. Each end of the T contained valves that could control the amount of water released. A pressure gage was attached to one side of the T, with that side's valve entirely open. The valve on the other side of the T was left closed. A picture of this setup can be viewed in Figure 19 below.



Figure 19: Pressure measurement set-up.

The water was then turned on, and the valve on the open end of the T was gradually opened, until the pressure gage read 40 psi. At this point in time, a five-gallon bucket was filled with water while time was kept, to determine the flow rate provided by the tap at 40

psi. The flow rate was calculated to be 3.20 GPM, which nearly aligned with the calculated value of 3.22 GPM that the sprinklers required to provide 1"/hr of water to the roof.

After determining that the tap met the water volume requirements, two sprinkler system pipe configuration were considered. In the first configuration, the hose connected to a manifold, which fed three branch pipes that housed the sprinklers. The second configuration consisted of a single pipe that housed all sprinklers.

After conducting energy analyses using Bernoulli's equation, and determining the pressure loss in an extended length of PVC pipe to be negligible, the single pipe configuration was selected, and can be seen in Figure 20 below.



Figure 20: Sprinkler System Pipe Configuration.

### 3.4 – Instrumentation

#### 3.4.1-Strain Gages

Member forces in the three beams comprising the roof's structural system were measured using strain gages. The middle beam was most heavily instrumented, because it was the member of greatest concern, as it represented a standard roofing member. Figure 21 below contains the layout of the strain gages on the three beams.

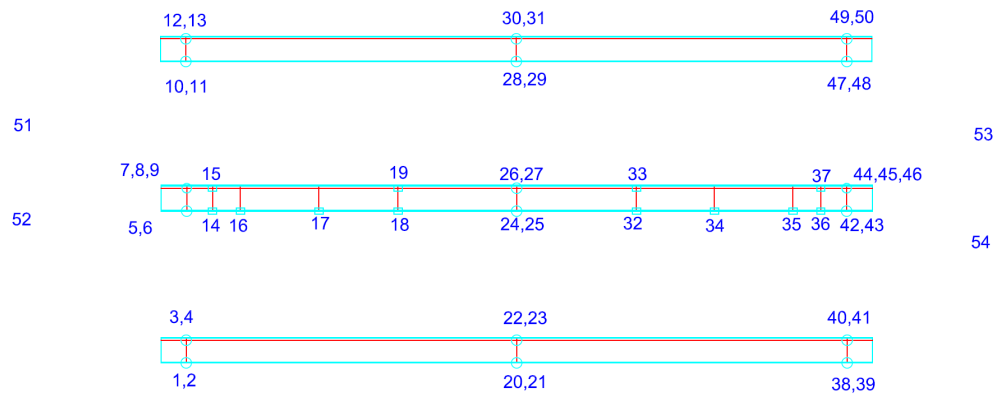


Figure 21: Strain Gage Layout

Strain gages 51-54 were placed on plates that support the parapet walls on the upslope and downslope ends of the roof. These gages were not utilized during the research conducted for this report, however they can be used to measure the forces that the parapet walls will be subject to when the ecoroof soil mobilizes during future lateral shaking tests.

On the two W12x16 outer beams, gages were present at the centerpoint and at a distance  $d$  (12 inches) from each end. Gages were offset from the ends to ensure that the stress field was stable and not influenced by the holes used in the connection, and so that they would be close to points where maximum shear tended to occur. There were two pairs of gages at each location. One pair was located on the bottom flange, and the second pair on the web, one inch below the bottom of the top flange. Each pair of gages was comprised of one longitudinal gage oriented along the length of the beam to measure mechanical strain, and a Poisson gage oriented perpendicular the longitudinal gage that was used to measure Poisson effects and strain that occurs due to temperature. Readings from the Poisson gage were used to separate temperature effects from the longitudinal gage's readings, so that mechanical effects due to roof loading could be isolated and analyzed.



The middle W12x26, being the main beam of interest, was more heavily instrumented than the two W12x16s. Gages were attached in a pattern that was symmetrical about the centerline of the beam, and placed at the following locations:  $d$ , and  $2d$  from the end, and at  $1/9$ ,  $2/9$ ,  $1/3$  and  $1/2$  points. At each strain gage location, gages were typically present on the bottom of the bottom flange, and on the web, one inch below the bottom of the top flange, like on the two W12x16 beams. Exceptions to this rule were made at six locations: the  $1/9$  and  $2/9$  points, along with their symmetrical counterparts, each contained a solitary longitudinal gage on the bottom of the bottom flange. Additionally, at both locations that were  $d$  from the end of the beam, three strain gages comprising a rosette were present on the beam web. The third gage in each rosette (in addition to the standard longitudinal and Poisson gages) was a gage that was placed at a  $45^\circ$  angle, which was used during calculations to determine the shear forces present. In addition to the rosette on the web, longitudinal and Poisson gage pairs were present on the bottom flange at the locations  $d$  from the beam ends. At the centerline, longitudinal and Poisson gages were present on both the bottom flange and beam web.

#### 3.4.2-Strain Gage Data Analysis Process

Following collection of data, the values returned by an instrument were adjusted by averaging the first 10 data points collected, and subtracting that average from all the data collected by the instrument for the duration of the test. This was done for every instrument used during testing, although data from the moisture sensors was used in both a raw and zeroed form.

Once initial data adjustment was complete, the following formula was used to isolate the mechanical strain effects from the temperature effects:

$$\epsilon_{mech} = \frac{\epsilon_{longitudinal} - \epsilon_v}{(1 - \nu)} \quad (3.1)$$

where  $\epsilon_{mech}$  is the strain due to mechanical effects,  $\epsilon_{longitudinal}$  is the strain read by the longitudinal gage,  $\epsilon_v$  is the strain read by the corresponding Poisson gage, and  $\nu$  is Poisson's ratio for steel, or 0.3. Appendix E contains the derivation of this formula.

At locations on the center W12x26 beam where Poisson gages were not present, Poisson gage values were produced using a linear interpolation between Poisson gages located "d" from the beam ends and those located at the beam midpoint. Linear interpolation was also used when web strain was needed at points where gages were not present. Once strain gage data had been corrected for temperature, the strains were then resolved into moment.

As analysis was conducted, removal of temperature effects proved difficult, unless the gages were near well-restrained positions, as was the case at the midpoint, seen in Figure 22.

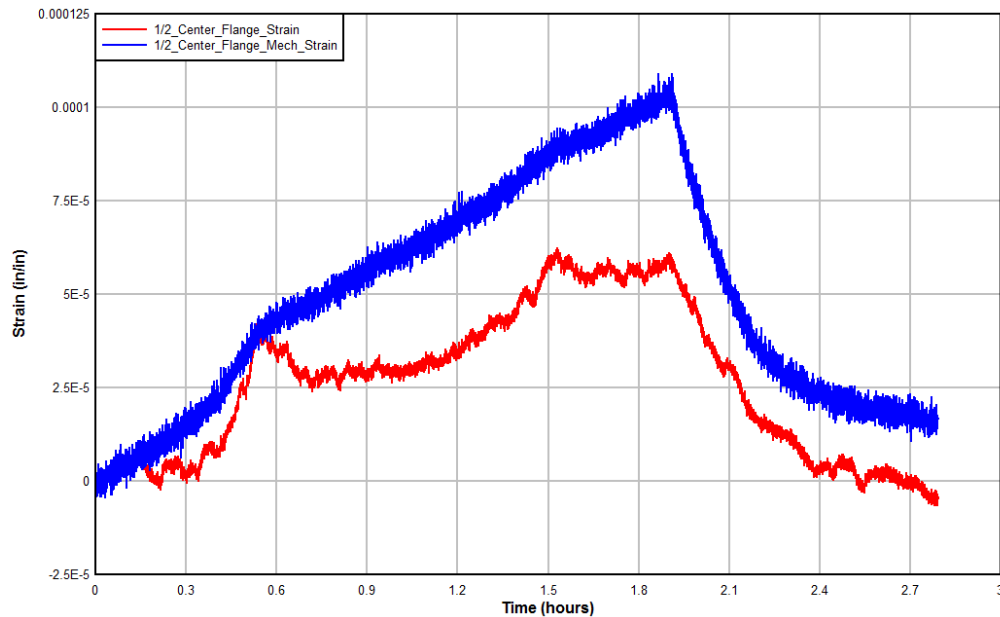


Figure 22: Midpoint Flange Strain (Raw and Temperature-Adjusted) vs Time

Indeed, it was found that attempting to remove temperature effects from some gages, such as gages 16 and 17, caused a deterioration in the quality of the data, as seen in Figure 23.

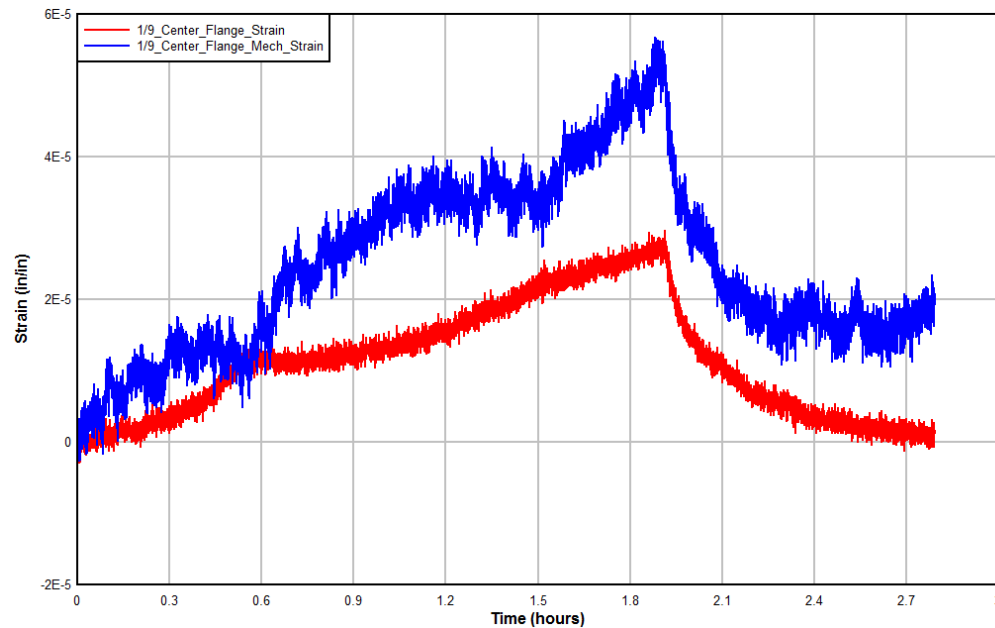


Figure 23: 1/9 Point Flange Strain (Raw and Temperature-Adjusted) vs Time

As data analysis progressed, it became apparent that the strain gages on the upslope half of the beam were not returning reliable data. That, combined with the lack of consistency in the temperature adjustment, led to a reliance on the midpoint strain gages, as they consistently returned reliable data, except in the case of the test with the smallest loading.

#### 3.4.3-Notes on the East and West Beams

For the tests conducted during this thesis, the only strain gages that from the East and West beams that were selected for use were those located and the beam midpoints.

#### 3.4.4-Calculation of Moment and Shear Using Strain Gage Pairs

Moment was calculated using the following equation:

$$M = (\epsilon_{mech_f} - \epsilon_{mech_w}) \left[ \frac{E \cdot I}{d'} \right] \quad (3.2)$$

where  $M$  is the moment at the location of interest (k-in),  $\epsilon_{mech_f}$  is the mechanical strain from the flange strain gage,  $\epsilon_{mech_w}$  is the mechanical strain from the web strain gage (both strain gages read in microstrain, so  $10^{-6}$  is appended to gage readings),  $E$  is Young's modulus for steel (ksi),  $I$  is the major axis moment of inertia of the beam of interest ( $\text{in}^4$ ), and  $d'$  is the distance separating the two gages (in).

#### 3.4.5-String Pots

Five string pots are being used to track beam deflections, and have been placed in the arrangement shown in Figure 24 below.

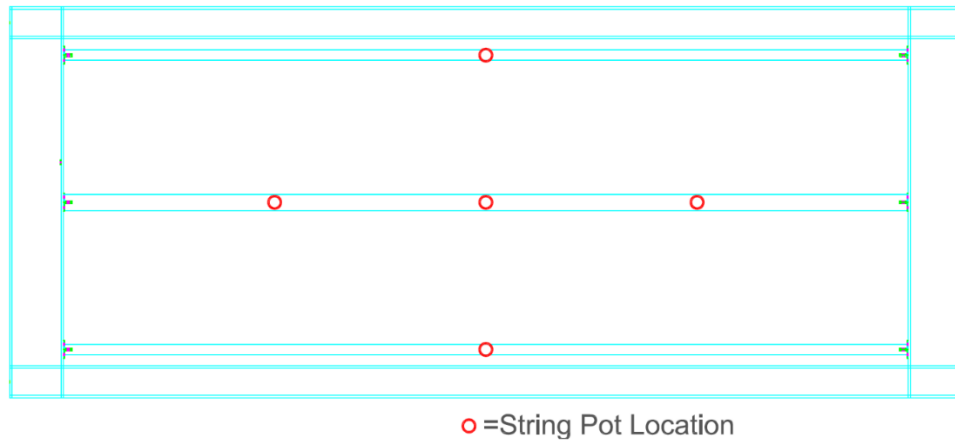


Figure 24: String Pot Layout.

Three string pots were on the center W12x26 beam, located at the  $\frac{1}{4}$ ,  $\frac{1}{2}$ , and  $\frac{3}{4}$  points, while both W12x16 beams had one string pot, located at the centerline. As with strain gages, the center beam was more heavily instrumented because it was the beam of primary interest.

As seen in the figure below, a pin connection was used to attach each string pot to an aluminum channel, which was itself anchored to a concrete pad, as seen in Figure 25

below.



Figure 25: String Pot Pin Connection

Due to the pin connection, each string pot is able to rotate, and will be able to follow the horizontal motion of the table when lateral shaking tests occur.

In addition to the aforementioned locations on the roof structure beams, displacements were also tracked at the north and south support locations. These displacements were then removed from the measured  $\frac{1}{4}$ ,  $\frac{1}{2}$ , and  $\frac{3}{4}$  displacements on the center beam, to account for the beam's rigid body motion.

#### 3.4.6-Flow Meter

A Proteus Industries Model 0812BN19 flow meter connected the hose and the sprinkler system, allowing the amount of water that was introduced to the roof through the sprinklers to be tracked.

#### 3.4.7-Soil Moisture Sensors

Three EC-5 small soil moisture sensors were used to track soil water content and flow through the soil. The sensors were installed in the soil above the central beam, with one sensor just north of the drainage area at the south end, one sensor at the midpoint, and one sensor at the  $\frac{3}{4}$  point. Each sensor tracked volumetric water content (VWC), which is defined as the ratio of volume of water present to volume of soil. Each sensor included a thermocouple that was used to account for variation in temperature. Prior to testing, each sensor was calibrated using soil samples from the roof. In addition to the sensor calibration, dry and surface saturated soil densities were determined.

#### 3.4.8-Water Level Sensors

Water level throughout the soil was tracked using two ToughSonic 14 UltraSonic sonic level sensors. One sensor was located on the east edge of the ecoroof at the centerline, and a second sensor was located in the drainage area at the downslope end.

#### 3.4.9-Outflow Measurement

Outflow exited the ecoroof through a scupper located at the southwest corner, which evacuated the water into drainpipe, allowing the water to travel from ecoroof to ground elevation. The drainpipe emptied into a six inch diameter pipe, which was outfitted with a weir. Height of water flowing through the weir was measured with a third ToughSonic 14 UltraSonic level sensor. Data from the ultrasonic level sensor was compared to the outflows designated on the weir to determine the outflow from the roof.

#### 3.4.10-End Rotation Sensor

A sensor was used to measure the downslope end rotation of the primary beam. End rotations were primarily used to assess the fixity of the connection.

### 3.5-Ecoroof Dead Load Determination

Ecoroof dead load was determined by measuring a 1 square foot section of roof as a whole.

This section consisted of a retention layer, polyester filter fabric, a geosynthetic drainage layer and root barrier, ecoroof soil, and ecoroof plants. The portion of the ecoroof was placed into a fitted plastic contained, with a known weight. The ecoroof was then weighed in two conditions: as it was immediately after removal from the roof, and at surface saturation.

### 3.6 – Loading Calibration

In order to ensure that strain gages and string pots were functioning accurately, and to ascertain how load is distributed among the three members comprising the structural portion of the ecoroof, a single point load of 3338 lbs was applied to the central W12x26 member. This point load was applied 11.875 feet (142.5 inches) from the upslope end of the beam, or, at a distance of 192 inches from the downslope end.

A wooden post was jacked up onto the bottom flange of the center beam in order to apply the point load. A load cell resting beneath the jack recorded the load exerted on the beam. The maximum value recorded by the load cell during the test was then used to create a theoretical moment diagram for the center beam, the theoretical midpoint load was determined.

Following the theoretical calculations, moment at the midpoint of the west, center, and east beams was determined using the strain gage measurements that corresponded to the point in time when the maximum load occurred. The summation of the midpoint moments of all three beams was compared to the theoretical midpoint moment caused by the load to ensure accuracy. Once the accuracy of the measurements had been confirmed, a moment distribution was created that denoted the midpoint moment exerted on each beam, and the percentage of the total moment that each beam undertook. This distribution was later used

when assigning tributary widths to each member. A 4.69% error existed between the theoretical moment (237.7 k-in) and the experimental moment (248.8 k-in).

### 3.7-Ponding Tests

#### 3.7.1-Ponding: Unevenly Distributed Water

Raw data of all strain gages was examined in order to determine accuracy. Of the gages that collected data on the primary center beam: the following were used during a check for data accuracy:

Gage Number	Gage Description
6	d_Flange_Poisson
7	d_Web_Strain
9	d_Web_Poisson
14	2d_Flange_Strain
15	2d_Web_Strain
16	1/9_Flange_Strain
17	2/9_Flange_Strain
24	1/2_Flange_Strain
25	1/2_Flange_Poisson
26	1/2_Web_Strain
27	1/2_Web_Poisson
42	d_Far_End_Flange_Strain
43	d_Far End_Flange_Poisson

The first 450 data points were disregarded in this analysis, as they did not return usable data, due to data collection beginning in advance of the test commencement.

To check the accuracy of the strain gage data that was collected, curvature was calculated using both flange and web strain gages, according to **Error! Reference source not found..** Curvature was then double-integrated to determine displacement, and percent error was calculated. Using this method, percent error between the center beam midpoint strain gage



data and the data collected by the center midpoint string pot was 3.93%. Ultimately, only midpoint flange and web strains were used as the data analysis process proceeded.

### 3.7.2-Ponding: Evenly Distributed Water Usable Strain Gages

Of the gages that collected data on the primary center beam: the following were used during a check for data accuracy:

<b>Gage Number</b>	<b>Gage Description</b>
6	d_Web_Poisson
7	d_Web_Strain
8	d_Web_Shear
14	2d_Flange_Strain
15	2d_Web_Strain
16	1/9_Flange_Strain
17	2/9_Flange_Strain
24	½_Flange_Strain
25	½_Flange_Poisson
26	1/2_Web_Strain
27_	½_Web_Poisson
44	d_Far End_Web_Shear

To check the accuracy of the strain gage data that was collected, curvature was calculated using both flange and web strain gages, according to **Error! Reference source not found.** Curvature was then double-integrated to determine displacement, and percent error was calculated. Using this method, percent error between the center beam midpoint strain gage data and the data collected by the center midpoint string pot was 0.41%. As mentioned previously, following the completion of the curvature double-integration, only the midpoint strain gages were used during data analysis.

### 3.8-Rain Events

#### 3.8.1-Natural Rain Event

Strain gage data did from the natural event could not be feasibly used during data analysis, because the gages were not able to return accurate responses when faced with the small magnitude of the loading.

Due to the uncertain timing of the natural event, the first 6000 points of data that were collected were not used during the data analysis process.

#### 3.8.2-Simulated 1-hr Design Rain Event

For this test, the center beam midpoint strain gages were the only gages that returned usable data. Double integrating curvature, using only the midpoint curvature returned a displacement with 5.69% difference compared to the measured center beam midpoint displacement. The larger percent difference in this test when compared to the ponding tests can be attributed to the lack of strain gage data that contributing to the curvature diagram.

### 3.9-Moment Amplification Factor (Beta)

#### 3.9.1-Moment Amplification Factor Introduction

As part of this project, a moment amplification factor, hereafter called “Beta” was developed to allow the first order moment for a roof design in which ponding was a concern to be amplified, such the following two equations would be approximately equal.

$$M_{total} = M_1 + M_2 \quad (3.3)$$

$$M_{total} = \beta M_1 \quad (3.4)$$

where  $M_1$  is the moment due to first-order effects,  $M_2$  is the moment due to second-order effects, and  $M_{total}$  is the total moment experienced by the roof beam in question, due to both first and second-order effects. More directly, the equation for Beta is as follows:

$$\beta = \frac{M_1 + M_2}{M_1} \quad (3.5)$$

where  $M_1$  and  $M_2$  are as defined above.

### 3.9.2-Description of Model Used to Investigate Beta

Beta was investigated using a model built in Microsoft Excel, and was calculated using a variety of values of EI, beam length, roof slopes, initial dead load, with varying secondary drain heights, being used to constrain the amount of water that can accrue in the case of rain loading. Loads were applied to the roof in the states detailed in Figure 26 and Figure 27, below. Figure 26 displays the uniform dead load, and the rain load that were used in first-order moment calculations, while the roof shape was undeflected. Figure 27 shows a theoretical deflected roof shape, and indicates the presence of additional area where water could reside that is created after initial deflection.

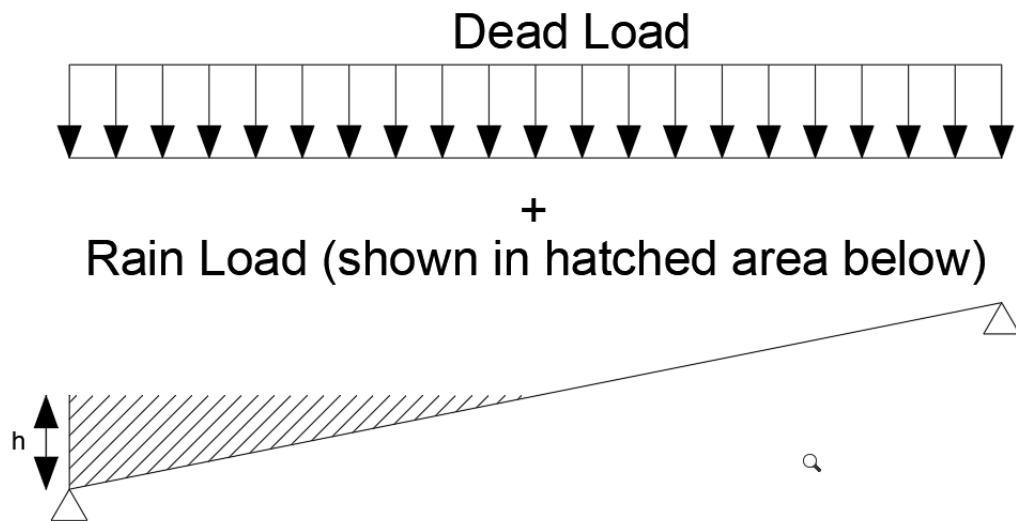


Figure 26: Undeflected Roof-Loads Used for 1st-Order Moment Calculations

## 2nd Order Rain Load (shown in hatched area below)

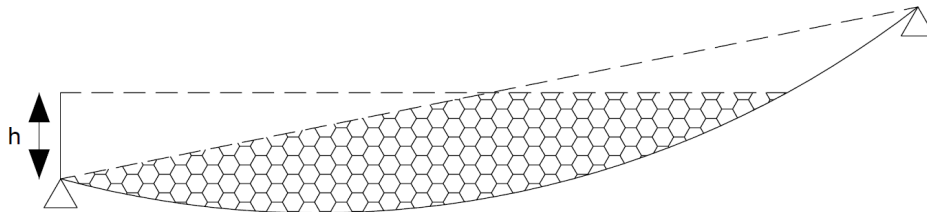


Figure 27: Deflected Roof-Loads Used for 2nd-Order Moment Calculations

Dead load was applied as a constant, continuous line load along the length of the undeflected beam. First-order rain load was applied as a triangular load that was constrained by the secondary drain height,  $h$ , and the slope of the roof,  $\alpha$ . Following the application of each load, shear and moment were calculated along the length of the beam. Curvature was arrived at by dividing the moments by  $EI$ , and numerical integration was then utilized to determine displacement due to the applied loads. The model allowed for the initial value of curvature to be altered in order to ensure that displacement at both beam ends was zero. Total first-order moment was determined by adding moment due to dead load and moment due to rain load together; Total first-order displacement was found using the same method.

Following the completion of the displacement calculations, second-order effects were calculated. This process began by determining the difference between the initial elevation of a point on the beam, and the new elevation after the application of the first-order loads. If the new elevation was found to be less than  $h$ , the elevation of the secondary drain, then the calculated difference was considered to be filled with water. The calculation of new elevations, and comparison of the elevations to secondary drain height continued along the

length of the beam. Following the completion of this process, a second-order load had been determined, and the maximum moment due to said load was found. It should be noted that second-order effects were only calculated once; after calculation of second-order effects, water was not assumed to flow into the new displacement and load the roof further, causing more displacement.

### 3.9.3-Derivation of Flat Roof Beta Equation

Due to total first-order moment being composed moment due to dead load, and moment due to rain load, Beta can be redefined as follows:

$$\beta = \frac{M_D + M_R + M_2}{M_D + M_R} \quad (3.6)$$

where  $M_D$  is the first-order moment due to dead load,  $M_R$  is the first-order moment due to rain load, and  $M_2$  is the second-order moment. Using this definition of Beta, an equation that predicts Beta for any flat roof was derived, using the following procedure:

#### **Maximum moment due to dead load**

$$M_D = \frac{w_D * L^2}{8} \quad (3.7)$$

Where  $w_D$  is the line load dead load, and  $L$  is beam length

#### **Maximum moment due to rain load**

$$M_R = \frac{w_R * L^2}{8} \quad (3.8)$$

Where  $w_R$  is line load rain load, and  $L$  is as defined above.

#### **Deflection due to dead and rain loads**

$$\Delta_{D+R} = \frac{(w_D + w_R) * x}{24EI} * (L^3 - 2Lx^2 + x^3) \quad (3.9)$$

Where  $\Delta_{D+R}$  beam deflection due to dead load and first-order rain load,  $E$  is modulus of elasticity of the beam, and  $I$  is moment of inertia of the beam.

Multiplying  $x$  through:

$$\Delta_{D+R} = \frac{(w_D + w_R)}{24EI} * (L^3 x - 2Lx^3 + x^4) \quad (3.10)$$

## 2<sup>nd</sup> Order Moment Equation

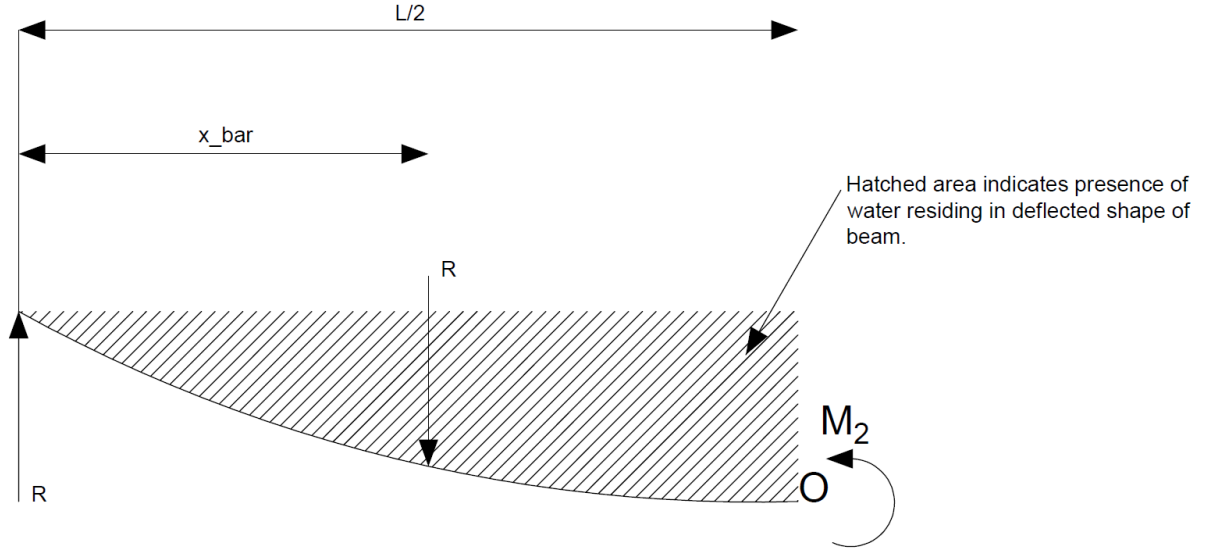


Figure 28: Flat Roof Second-Order Effects Free-Body Diagram

$$M_2 = R * \frac{L}{2} - R * \left( \frac{L}{2} - \bar{x} \right) \quad (3.11)$$

Where  $M_2$  is the moment due to second-order effects,  $R$  is the reaction due to second-order effects, and  $\bar{x}$  (written as  $x\_bar$  in Figure 28) is the centroid of the second-order load occupying the space from the left end of the beam to the midpoint.

### Reaction:

$$R = \int_0^{\frac{L}{2}} \Delta_{D+R} dx * \gamma_w * t_w \quad (3.12)$$

Where:  $\gamma_w$  is the specific weight of water and  $t_w$  is the tributary width associated with the beam.

Substituting  $\Delta_{D+R}$  into the integral:

$$R = \int_0^{\frac{L}{2}} \frac{(w_D + w_R)}{24EI} * (L^3 x - 2Lx^3 + x^4) dx * \gamma_w * t_w \quad (3.13)$$

Moving constants outside of the integral:

$$R = \frac{(w_D + w_R)}{24EI} \int_0^{\frac{L}{2}} (L^3 x - 2Lx^3 + x^4) dx * \gamma_w * t_w \quad (3.14)$$

Integration and substituting upper bound,  $\frac{L}{2}$ , in for x:

$$R = \frac{(w_D + w_R)}{24EI} * \left( \frac{L^3}{2} \left( \frac{L}{2} \right)^2 - \frac{L}{2} \left( \frac{L}{2} \right)^4 + \frac{1}{5} \left( \frac{L}{2} \right)^5 \right) * \gamma_w * t_w \quad (3.15)$$

Applying powers to  $\frac{L}{2}$  terms:

$$R = \frac{(w_D + w_R)}{24EI} * \left( \frac{L^3}{2} \left( \frac{L^2}{4} \right) - \frac{L}{2} \left( \frac{L^4}{16} \right) + \frac{1}{5} \left( \frac{L^5}{32} \right) \right) * \gamma_w * t_w \quad (3.16)$$

Simplification:

$$R = \frac{(w_D + w_R)}{24EI} * \left( \frac{L^5}{8} - \frac{L^5}{32} + \frac{L^5}{160} \right) * \gamma_w * t_w \quad (3.17)$$

$$R = \frac{(w_D + w_R)}{24EI} * \left( \frac{L^5}{10} \right) * \gamma_w * t_w \quad (3.18)$$

$$R = \frac{(w_D + w_R) L^5 \gamma_w t_w}{10 * 24EI} \quad (3.19)$$

**X-bar:**

$$\bar{x} = \frac{\int_0^{\frac{L}{2}} x * \Delta_{D+R} dx}{\int_0^{\frac{L}{2}} \Delta_{D+R} dx} \quad (3.20)$$

X-bar numerator:

$$\int_0^{\frac{L}{2}} x * \frac{(w_D + w_R)}{24EI} * (L^3 x - 2Lx^3 + x^4) dx \quad (3.21)$$

Moving constants to outside of integral:

$$\frac{(w_D + w_R)}{24EI} * \int_0^{\frac{L}{2}} L^3 x^2 - 2Lx^4 + x^5 dx \quad (3.22)$$

Integration and substituting upper bound,  $\frac{L}{2}$ , in for x:

$$\frac{(w_D + w_R)}{24EI} * \left( \frac{L^3}{3} \left( \frac{L}{2} \right)^3 - \frac{2L}{5} \left( \frac{L}{2} \right)^5 + \frac{1}{6} \left( \frac{L}{2} \right)^6 \right) \quad (3.23)$$

Applying powers to  $\frac{L}{2}$  terms:

$$\frac{(w_D + w_R)}{24EI} * \left( \frac{L^3}{3} \left( \frac{L^3}{8} \right) - \frac{2L}{5} \left( \frac{L^5}{32} \right) + \frac{1}{6} \left( \frac{L^6}{64} \right) \right) \quad (3.24)$$

X-bar numerator simplification:

$$\frac{(w_D+w_R)}{24EI} * \left( \frac{L^6}{24} - \frac{L^6}{80} + \frac{L^6}{384} \right) \quad (3.25)$$

$$\frac{(w_D+w_R)}{24EI} * \left( \frac{61L^6}{1920} \right) \quad (3.26)$$

$$\frac{61(w_D+w_R)L^6}{1920*24EI} \quad (3.27)$$

X-bar simplification:

$$\bar{x} = \frac{\frac{61(w_D+w_R)L^6}{1920*24EI}}{\frac{(w_D+w_R)L^5}{10*24EI}} \quad (3.28)$$

$$\bar{x} = \frac{61}{192}L \quad (3.29)$$

**2<sup>nd</sup>-Order Moment determination:**

$$M_2 = R * \frac{L}{2} - R * \left( \frac{L}{2} - \bar{x} \right) \quad (3.30)$$

Substituting Equations into  $M_2$  and simplifying:

$$M_2 = \left( \frac{(w_D+w_R)L^5\gamma_w t_w}{10*24EI} \right) * \frac{L}{2} - \frac{(w_D+w_R)L^5\gamma_w t_w}{10*24EI} * \left( \frac{L}{2} - \frac{61}{192}L \right) \quad (3.31)$$

$$M_2 = \left( \frac{(w_D+w_R)L^5\gamma_w t_w}{10*24EI} \right) * \frac{L}{2} - \frac{(w_D+w_R)L^5\gamma_w t_w}{10*24EI} * \left( \frac{35}{192}L \right) \quad (3.32)$$

$$M_2 = \left( \frac{(w_D+w_R)L^6\gamma_w t_w}{20*24EI} \right) - \frac{35(w_D+w_R)L^6\gamma_w t_w}{192*10*24EI} \quad (3.33)$$

$$M_2 = \frac{61(w_D+w_R)L^6\gamma_w t_w}{46080EI} \quad (3.34)$$

**Beta**

$$\beta = \frac{M_D+M_R+M_2}{M_D+M_R} \quad (3.6)$$

Substituting equations for  $M_D$ ,  $M_R$ , and  $M_2$  into equation for Beta:

$$\beta = \frac{\frac{w_D*L^2}{8} + \frac{w_R*L^2}{8} + \frac{61(w_D+w_R)L^6\gamma_w t_w}{46080EI}}{\frac{w_D*L^2}{8} + \frac{w_R*L^2}{8}} \quad (3.35)$$

Factoring out  $\frac{L^2}{8}$ :

$$\beta = \frac{\frac{L^2}{8} \left( w_D+w_R + \frac{61(w_D+w_R)L^4\gamma_w t_w}{5760EI} \right)}{\frac{L^2}{8} (w_D+w_R)} \quad (3.36)$$

Splitting Fractions:



$$\beta = \frac{w_D + w_R}{w_D + w_R} + \frac{61(w_D + w_R)L^4\gamma_w t_w}{5760EI(w_D + w_R)} \quad (3.37)$$

Simplifying:

$$\beta = 1 + \frac{61L^4\gamma_w t_w}{5760EI} \quad (3.38)$$

It should also be noted that this moment amplification factor only takes into account first iteration second order effects, and does not account for any potential moment amplification that might occur due to the additional displacement caused by the second-order effects themselves. So, it is an implicit assumption that any further second-order effects beyond those due to the displacements associated with the loads named in load combinations are negligible, which is a reasonable assumption if beta is relatively small and the roof is stable.

#### 3.9.4-Calculation of Experimental Beta

Experimental beta was calculated for the uniform input ponding test. The maximum midpoint moment from the center beam was taken as  $M_{total}$ . The first order moment,  $M_1$  was then calculated, based on the water elevation associated with the maximum moment, and beta was determined by dividing  $M_{total}$  by  $M_1$ . Experimental beta was then compared to the theoretical beta for the roof, as determined by the model used during the beta investigation, and will be discussed in Chapter 4.

## CHAPTER 4-DRAINAGE TESTING RESULTS

### 4.1-Program of Testing

For ease of reference, the program of testing is presented again below, in Table 1.

Test	Description
Load Calibration	A single point load of known magnitude was applied to the center roof girder. Returned instrumentation data was compared to theoretical expectations to ensure that instrumentation was functioning as expected and explore load distribution.
Ponding (Flooding Input)	The ecoroof drain was clogged to prevent drainage, and a large amount of water was collected on the roof from several output locations on the ecoroof surface. This data was used to assess the structural performance of the ecoroof in a more extreme event.
Ponding (Uniform Input)	A similar test to the above, however, water was added to the roof, using the sprinkler system built for the 1-hr rain event test, applying it uniformly over the area.
Natural Rain Event Observation	Data about the ecoroof's structural behavior was collected during the course of a natural rain event.
1-hr Rain Event (Structural & Drainage Design Event)	Sprinklers designed to deliver a set amount of precipitation, uniformly to the ecoroof area, were operated for 1-hr, and the ecoroof's structural behavior during and after this period was monitored for as long as data could be determined to be accurate without the use of temperature correction.

Discussion of figures will proceed in the order in which they are listed in the table, with the exception of the load calibration test, which is mentioned before discussion of the results from the model of the hydraulically loaded roof.

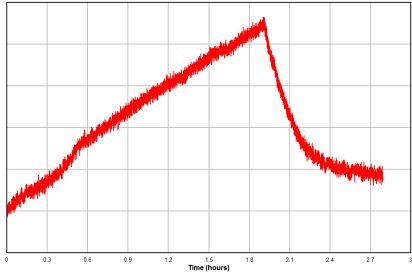
### 4.2 – General Discussion

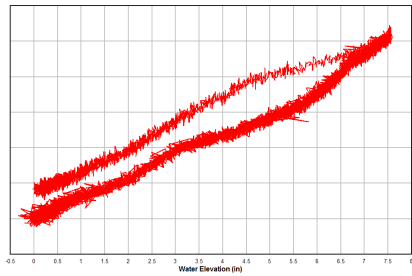
Ecoroof characteristics are plotted vs two quantities: time, and the height of the water against the downslope parapet wall, which corresponds to the imagined secondary drain height of the roof. For the rain events, both the natural event and the simulated 1-hr design event, characteristic quantities proved to be too small to rise above the noise and display

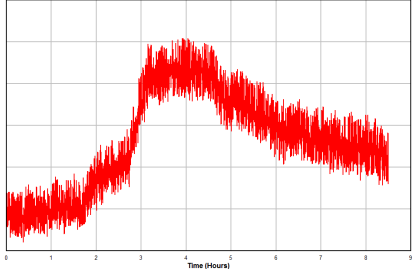
any meaningful relationships. Consequently, data from the rain events is only displayed vs time.

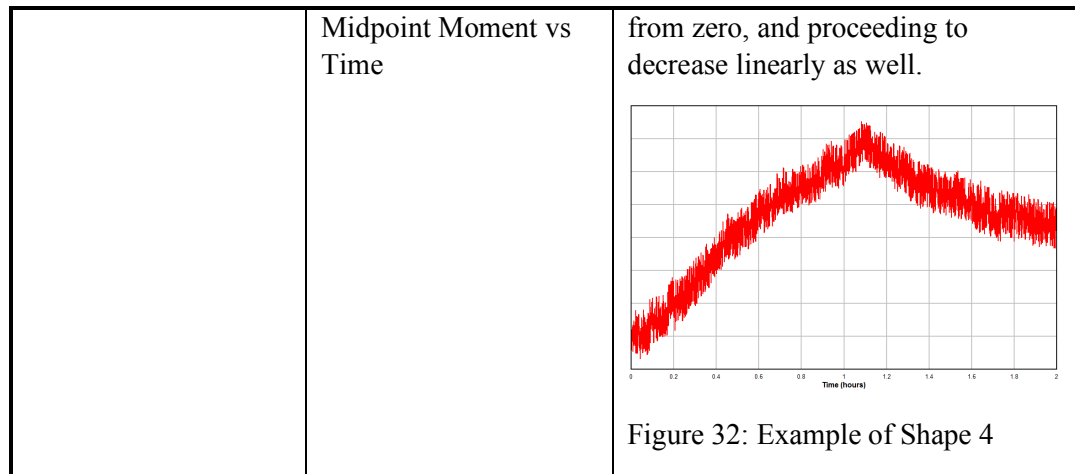
Plots of numerous characteristics had similar shapes. The test, associated characteristics, and a description of the common shape can be found below in Table 2. Discussion that follows the table will concentrate on more specific aspects of each plot.

*Table 2: Description of Common Plot Appearances*

Test	Characteristic	Description
Ponding: Randomized Loading	Center Beam Displacements vs Time	<p>Characteristic begins by increasing linearly from zero to point of maximum magnitude. Once past maximum, characteristic begins decreasing, with the rate decaying as time passes. An example of the shape is shown below in Figure 29.</p>  <p>Figure 29: Example Shape 1</p>
	Midspan Displacements vs Time	
	Support Displacements vs Time	
	Downslope Parapet Wall Water Elevation vs Time	
	Midpoint Flange Strain/Stress vs Time	
	Midpoint Moment vs Time	
	Tilt vs Time	
Ponding: Uniform Loading	Center Beam Displacements vs Time	
	Midspan Displacements vs Time	
	Support Displacements vs Time	
	Downslope Parapet Wall Water Elevation vs Time	

	Midpoint Flange Stress/Strain vs Time	
	Midpoint Moment vs Time	
	Tilt vs Time	
Ponding: Randomized Loading	Center Beam Displacements vs Downslope Parapet Wall Water Elevation	<p>As downslope parapet wall water elevation increases, the characteristic increases from zero, with rate of increase initially linear, but becoming nonlinear. Once the maximum water elevation is reached, the characteristic begins decreasing, however it does not follow the path established while water elevation was increasing. Instead, it decreases at a nearly linear rate of equal or smaller magnitude than the nonlinear rates that occurred at the larger water elevations. When water elevation reaches zero, there is a residual amount of the characteristic still present. An example of the shape is shown below in Figure 30.</p>
	Midspan Displacements vs Downslope Parapet Wall Water Elevation	
	Support Displacements vs Downslope Parapet Wall Water Elevation	
	Midpoint Flange Strain/Stress vs Downslope Parapet Wall Water Elevation	
	Midpoint Moment vs Downslope Parapet Wall Water Elevation	
Ponding: Uniform Loading	Center Beam Displacements vs Downslope Parapet Wall Water Elevation	 <p>Figure 30: Example of Shape 2</p>
	Midspan Displacements vs Downslope Parapet Wall Water Elevation	
	Support Displacements vs Downslope Parapet Wall Water Elevation	
	Midpoint Flange Strain/Stress vs	

	Downslope Parapet Wall Water Elevation	
	Midpoint Moment vs Downslope Parapet Wall Water Elevation	
Rain: Natural Event	Center Beam Displacements vs Time	<p>As time increases, each characteristic increases nonlinearly from zero to the maximum value, with rate of increase becoming larger as time passes. As the maximum value the characteristic plateaus before beginning to decrease nonlinearly, with the rate of decrease becoming smaller as time passes. An example of the shape is shown below in Figure 31. Midpoint moment and midpoint flange, while similar to the shape shown below, do not plateau, instead beginning to decrease immediately.</p>  <p>Figure 31: Example of Shape 3</p>
	Midspan Displacements vs Time	
	Support Displacements vs Time	
	Midpoint Flange Strain/Stress vs Time	
	Midpoint Moment vs Time	
Rain: Simulated 1-hr Event	Center Beam Displacements vs Time	<p>The characteristic increases linearly from zero, until a maximum is reached, and then proceeds to decrease nonlinearly, gradually appearing to approach a plateau. An example of the shape is shown below in Figure 32. As with the natural rain event, midpoint flange strain/stress and midpoint moment have a slightly different shape, increasing linearly</p>
	Midspan Displacements vs Time	
	Support Displacements vs Time	
	Midpoint Flange Strain/Stress vs Time	



### 4.3-Water Level

Downslope parapet wall water level vs time for the four tests is plotted in Figure 33, Figure 34, Figure 35, and Figure 36. Maximum water elevation was 7.51 inches and 7.54 inches for the flooding and uniform input ponding tests respectively.

Maximum water elevation for the natural rain even is 0.32 inches, while the maximum elevation for the 1-hr event is 0.97 inches. For all tests, behavior after the maximum water elevation is passed is nonlinear, and the rate of change of the water elevation appears to approach a plateau as time passes.

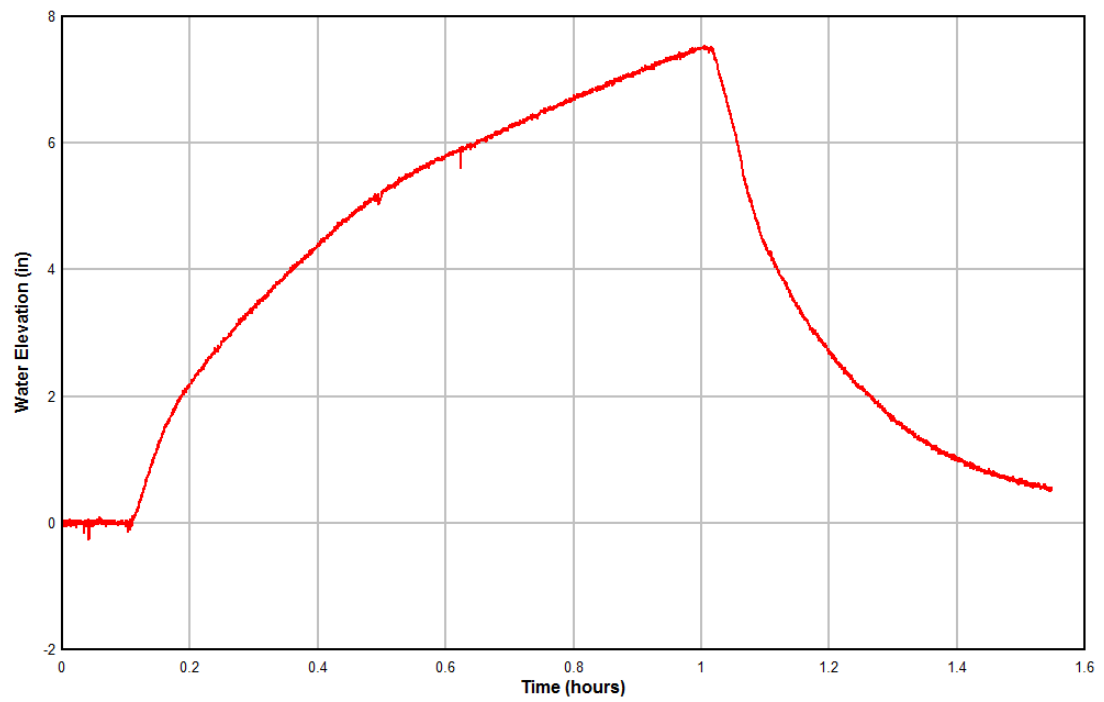


Figure 33: Downslope Parapet Wall Water Elevation (Ponding Flooding Input Test)

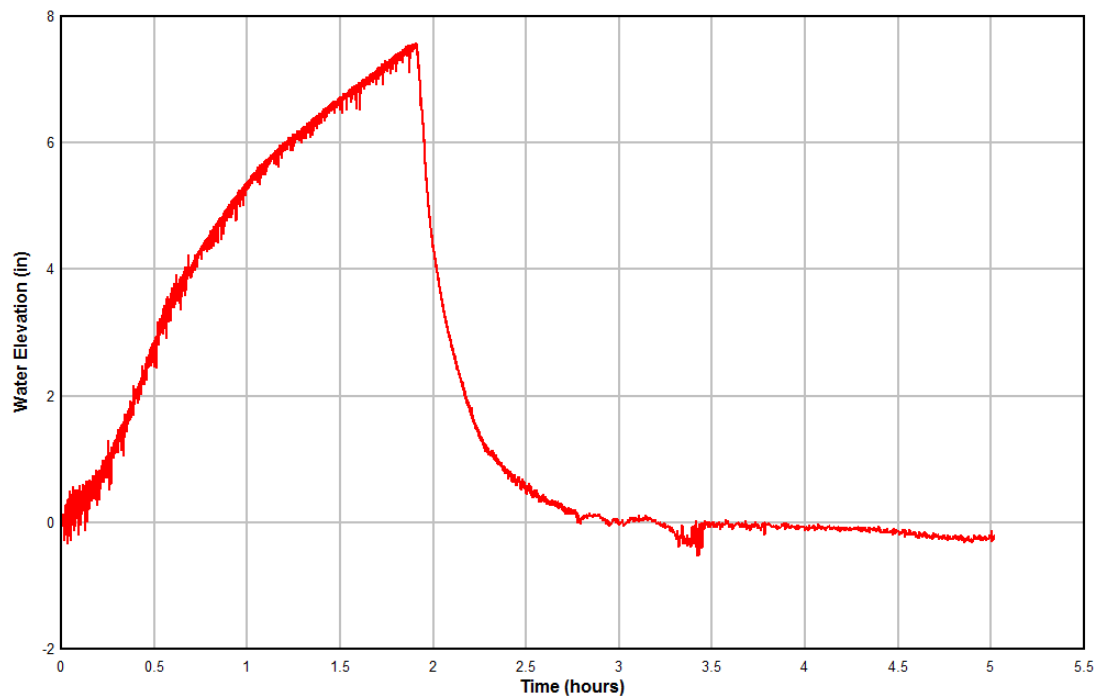


Figure 34: Downslope Parapet Wall Water Elevation (Ponding Uniform Input Test)

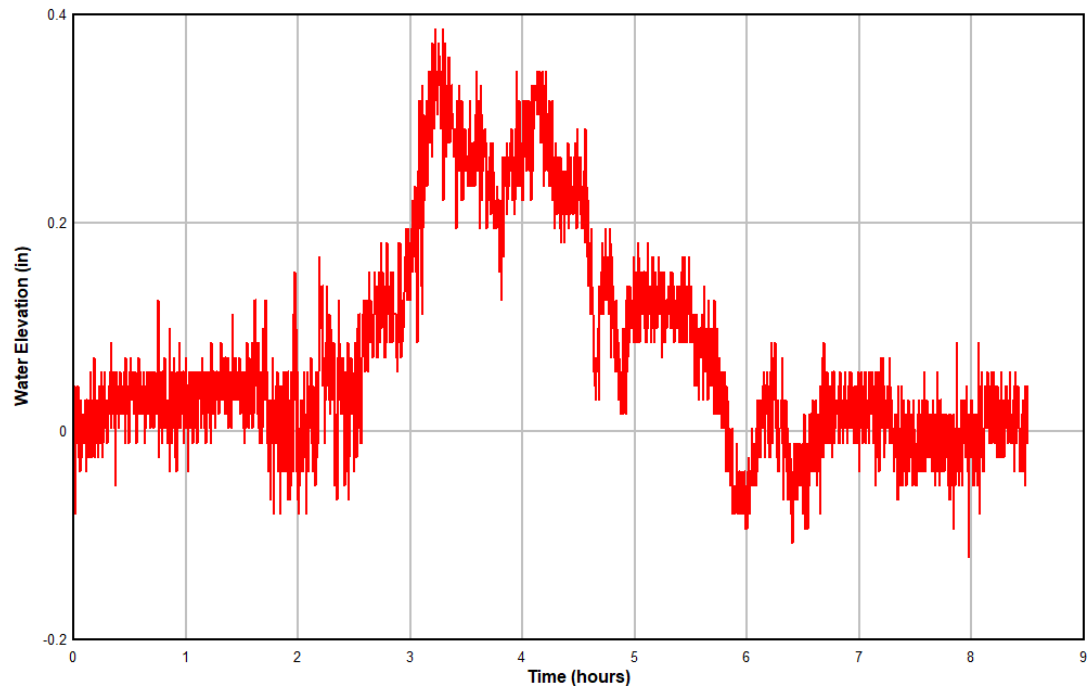


Figure 35: Downslope Parapet Wall Water Elevation (Natural Rain Event)

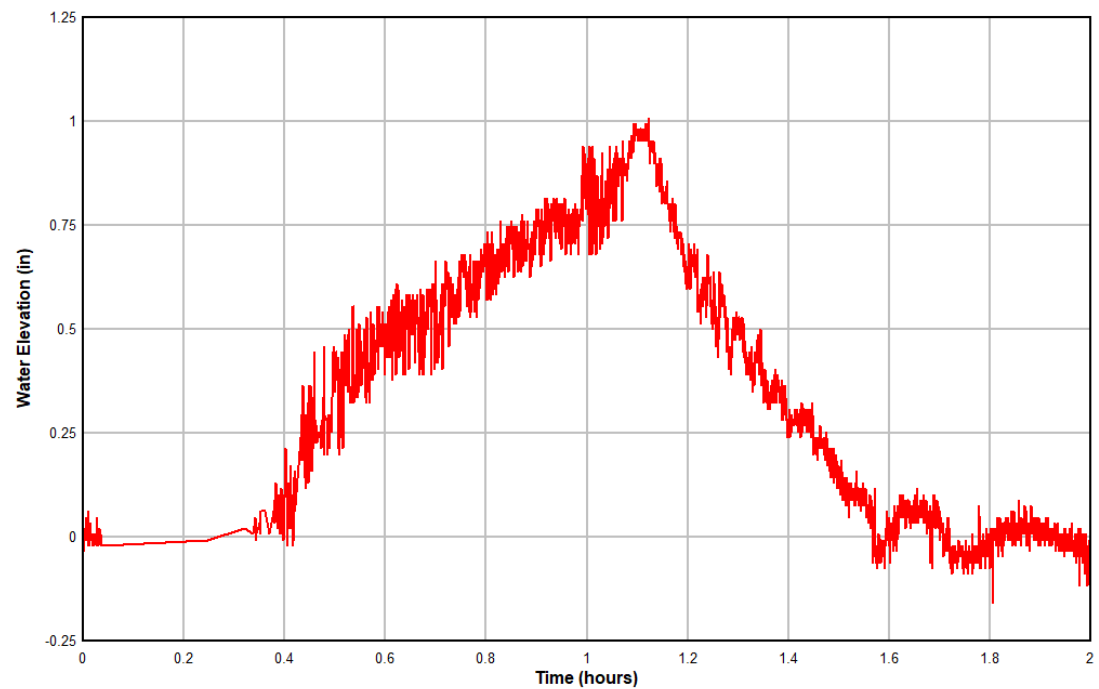


Figure 36: Downslope Parapet Wall Water Elevation (Simulated 1-hr Event)



#### 4.4-Soil Moisture Content

##### 4.4.1-Moisture Sensor Calibration

During the moisture sensor calibrations, surface saturation occurred at a volumetric water content between 0.521 and 0.527. Table 3 contains the readings that were used during sensor calibration.

Table 3: Soil Moisture Sensor Calibration Data

Sensor 1		Sensor 4		Sensor 5	
Reading	VWC	Reading	VWC	Reading	VWC
0.33	0	0.3136	0	0.3255	0
0.46	0.124018	0.4347	0.12504	0.4315	0.12504
0.614	0.244178	0.6349	0.25008	0.6027	0.25008
0.7353	0.368196	0.7741	0.375121	0.7474	0.375121
0.8203	0.493316	0.8174	0.500161	0.7857	0.500161
0.8228	0.521371	0.817	0.525499	0.7863	0.527152

##### 4.4.2-Soil Moisture Content

The primary difference between the two ponding tests resided in how the water was applied to the roofs. During the flooding input test, water flowed at an uncontrolled rate and filled the roof from the downslope, and during the uniform input test, water was evenly applied to the roof by the designed sprinkler system. The three moisture sensors that were collecting data were located at the downslope edge of the roof, the midpoint, and the  $\frac{3}{4}$  point.

Figure 37, Figure 38, Figure 41, and Figure 42 plot data from the flooding input ponding test., and concern soil moisture content throughout the duration of the test. When volumetric water content begins increasing, water has reached the bottom of the moisture

sensor. Figure 37 indicates that water is moving upslope over time, as evidenced by the time points where the VWC being measured by each sensor begins to rise sharply. Each sensor plateaus once the soil around it has become completely saturated, or attained the maximum water content permitted by the soil. Similar behavior is seen in Figure 38, with a minor difference seen in an immediate rise in the VWC of the  $\frac{3}{4}$  point sensor at the beginning of the test. Roof soil is not without moisture when testing begins, with Figure 37 and Figure 38 displaying initial VWCs ranging between 0.2312 and 0.277. Additionally, Figure 37 and Figure 38 show that saturation occurred at a higher VWC in tests than during sensor calibrations, with VWC readings at saturation ranging from 0.5542 to 0.5813. The range in VWC required to reach saturation is attributed to the variance associated with the soil.

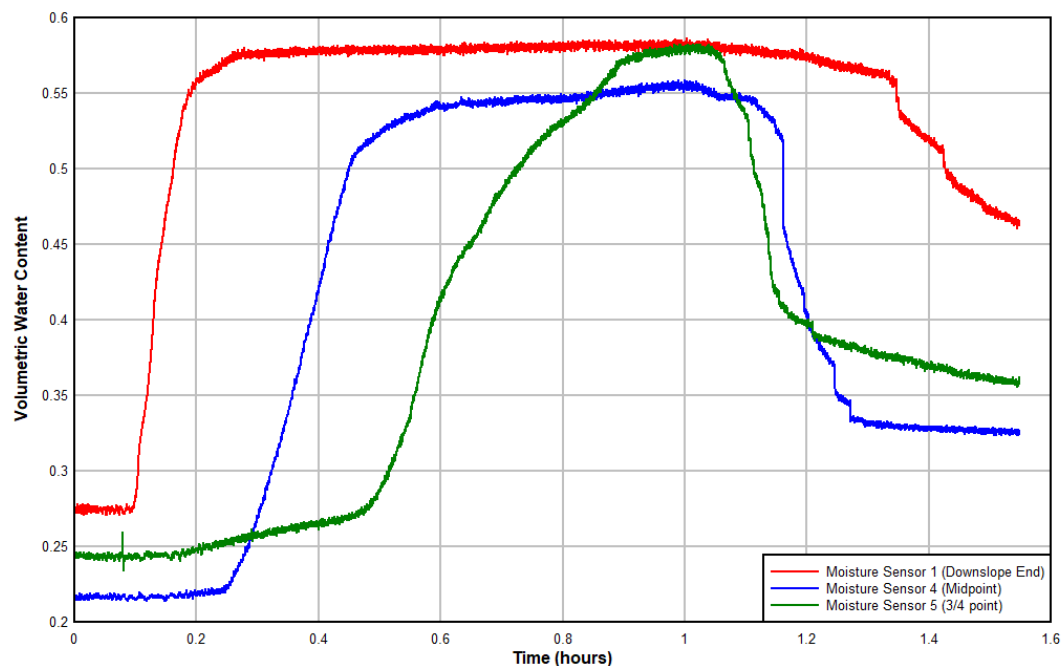


Figure 37: Non-zeroed Moisture Content vs Time (Ponding Flooding Input Test)

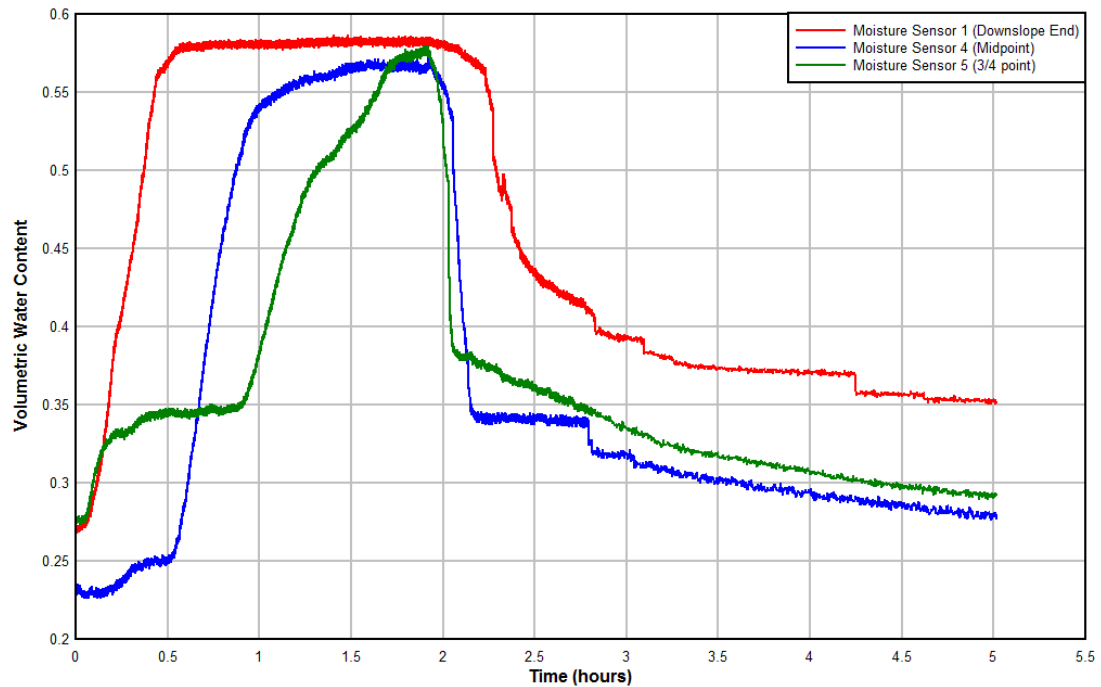


Figure 38: Non-zeroed Moisture Content vs Time (Ponding Uniform Input Test)

No saturation occurs in either rain event, with a peak VWC of 0.3127 being attained during the natural event, shown below in Figure 39, and a peak VWC of 0.4823 being attained during the 1-hr simulated event, shown in Figure 40. As with the ponding tests, the roof soil is not entirely dry when testing begins, with initial VWC values ranging from 0.2301 to 0.260 in the natural event, and 0.2816 to 0.3082 in the 1-hr simulated event. Despite not reaching saturation, VWC does reach a temporary state of equilibrium during the 3 to 4.5 hr interval in the natural event, while the downslope sensor and  $\frac{3}{4}$  point sensor indicate constant VWC during the intervals from 0.94 to 1.19 hrs and 0.49 to 1.04 hrs respectively during the 1-hr simulation. The presence of constant VWC below saturation indicates that steady state flow occurred during the aforementioned intervals.

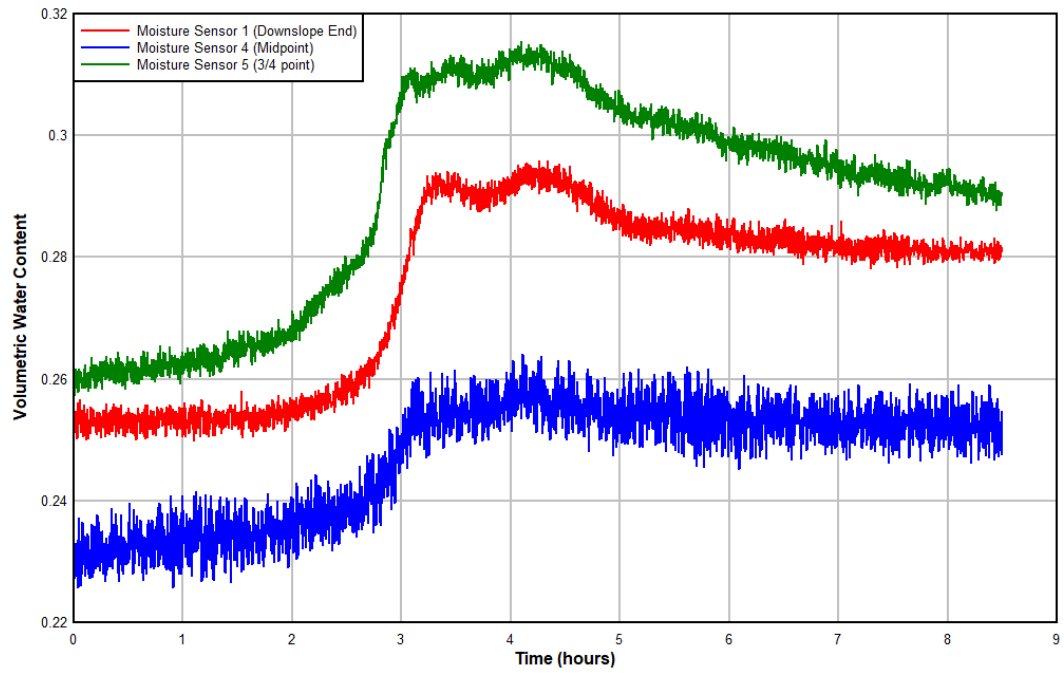


Figure 39: Non-zeroed Moisture Content vs Time (Natural Event Test)

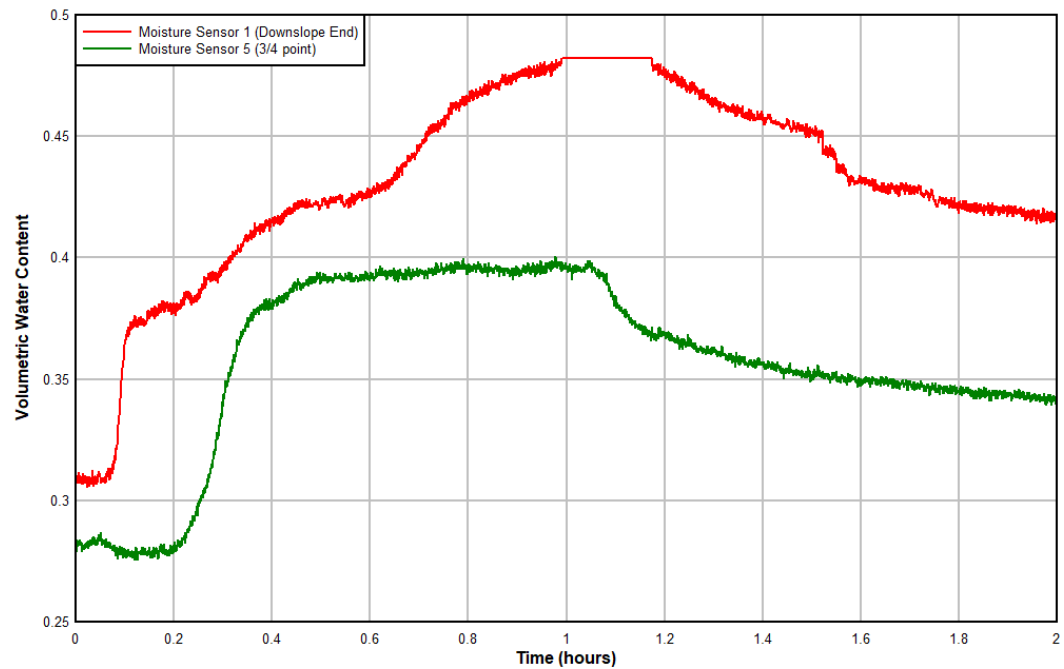


Figure 40: Non-Zeroed Moisture Content vs Time (Simulated 1-hr Rain Event Test)

Figure 41 and Figure 42 display volumetric water content vs time for the three sensors, with the data adjusted so that each sensor's readings begin at zero. The alignment of the data helps visualize the roof drainage process. Equating decreasing VWC with drainage, it can be seen that the roof drains from upslope down, as was expected. During the flooding input test, shown in Figure 41, the  $\frac{3}{4}$  point sensor,  $\frac{1}{2}$  point sensor, and downslope sensor indicate that desaturation occurs at 1.04, 1.11, and 1.34 hrs respectively. Meanwhile, during the uniform input test, shown in Figure 42, the  $\frac{3}{4}$  point,  $\frac{1}{2}$  point, and downslope sensors desaturated at 1.91, 1.93, and 2.08 hrs.

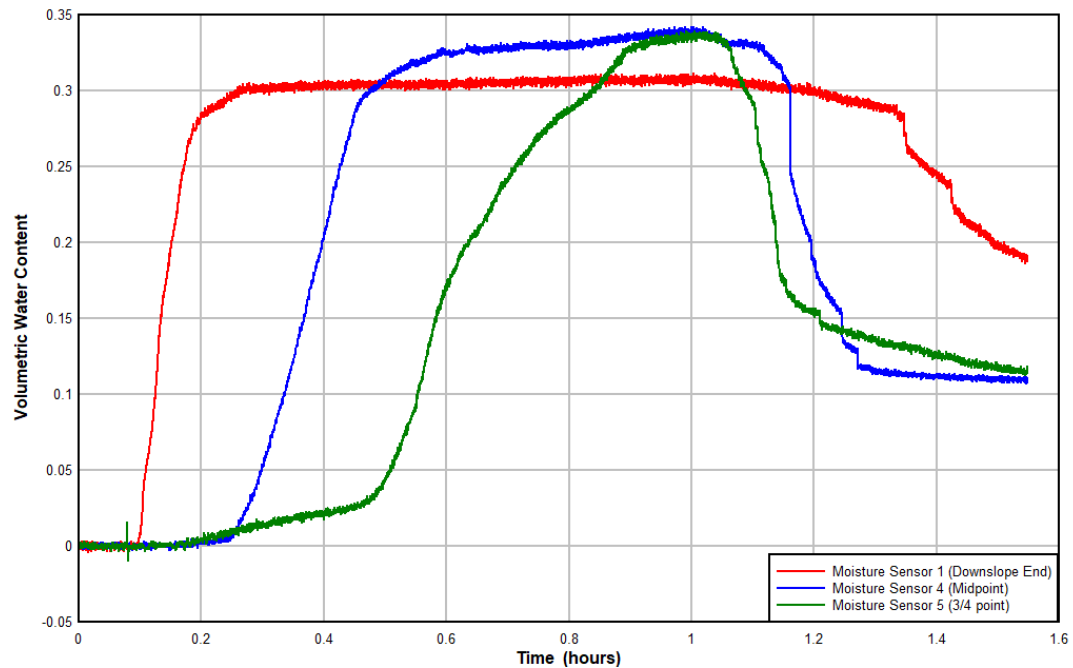


Figure 41: Zeroed Moisture Content vs Time (Ponding Flooding Input Test)

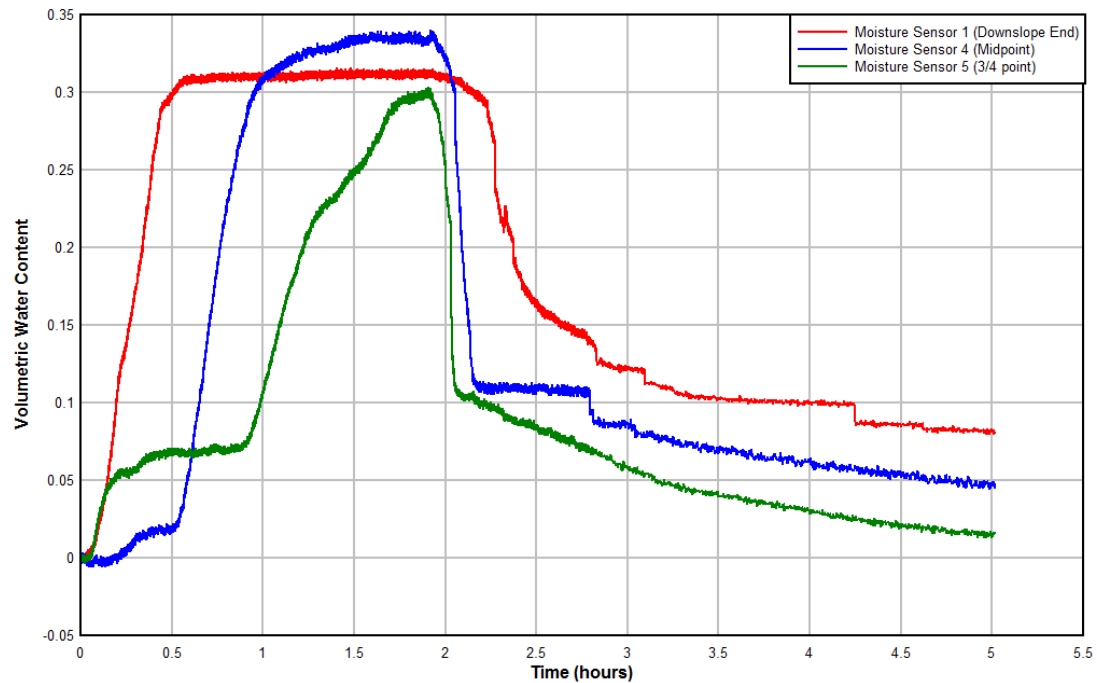


Figure 42: Zeroed Moisture Content vs Time (Ponding Uniform Input Test)

In Figure 43, the natural event is seen to have created a maximum change in VWC of 0.05297, which is small in comparison to the other events, with the 1-hr event, flooding input ponding event, and the uniform input ponding events creating maximum VWC changes of 0.17128, 0.3372, and 0.33465 respectively. It is unclear from the figure how long it would take for the VWC of the roof to return to its initial value, as residual VWC values are present at the end of the data collection interval, despite allowing for a drainage period of 3 hrs. It should be noted that these residual VWC values are small, ranging from 0.02 to 0.03.

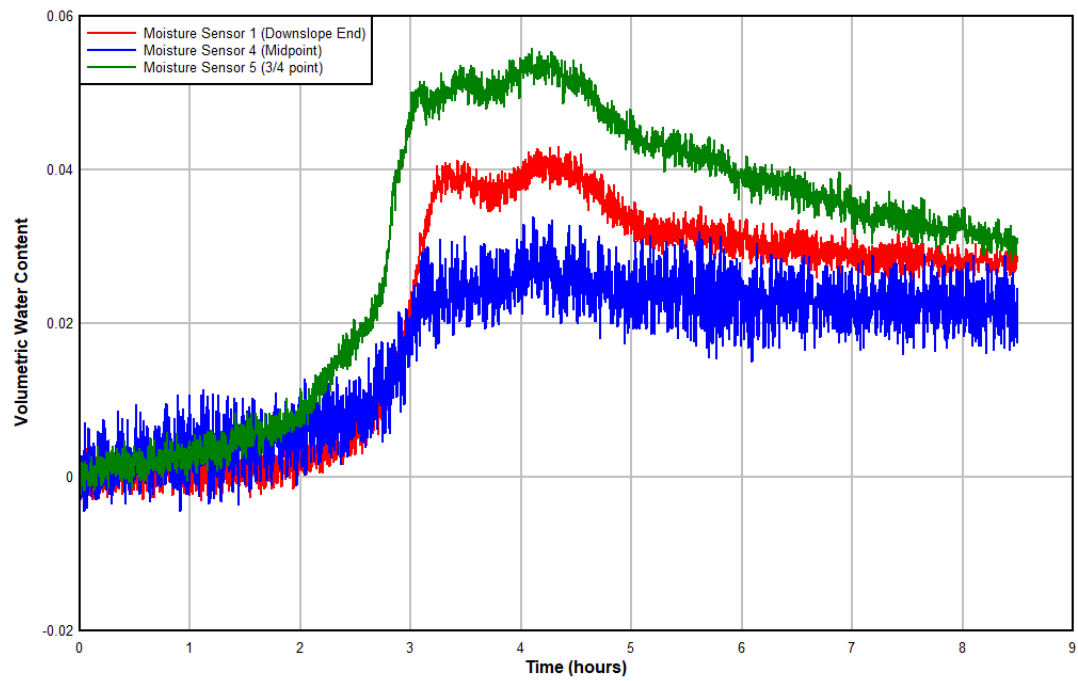


Figure 43: Zeroed Moisture Content vs Time (Natural Event Test)

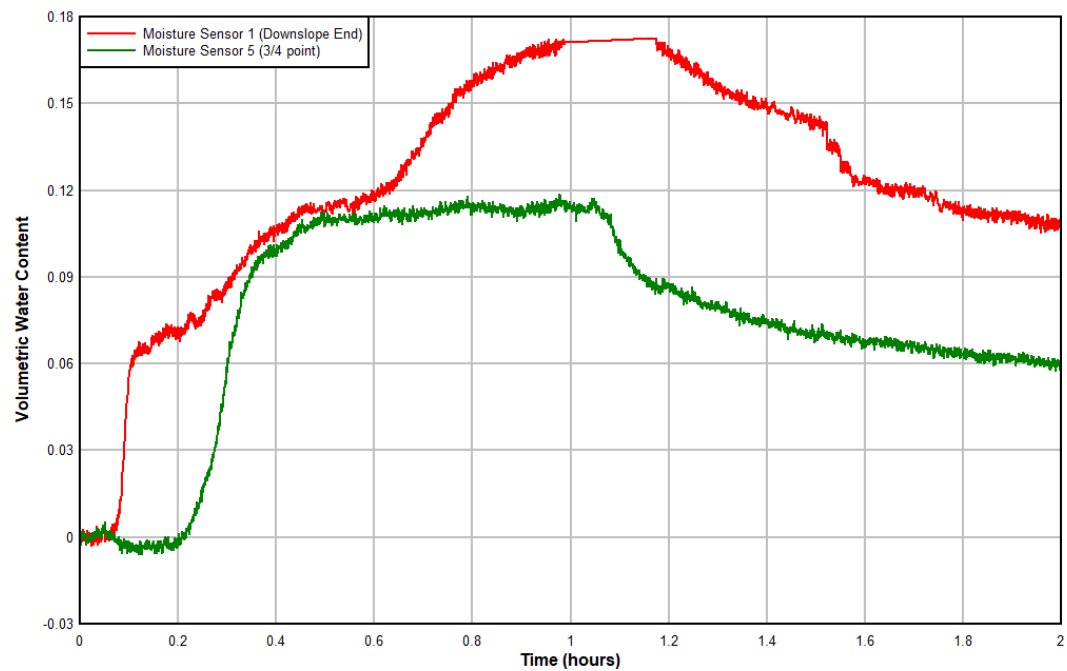


Figure 44: Zeroed Moisture Content vs Time (Simulated 1-hr Rain Event Test)



Figure 45 and Figure 46 plot VWC vs downslope parapet wall water elevation. Due to the roof slope, the bottom of each moisture sensor is at a differing elevation, 0.25 inches, 3.5 inches, and 5.25 inches, for the downslope, midpoint, and  $\frac{3}{4}$  point sensors respectively. VWC recorded by each sensor does not begin to substantially increase until the parapet wall water elevation is near the elevation of the bottom of the sensor. Once water reaches the sensor's bottom, VWC increases, tapering off as the water elevation reaches a height that coincides with saturation of the soil at the elevation where the sensor resides. As water level decreases, a new path is created. The VWC recorded by each sensor continues to indicate that the soil is saturated at lower parapet wall water elevations than were associated with saturation when the water elevation was increasing. This difference is because the water that resides along the parapet wall is not in the soil, and is able to drain more quickly. Consequently, the water elevation will fall to a lower level before the soil desaturates, in comparison to when saturation was initially occurring, and water was uniformly increasing with elevation. Due in part to the discrepancy between the rate free water outside the soil drains in comparison to the rate that water drains through the soil,

residual increases of VWC of about 0.14, 0.10, and 0.07 is present at the downslope, midpoint, and  $\frac{3}{4}$  points when the water elevation returns to zero.

Once the soil is no longer saturated, drainage occurs at approximately the same rate as saturation with the downslope soil.

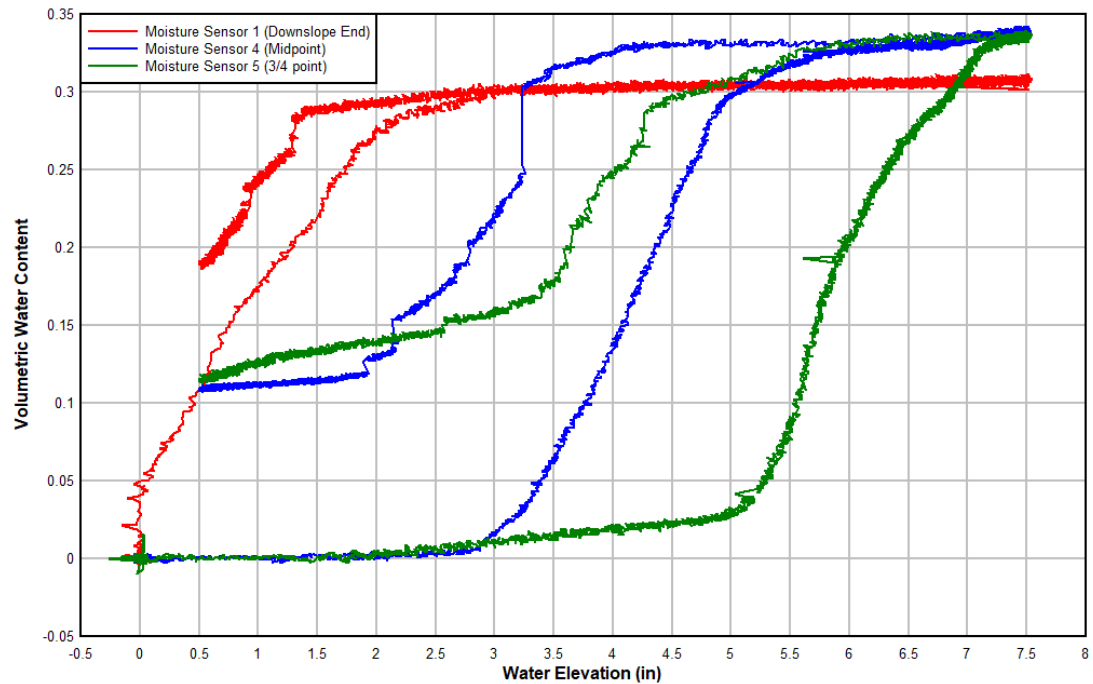


Figure 45: Zeroed Moisture Content vs Downslope Parapet Wall Water Elevation (Ponding Flooding Input Test)

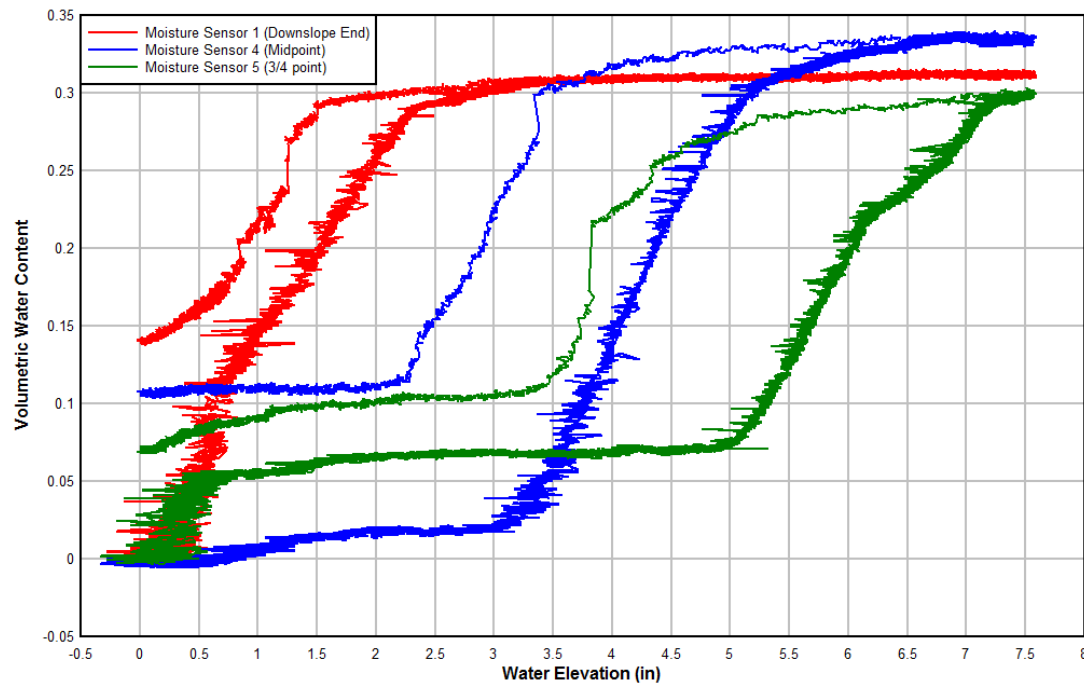


Figure 46: Zeroed Moisture Content vs Downslope Parapet Wall Water Elevation (Ponding Uniform Input Test)

#### 4.1 – Displacements

##### 4.1.1-Primary Beam Displacements

Displacements for flooding input and uniform input ponding tests, shown below in Figure 47 and Figure 48 respectively, increase linearly as water is added to the roof. Midpoint displacement was largest, while  $\frac{1}{4}$  and  $\frac{3}{4}$  displacements were of similar magnitude, with the  $\frac{3}{4}$  displacement being slightly larger. Once roof began draining, displacements decreased, with rate of decrease tapering off, and in the case of the uniform input test, assumed a linear decrease that caused the roof to return to a non-displaced state 3 hours after draining had commenced.

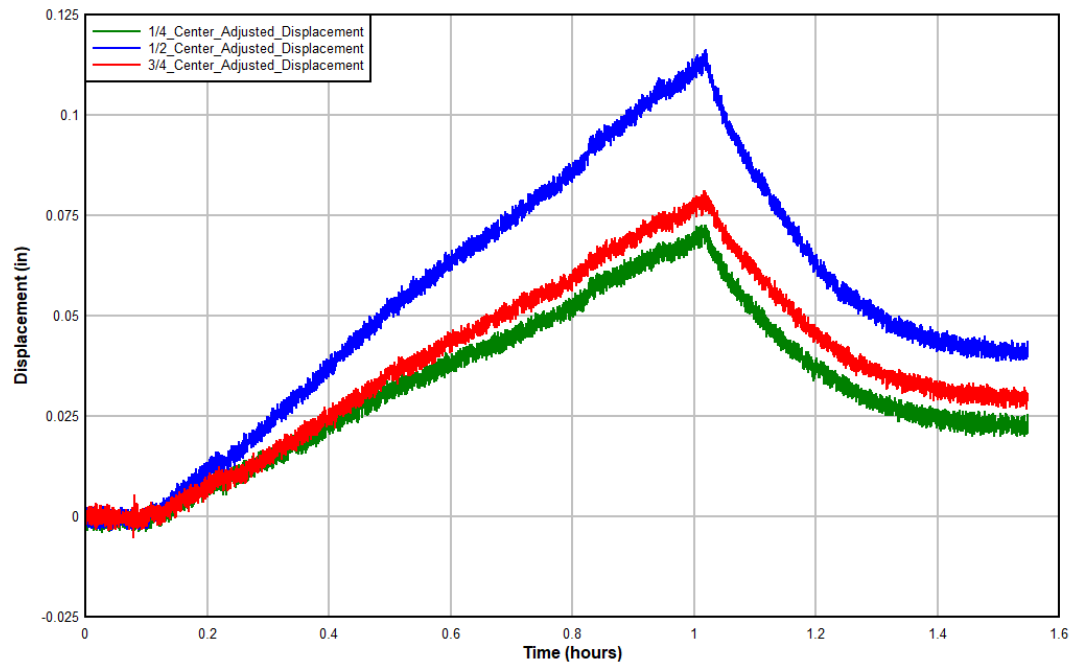


Figure 47: Displacement vs Time (Ponding Flooding Input Test)

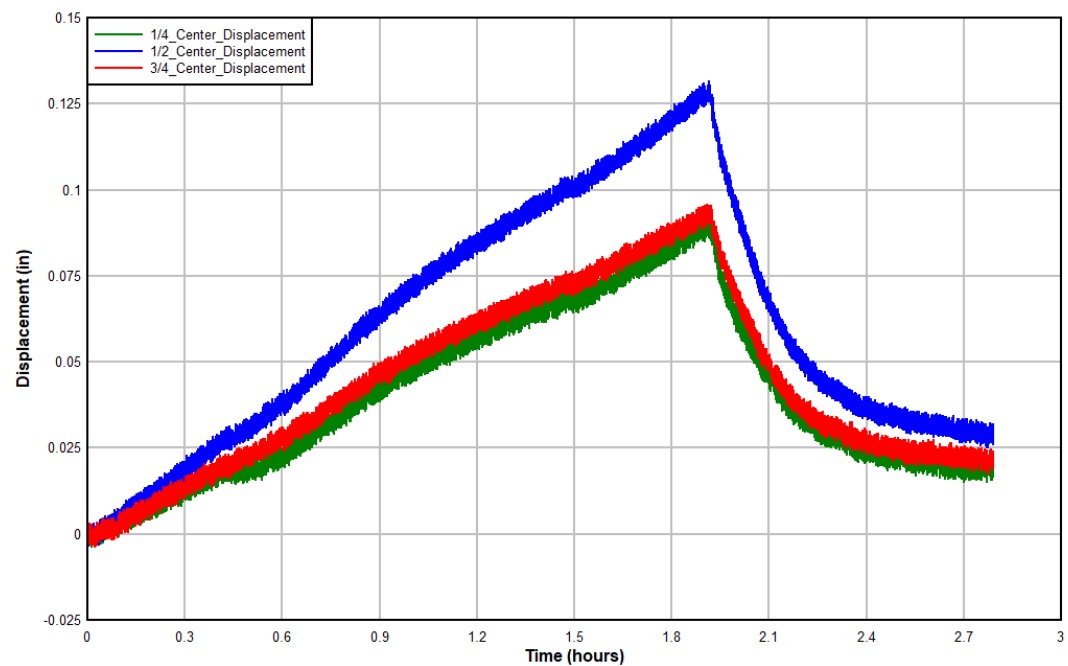


Figure 48: Displacement vs Time (Ponding Uniform Input Test)

As with the ponding tests, the midpoint displacements from the rain events, both natural and simulated, were largest.  $\frac{3}{4}$  point displacement was slightly larger than  $\frac{1}{4}$  point

magnitude, 0.0078 in to 0.0106 in during the during the natural event, and 0.0146 in to 0.0173 in during the 1-hr simulation. As opposed to the simulated tests (ponding and the 1-hr event), the maximum displacements during the natural event are a plateau rather than a point. Both rain events also lack the initial period where displacement decreases rapidly immediately after drainage commences. This could be due to a lack of free water outside the ecoroof soil, forcing all water that drains to reach the drain by traveling through the soil.

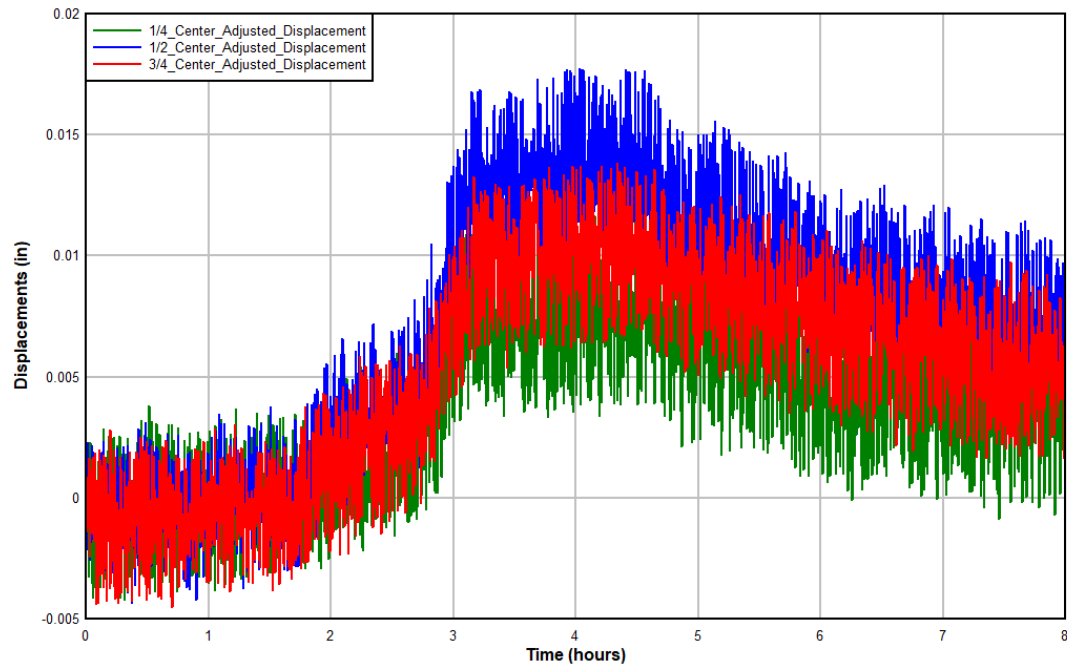


Figure 49: Displacement v Time (Natural Rain Event)

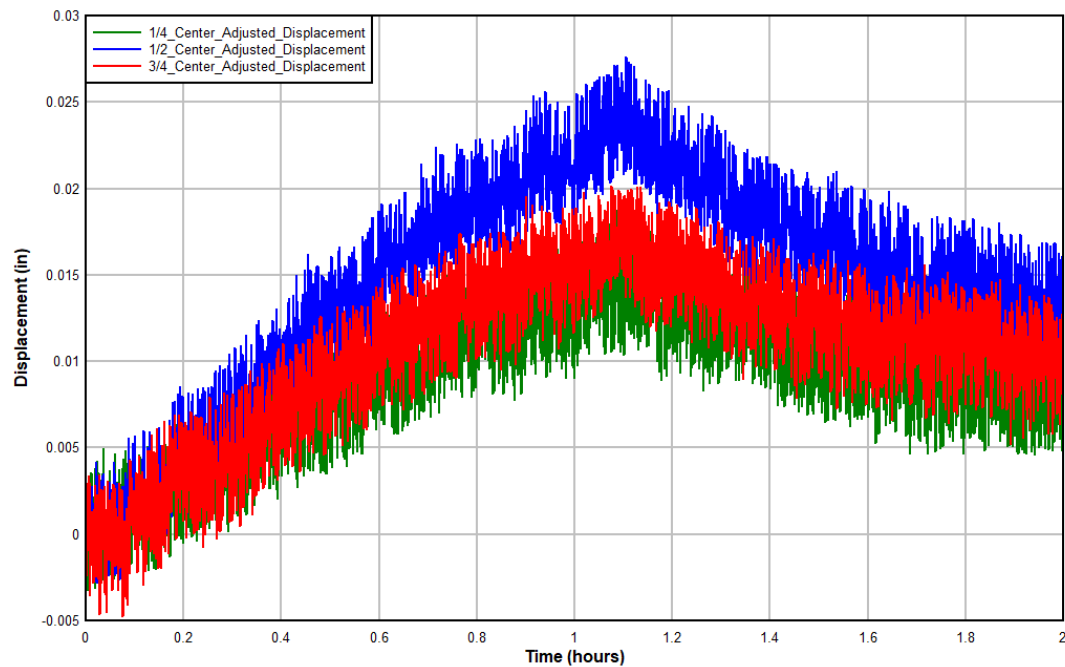


Figure 50: Displacement vs Time (Simulated 1-hr Rain Event)

Figure 51 and Figure 52 display displacement vs downslope parapet wall water elevation, for the flooding input ponding test and uniform input ponding test respectively. As water elevation at the parapet wall increases, rate of displacement also increases. However, as drainage occurs and the parapet wall water elevation decreases, displacement decreases at a smaller, more linear rate in comparison to its increase. As the water elevation reaches zero, displacement remains positive in both tests, with 0.037 inches of residual midpoint displacement in the flooding input test and 0.023 inches of residual midpoint displacement in the uniform input test. As with the residual VWC discussed earlier, the appearance of residual displacement in the figures is due to the water that rests against the downslope parapet wall draining at a faster rate than the water that was added to the soil, causing the drainage of added water to still be incomplete at the time when all standing water outside the soil has drained. While drainage continued past the time interval shown here, a lack of

temperature correction made it impossible to ensure the accuracy of the data outside of the displayed interval.

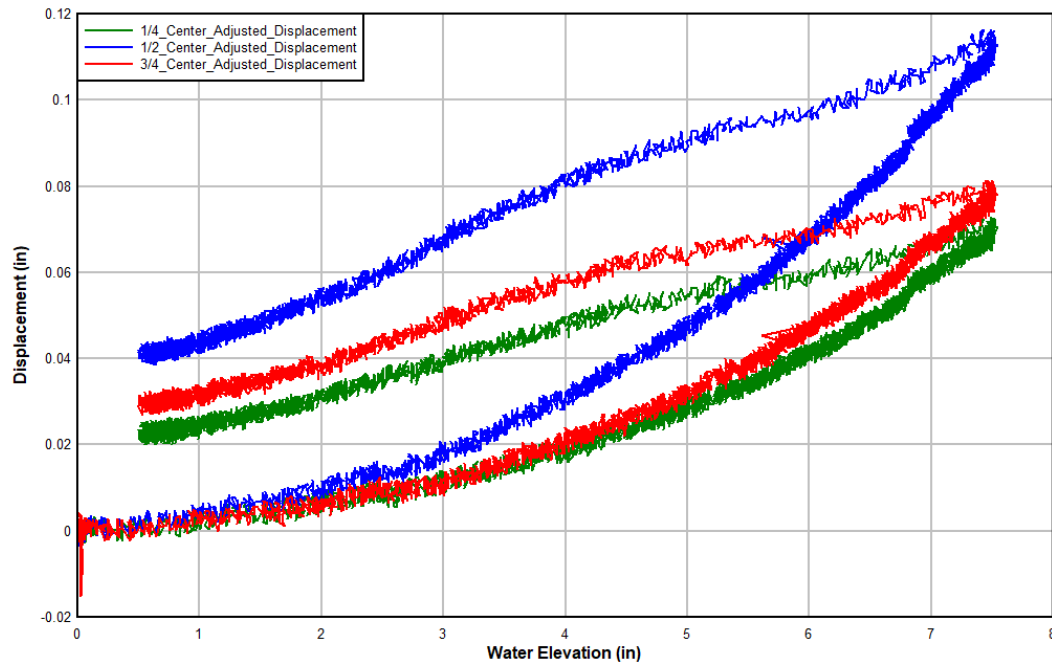


Figure 51: Displacement vs Downslope Parapet Wall Water Elevation (Ponding Flooding Input Test)



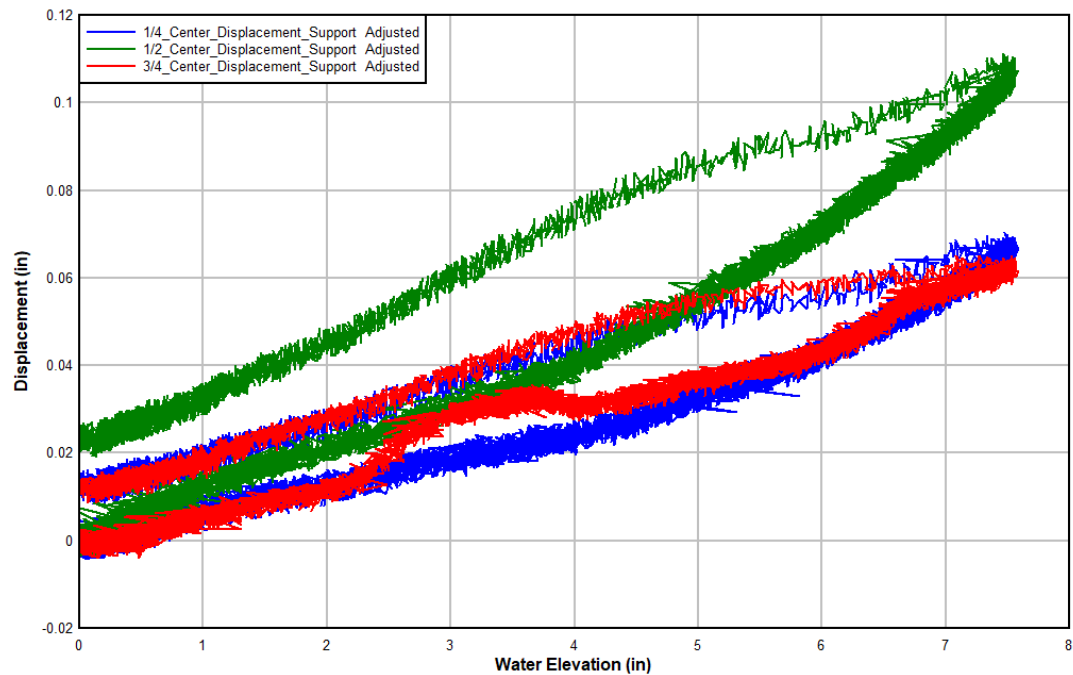


Figure 52: Displacement vs Downslope Parapet Wall Water Elevation (Ponding Uniform Input Test)

#### 4.1.2-Midspan Displacements

Figure 53 and Figure 54 display midspan displacements vs time of the three roof beams for the ponding tests. East beam and West beam displacements are equivalent, with center beam displacement being larger than both. When support displacements are removed from center beam displacements, the three have approximately equivalent magnitudes during the flood input ponding test. However, during the uniform input ponding test, center beam displacement remains larger than east and west displacements, indicating that some two-way bending is present.

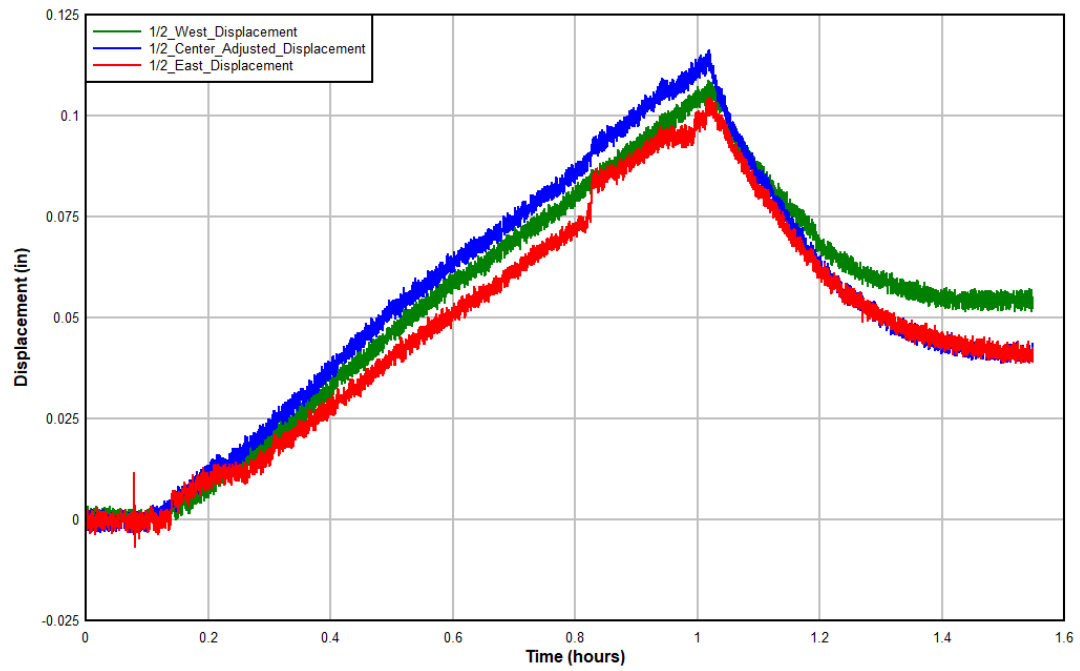


Figure 53: Midspan Displacements vs Time (Ponding Flooding Input Test)

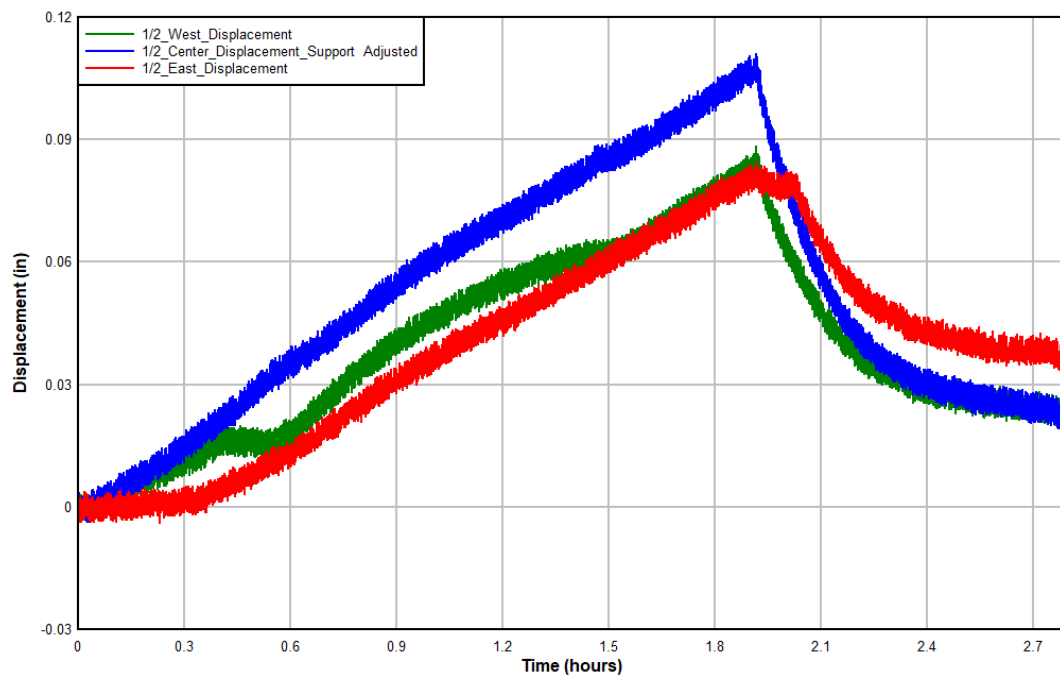


Figure 54: Midspan Displacements vs Time (Ponding Uniform Input Test)

Figure 55, and Figure 56 display midspan displacements vs time for the natural and simulated rain events. During data collection, the string pot associated with the east beam midpoint proved to be less sensitive to smaller displacements than the center and west beam string beam strings, and consequently did not read any displacement in during the rain event tests. Despite this, the string pot is still functioning, because while it did not return for the natural rain event on December 19<sup>th</sup>, reliable data is returned for the ponding test on December 20<sup>th</sup>. As with the ponding midspan displacements, center beam displacement is larger than west displacement, indicating the presence of some two-way bending.

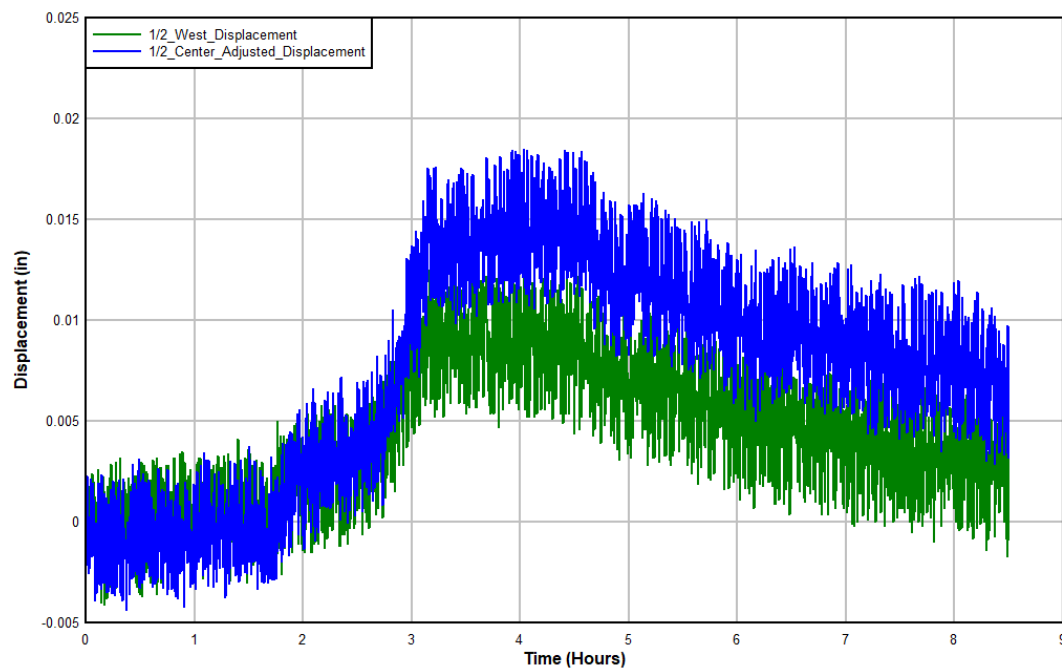


Figure 55: Midspan Displacements vs Time (Natural Event Test)

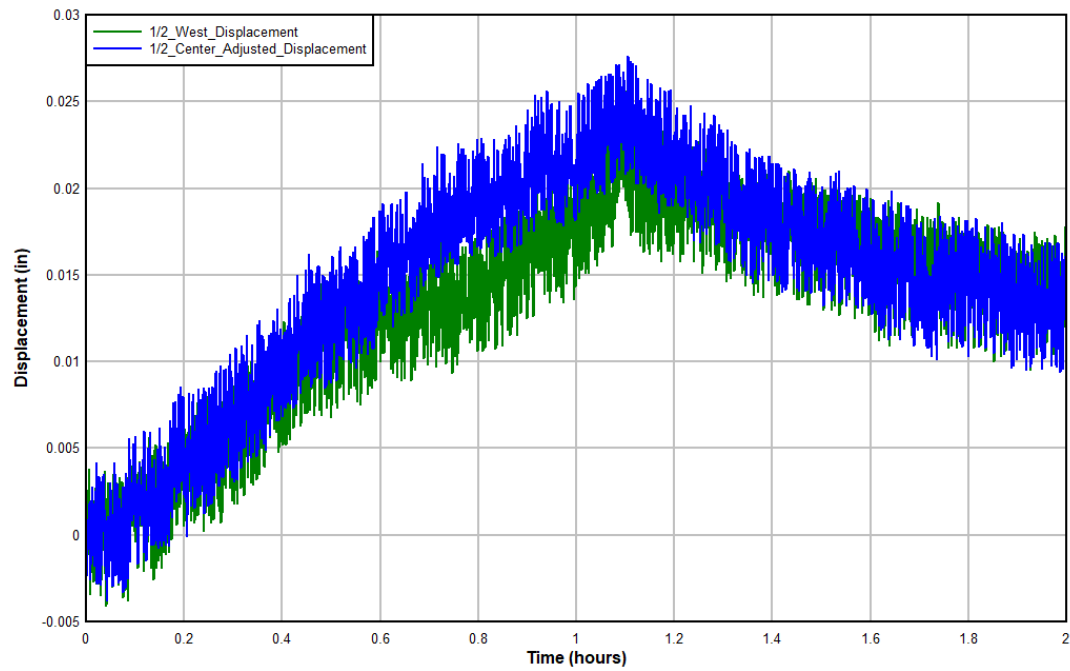


Figure 56: Midspan Displacements vs Time (Simulated 1-hr Rain Event Test)

Figure 57 and Figure 58 plot midspan displacement vs downslope parapet wall water elevation for the two ponding tests. Residual displacements for the center beam after water elevation returns to zero are larger during the flooding input ponding event than during the uniform input event, with center beam residuals ranging from 0.031 to 0.054 in and 0.023 to 0.37 in for the two respective tests.

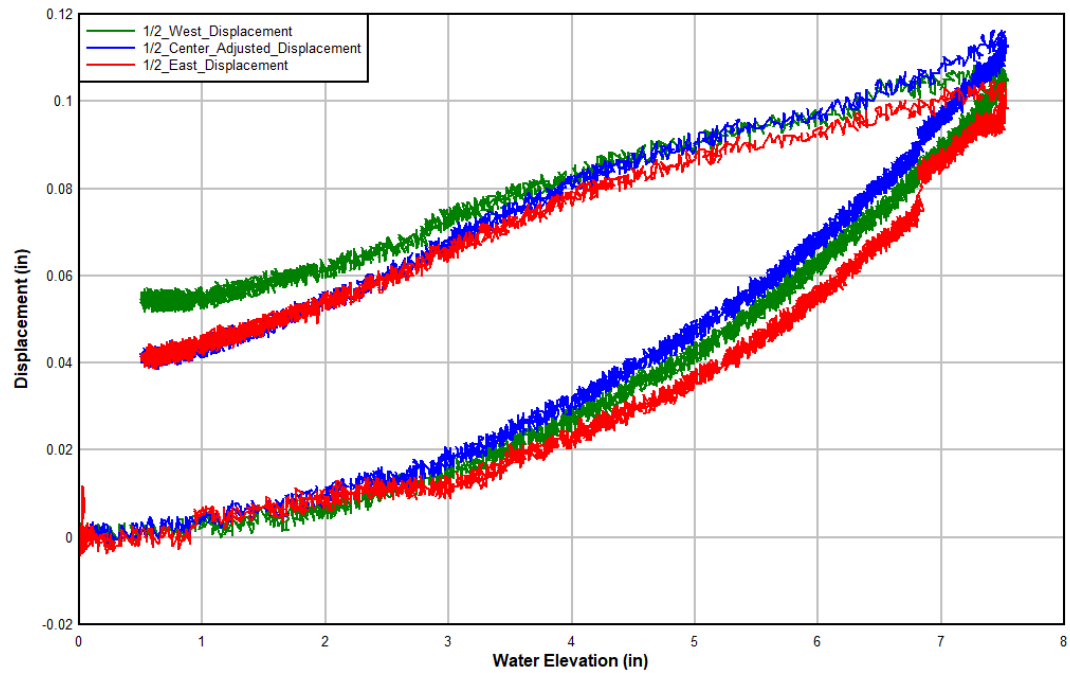


Figure 57: Midspan Displacements vs Downslope Parapet Wall Water Elevation (Ponding Flooding Input Test)

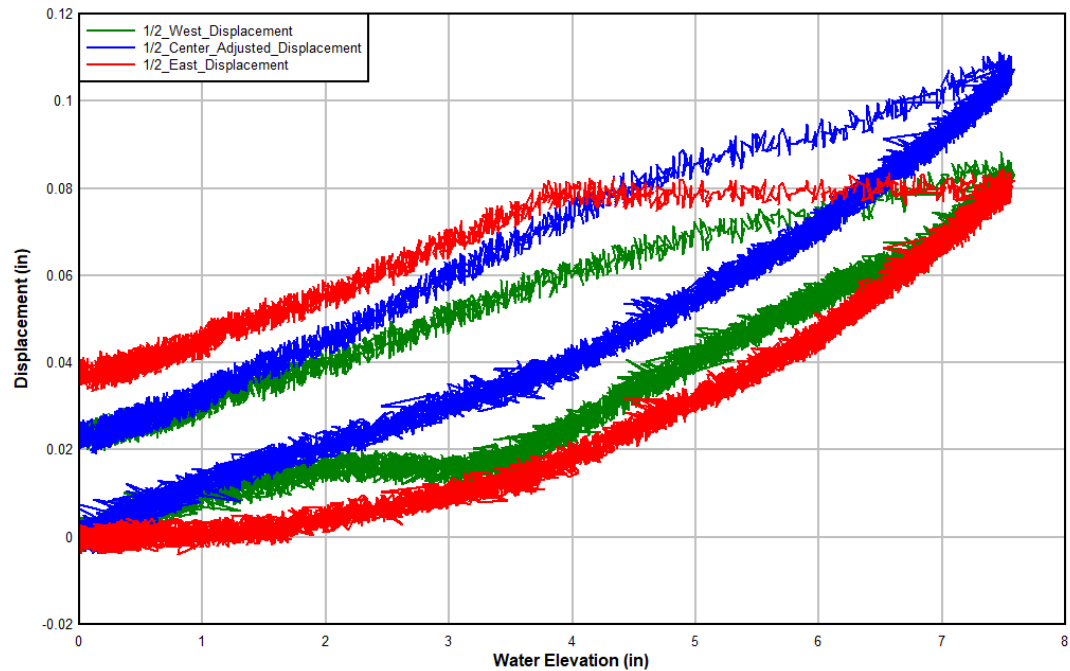


Figure 58: Midspan Displacement vs Downslope Parapet Wall Water Elevation (Ponding Uniform Input Test)

#### 4.1.3-Support Displacements

Displacements for the supports holding the center beam were tracked, and were used to remove rigid body motion from the displacement measurements. As can be seen in Figure 59, the support displacements vs time for the flood input ponding test and Figure 60, the support displacements for the uniform input ponding test, the south support, which corresponds to the downslope end of the roof, displaces at a faster rate than the north support (0.0406 in/hr and 0.0214 in/hr for the south and north supports respectively during the flooding input ponding test) and experiences more displacement than the north support, as would be expected on a sloped roof. Additionally, it is clear that load effects are not constrained purely to the roof itself, with the south supports experiencing between 20 and 25% of the displacement seen at the midpoint.

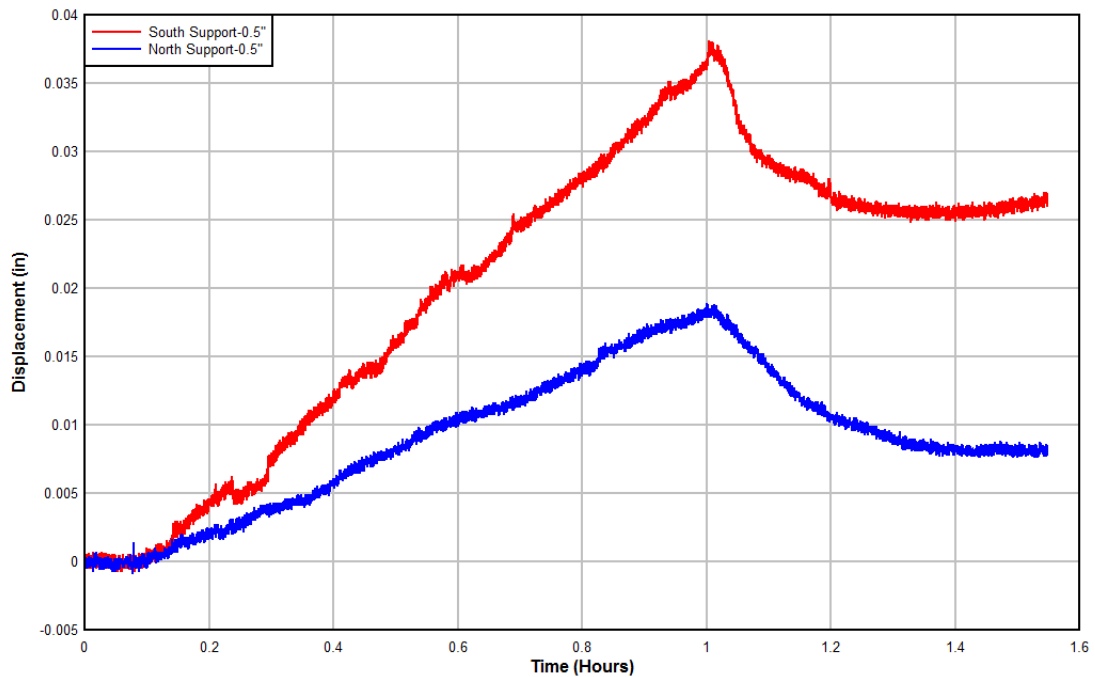


Figure 59: Support Displacements vs Time (Ponding Flooding Input Test)

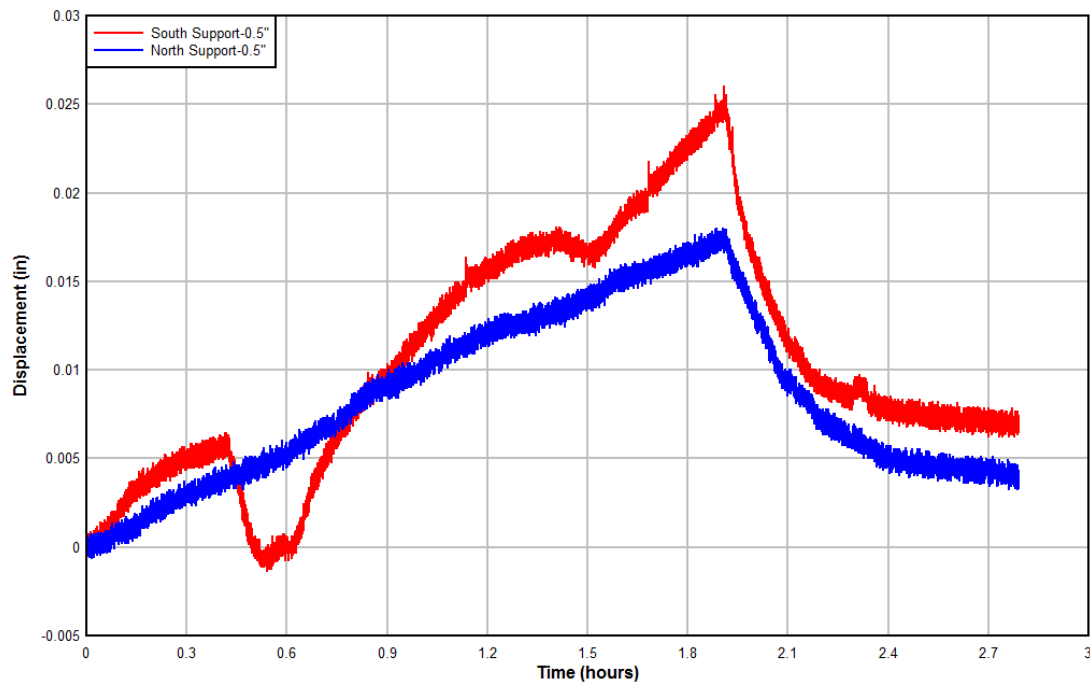


Figure 60: Support Displacements vs Time (Ponding Uniform Input Test)

#### 4.4-Primary Member Forces

##### 4.4.1-Midspan Flange Strain and Stress

A small amount of strain and stress was exerted on the structure throughout the tests, with midpoint flange stress reaching a maximum value of 3.40 ksi in the flooding input ponding test, shown below in Figure 61. Stress was smaller during the uniform input ponding test, reaching a maximum value of 2.90 ksi. Smaller stresses were produced during the rain events, where free drainage was allowed, with stress reaching a maximum value of 0.435 ksi during the natural event, seen in Figure 63 and 0.725 ksi during the simulated 1-hr event, seen in Figure 64. Residual stresses were present at the end of the data collection intervals, ranging from 0.2 to 08 ksi.



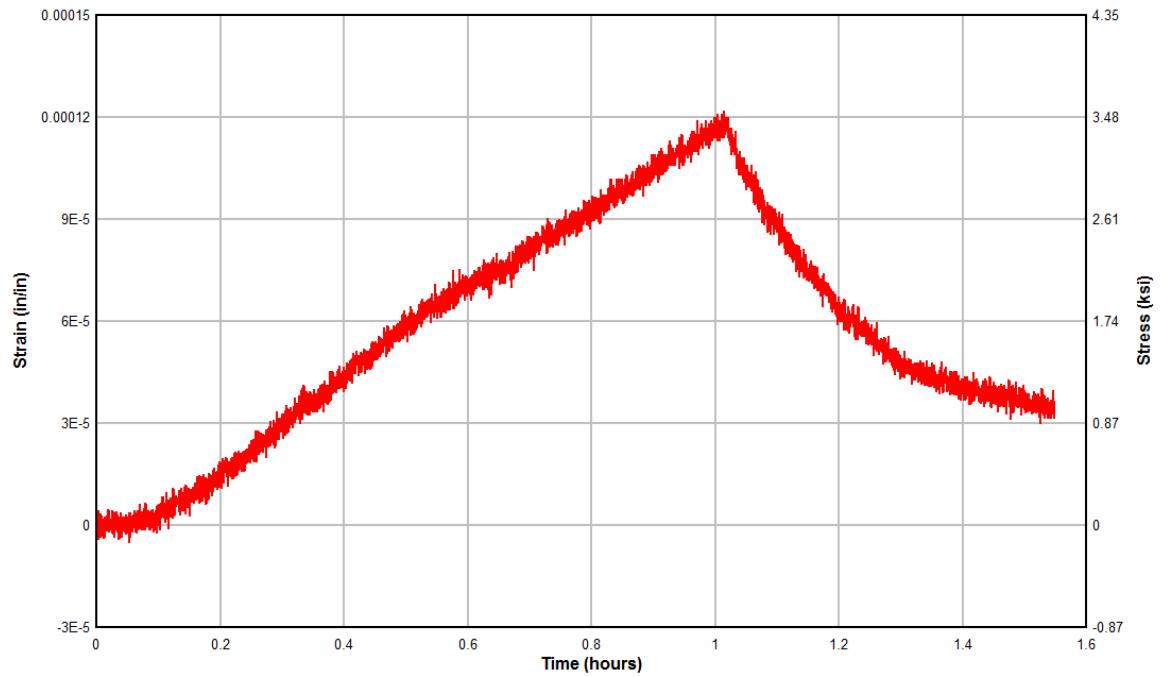


Figure 61: Midspan Bottom Flange Stress/Strain vs Time (Ponding Flooding Input Test)

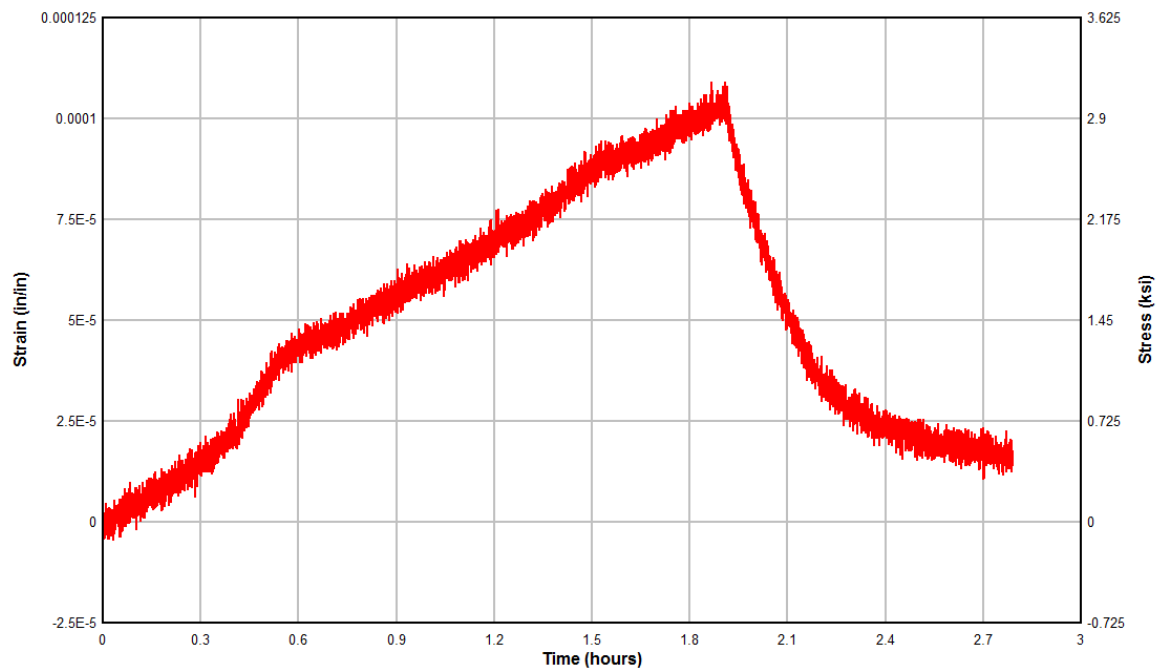


Figure 62: Midspan Bottom Flange Stress/Strain vs Time (Ponding Uniform Input Test)

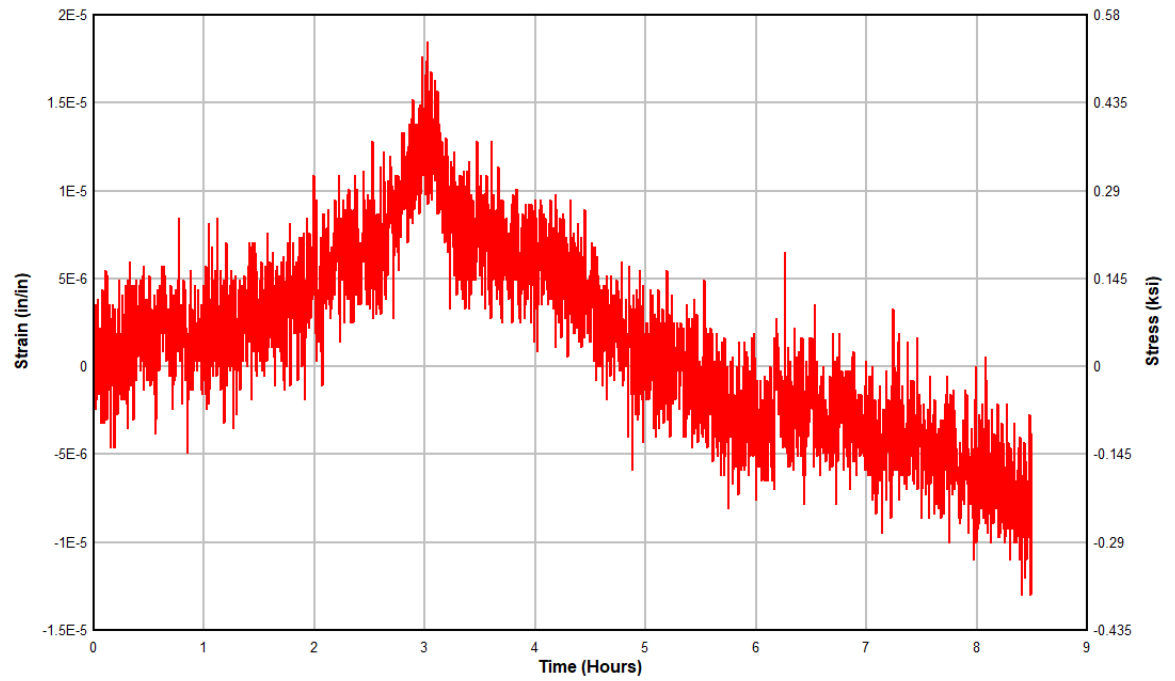


Figure 63: Midspan Bottom Flange Stress/Strain vs Time (Natural Event Test)

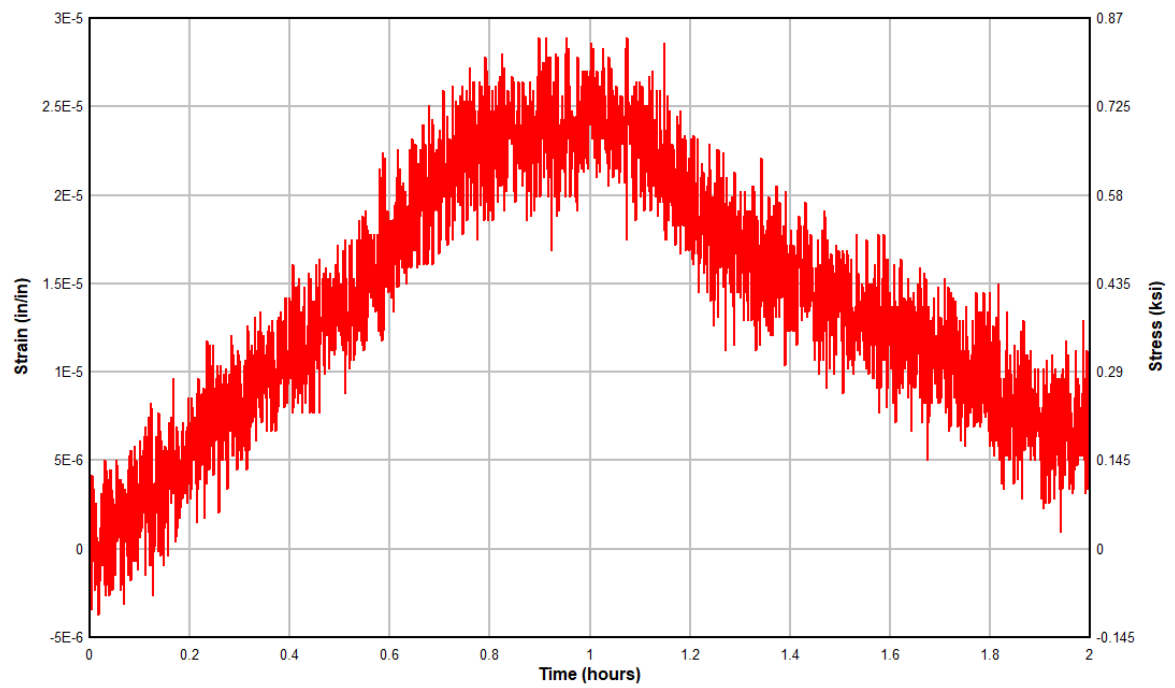


Figure 64: Midspan Bottom Flange Stress/Strain vs Time (Simulated 1-hr Rain Event Test)

#### 4.4.2-Midpoint Moment

Moment vs time for the two ponding experiments is shown below in Figure 65 and Figure 66. Both experiments have similar maximum moments; maximum moment for the flooding input test was 103.6 k-in, while maximum moment for uniform input was 93.1 k-in. This discrepancy could be attributed to the variation in the application of loading between the two tests, as a similar amount of water was applied to the roof during both tests, with downslope parapet wall water elevation reaching 7.50 inches during the flood input test and 7.52 inches during the uniform input test.

Maximum moment that occurred during the free draining rain events ranged from 15.8 k-in during the natural event to 27.9 k-in during the simulated 1-hr rain event, as seen in Figure 67 and Figure 68 respectively.

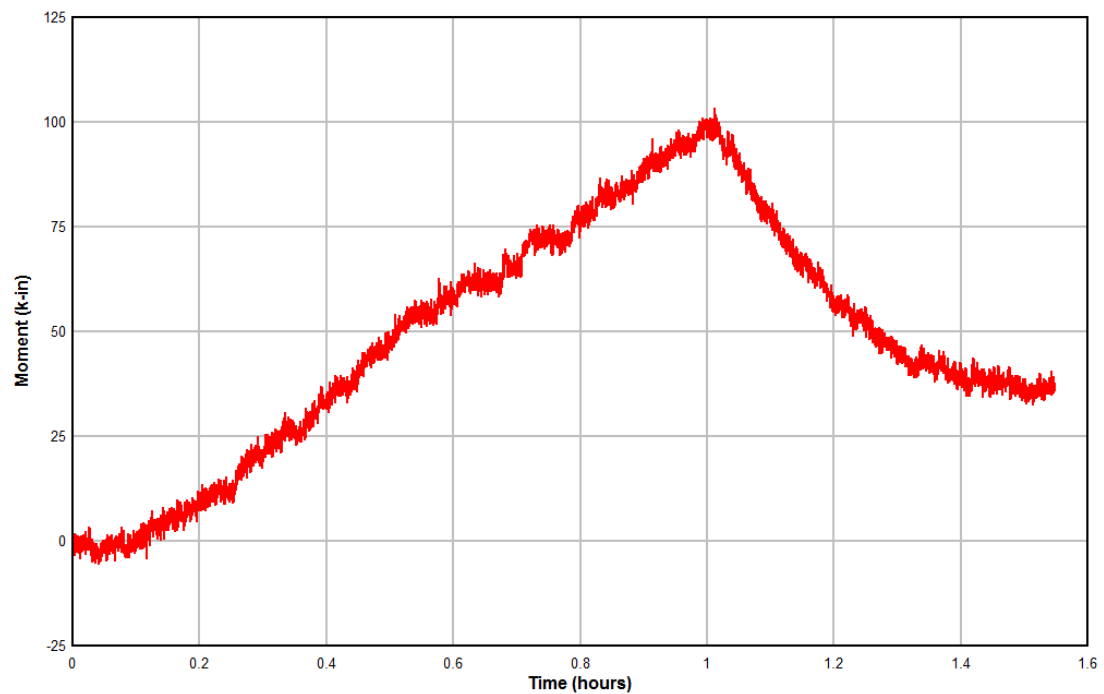


Figure 65: Midpoint Moment vs Time (Ponding Flooding Input Test)

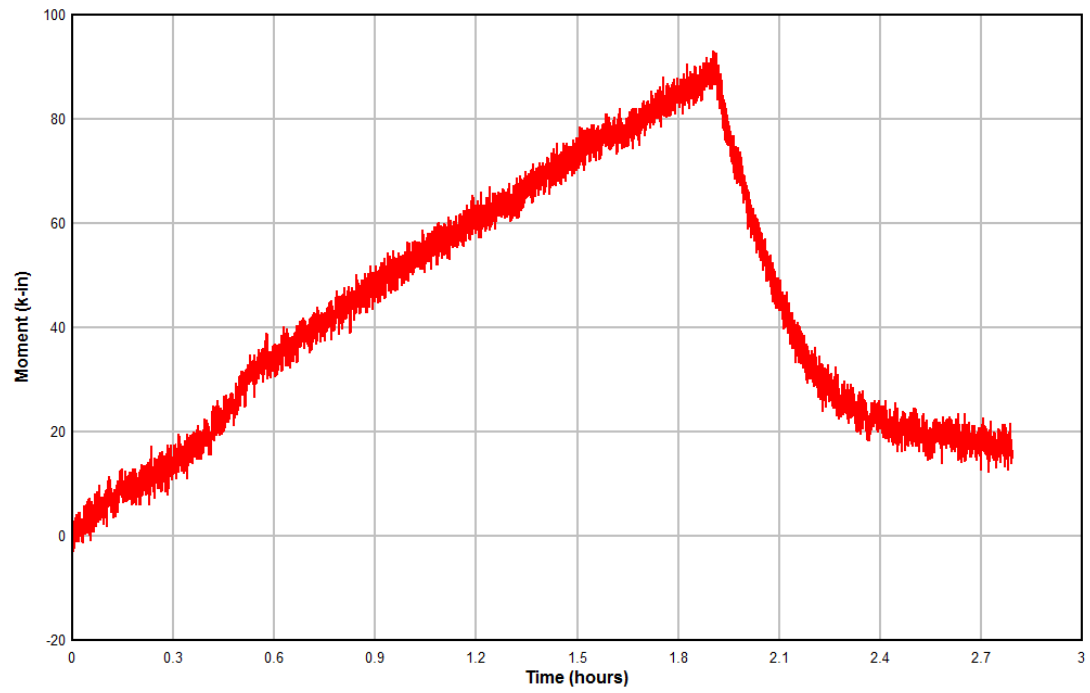


Figure 66: Midpoint Moment vs Time (Ponding Uniform Input Test)

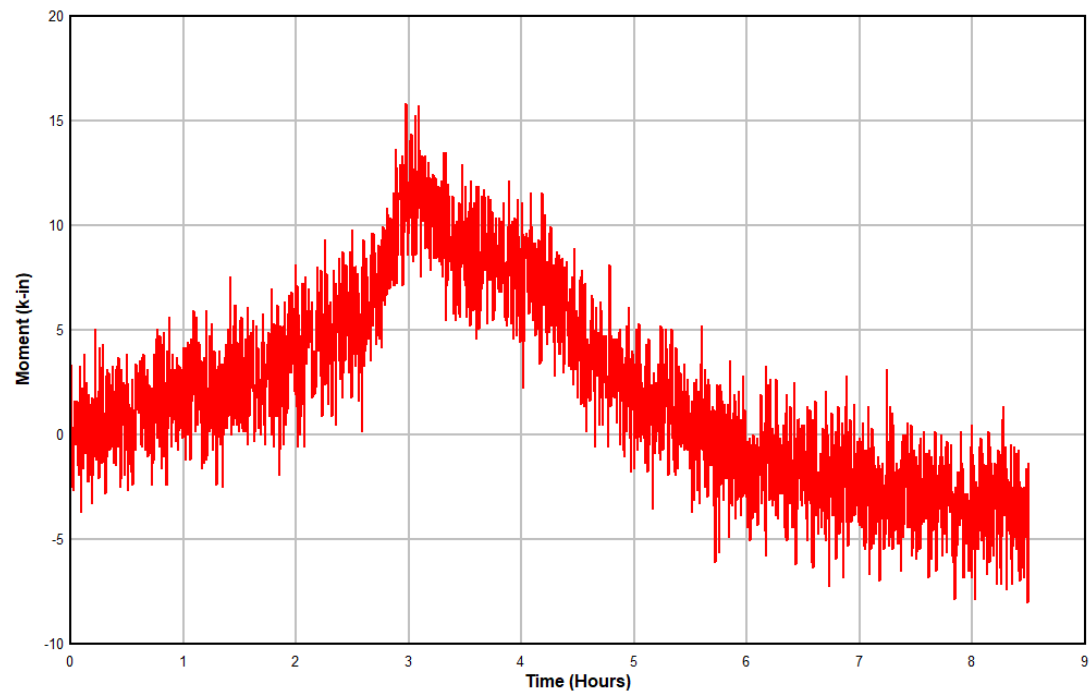


Figure 67: Midpoint Moment vs Time (Natural Event Test)

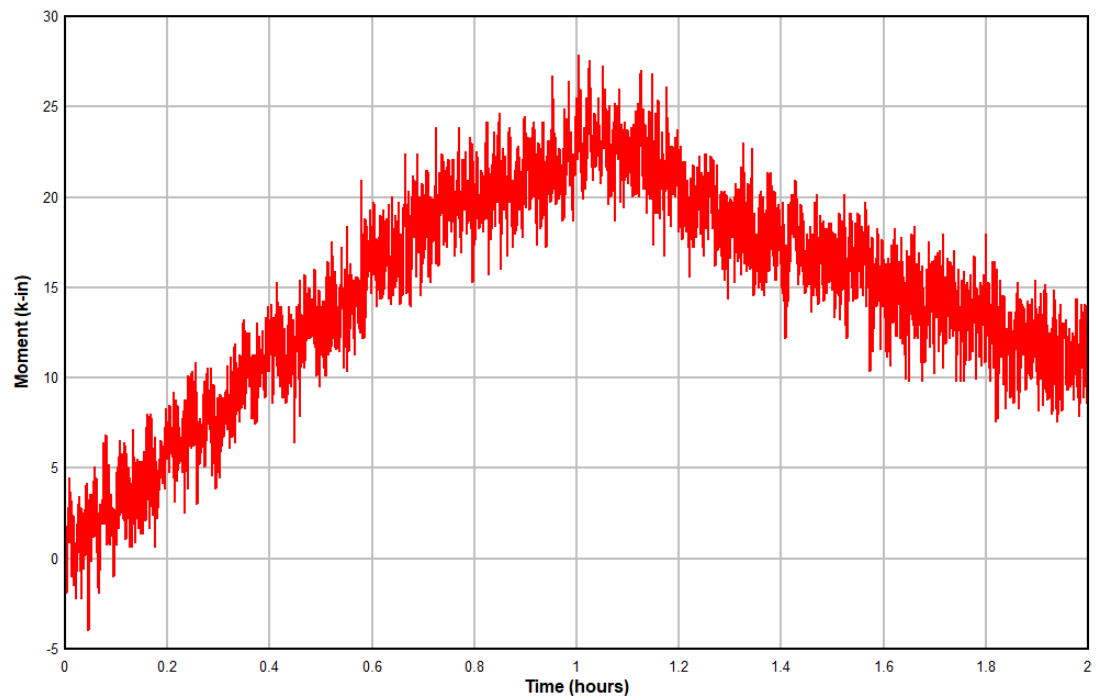


Figure 68: Midpoint Moment vs Time (Simulated 1-hr Rain Event Test)

Figure 69 and Figure 70 display moment vs downslope parapet wall water elevation for the two flooding input and uniform input ponding tests respectively. The relationship between moment and water elevation echoes the relationship between displacement and water elevation, and stress/strain and water elevation.

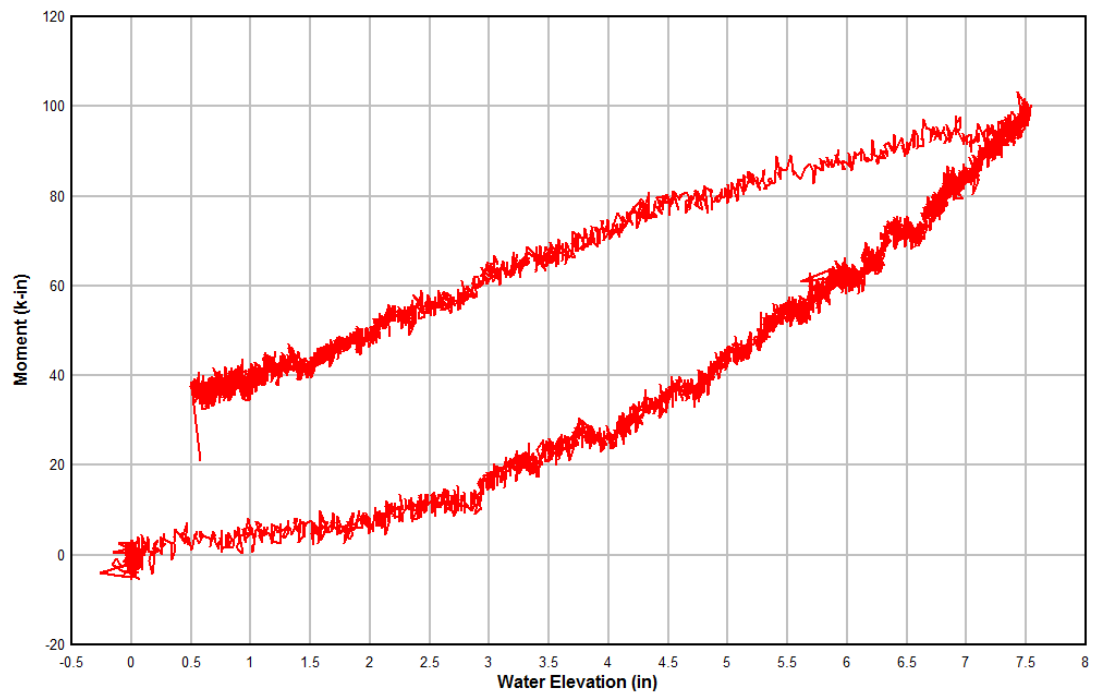


Figure 69: Midpoint Moment vs Downslope Parapet Wall Water Elevation (Ponding Flooding Input Test)

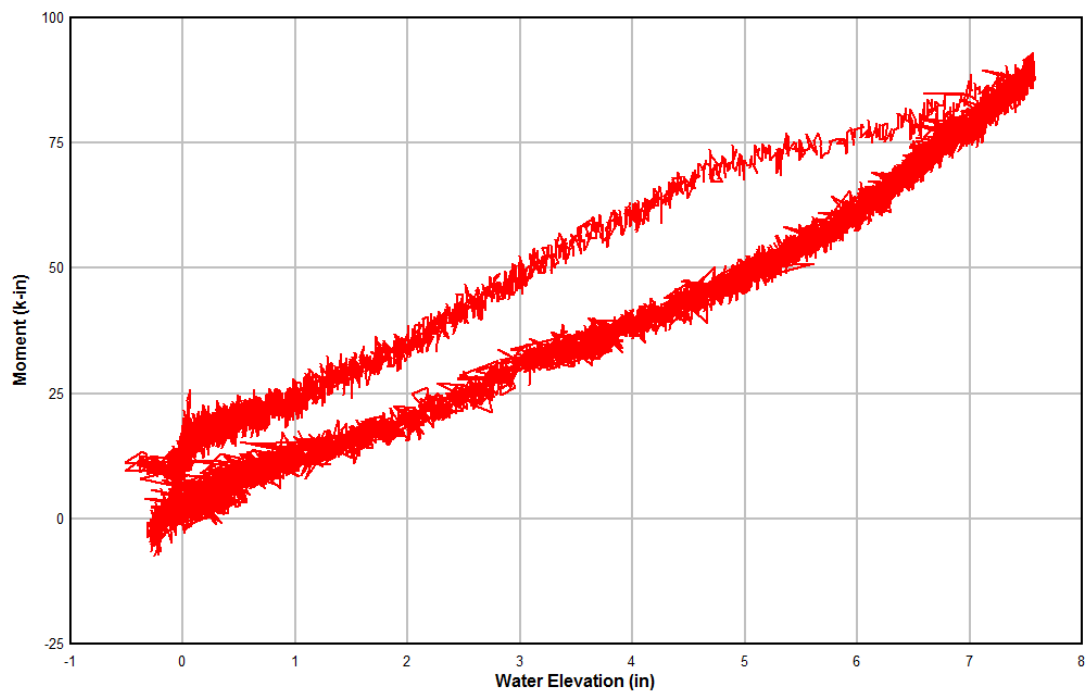


Figure 70: Midpoint Moment vs Downslope Parapet Wall Water Elevation (Ponding Uniform Input Test)

#### 4.5-Downslope End Rotation

Characteristic downslope end rotation for ponding tests is shown below in Figure 71, which displays the end rotation associated with the flooding input ponding test. Rotation begins with a value of approximately zero, increasing throughout the testing interval until a maximum value of approximately 0.072 degrees occurs. After the maximum value is reached, end rotation decreases as the roof drains beginning to plateau at 0.045 degrees. Measured end rotation was less than theoretical end rotation 0.105 degrees, indicating that connections were semi-rigid instead of pinned, as designed.

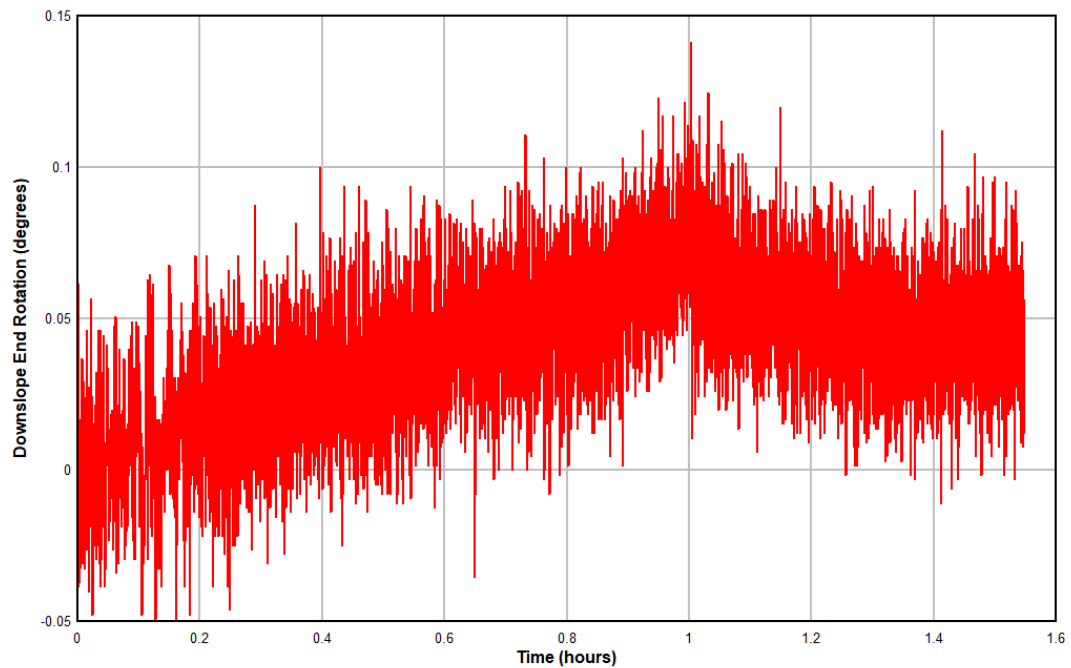


Figure 71: Downslope End Rotation vs Time (Ponding Flooding Input Test)

#### 4.6-Ecoroof Load

##### 4.6.1-Soil Density

Soil density as measured during the soil moisture modification process, and the unit weight psf values corresponding to a 4 inch layer of the soil are displayed in Table 4 below:

Table 4: Ecoroof Soil Unit Weights

Soil State	Density (lb/ft <sup>3</sup> )	Unit Weight (psf)
Dry	31.8	10.6
Saturated	62.6	20.9

As can be seen, the weight of the ecoroof soil nearly doubles when progressing from an entirely dry to saturated state.

#### 4.6.2-Roof Weight as a Whole

Ecoroof unit weights as a whole, including all layers that can hold moisture are contained in Table 5 below:

Table 5: Ecoroof Unit Weights

Ecoroof State	Density (lb/ft <sup>3</sup> )	Unit Weight (psf)
In Situ	34.1	13.5 psf
Saturated	60.6	24 psf

### 4.7-Moment Amplification (Beta)

#### 4.7.1-Beam Calibration Results

Results from the beam calibration test were used to determine the tributary width associated with the center beam. As shown in Figure 72 below, the center beam held 77.9% of the total load that the roof was under. Since the total width of the roof specimen was 10'11-5/8", or 131 inches, the tributary width associated with the center beam was determined as 102.5". This tributary width was later used while calculating the beta value associated with the experimental ecoroof.



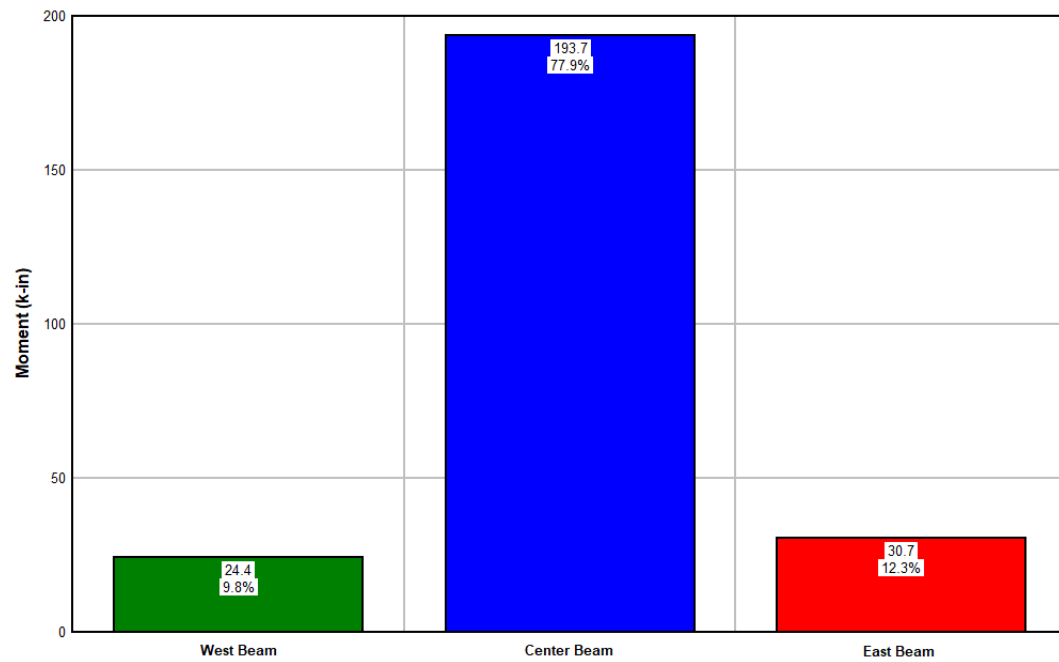
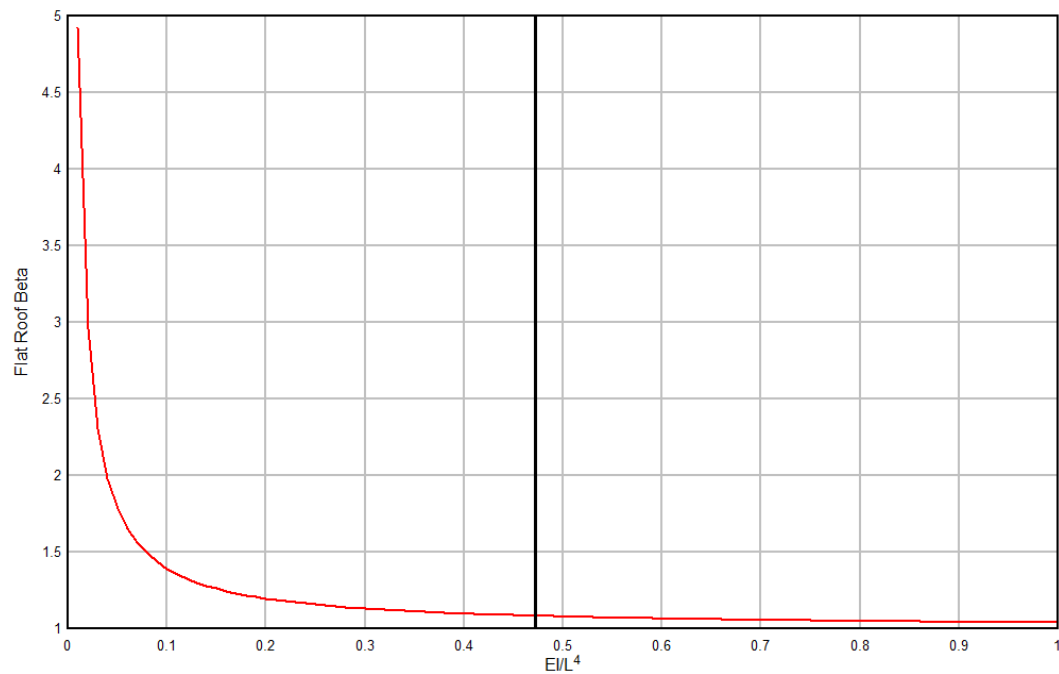


Figure 72: Calibration Load Moment Distribution

#### 4.7.2-Flat Roof Beta

Figure 73: Flat Roof Beta vs  $EI/L^4$ .

As noted in equation 3.38, Beta also relies on  $\gamma_w$ , the specific gravity of water, and  $t_w$ , the tributary width associated with the beam in question. For Figure 73, both of these values were set to 0.0361 lb/in<sup>3</sup> and 102.5 inches respectively, due to those values corresponding with the tests completed and the roof conditions. The beta value, were the tested roof to be flat, was calculated as  $\beta=1.0825$ , meaning that a flat roof with the properties associated with the tested roof would experience a total moment 8.25% greater than the calculated first-order moment, due to second-order effects.

#### 4.7.3-Sloped Roof Beta

Figure 74 compares beta vs  $EI/L^4$  for flat roofs, and beta for roofs with a slope of 0.25/12 with dead loads of 24 psf and 100 psf. As can be seen from the figure, there is no apparent difference between beta values for flat roofs and beta values for roofs with a slope of 0.25/12, even when dead loads vary.

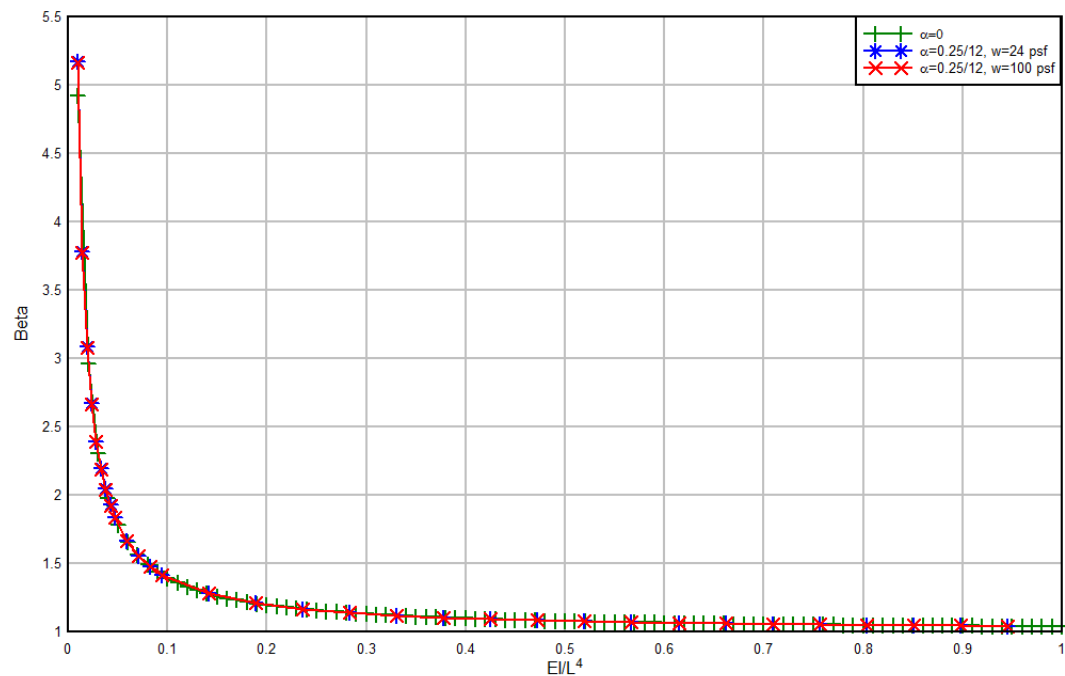


Figure 74: Beta vs  $EI/L^4$  for flat roof and roof with a slope of 0.25/12, with varying dead loads.

Although dead load has little effect when viewed in the context of  $\beta$  vs  $EI/L^4$ , when  $\beta$  vs secondary drain height is plotted, dead load's effect can be better observed. Figure 75, seen below, displays  $\beta$  vs height of secondary drains, for a constant roof slope of 0.25/12 and varying dead loads. The black reference line indicates the flat roof  $\beta$  value associated with the  $EI/L^4$  value of the sloped roofs. As secondary drain height increases,  $\beta$  values converge towards the flat roof  $\beta$  value. As dead load increases,  $\beta$  has a correspondingly larger value at similar secondary drain heights. Despite this pattern, sloped roof  $\beta$  values tend to converge with flat roof  $\beta$  values at the same secondary drain height. This indicates that while dead load has an effect on  $\beta$  values, it is not a controlling design factor.

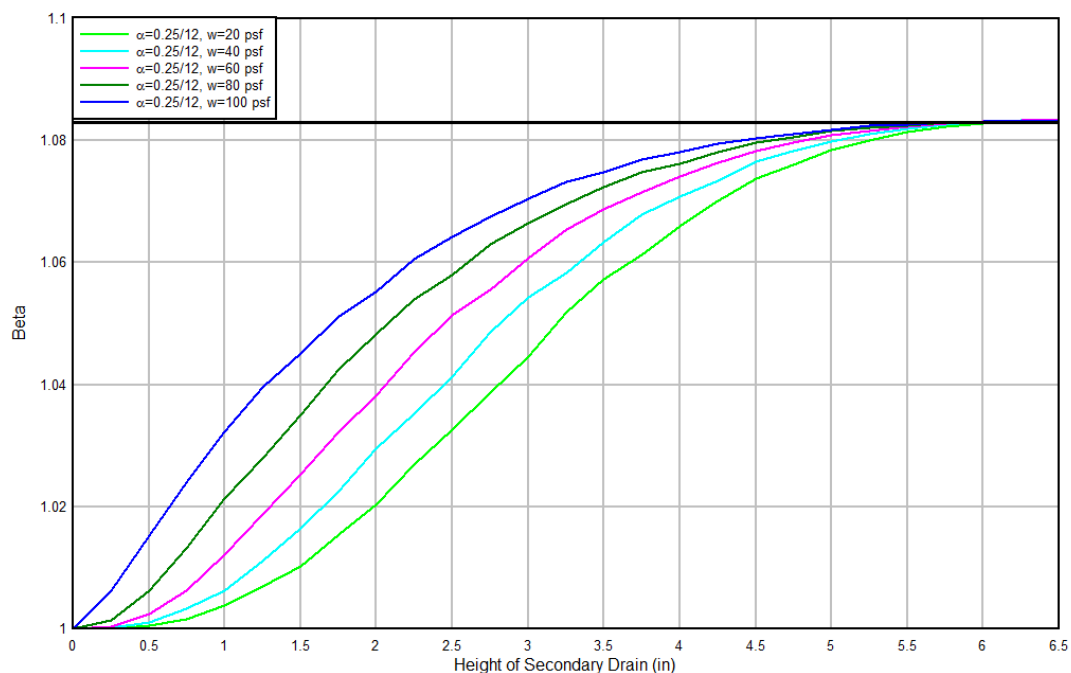


Figure 75: Beta vs Secondary Drain Height for Roofs with Slope 0.25/12 and Varying Dead Loads

Dead load's effect on partially loaded spans is further investigated in Figure 76 and Figure 77, which display the deflected shapes for roof with a slope of 0.25/12, and dead loads of 20 or 100 psf, and secondary drain heights of 1 inch or 5 inches respectively. Secondary drain heights are indicated by the horizontal black reference lines. As can be seen in Figure 76, the proportional difference between the areas water can occupy for the two deflected shapes is larger than in Figure 77, where secondary drain height is 5 inches. Consequently, there is a larger difference in the beta values associated with a secondary drain height of 1 inch than those associated with a secondary drain height of 5 inches.

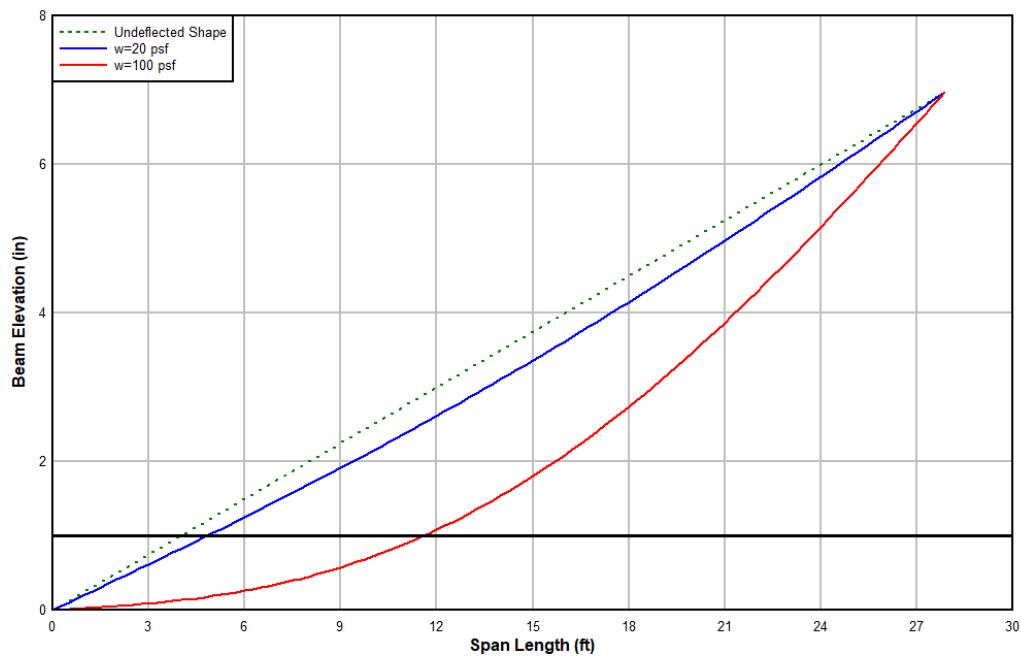


Figure 76: Deflected Shapes for a Roof with a 0.25/12 Slope, 20 and 100 psf Dead Loads, with Secondary Drain Height of 1 inch.

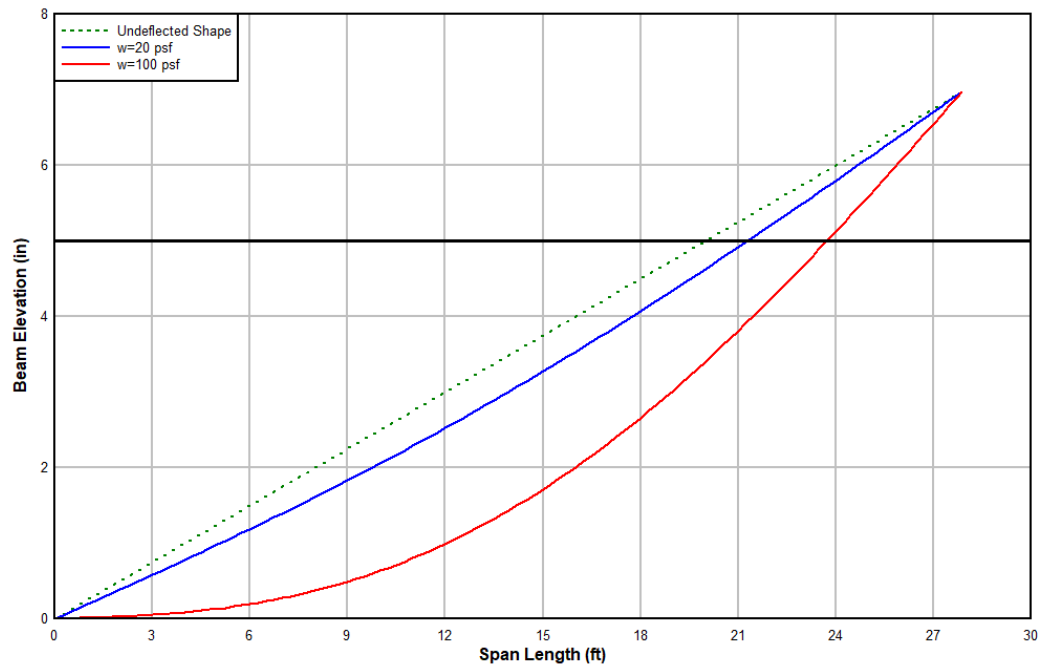


Figure 77: Deflected Shapes for a Roof with a 0.25/12 Slope, 20 and 100 psf Dead Loads, with Secondary Drain Height of 5 inches

The effect of varying roof slopes on beta can be seen in Figure 78 below, which plots flat roof beta vs  $EI/L^4$ , in addition to the beta values associated with roofs with a slope of 0.25/12 and 1/12, with a dead load of 100 psf. A 100 psf dead load was selected for comparison, as it was significantly larger than the 24 psf dead load that corresponded to a totally saturated ecoroof, which caused little deviation from flat roof beta values. As with Figure 74, there is little observable difference between flat roof beta values and those with a slope of 0.25/12. However, when roof slope increases to 1/12, beta values noticeably decrease in comparison to flat roof beta values beginning at an  $EI/L^4$  value of approximately 0.04, as seen in Figure 79.

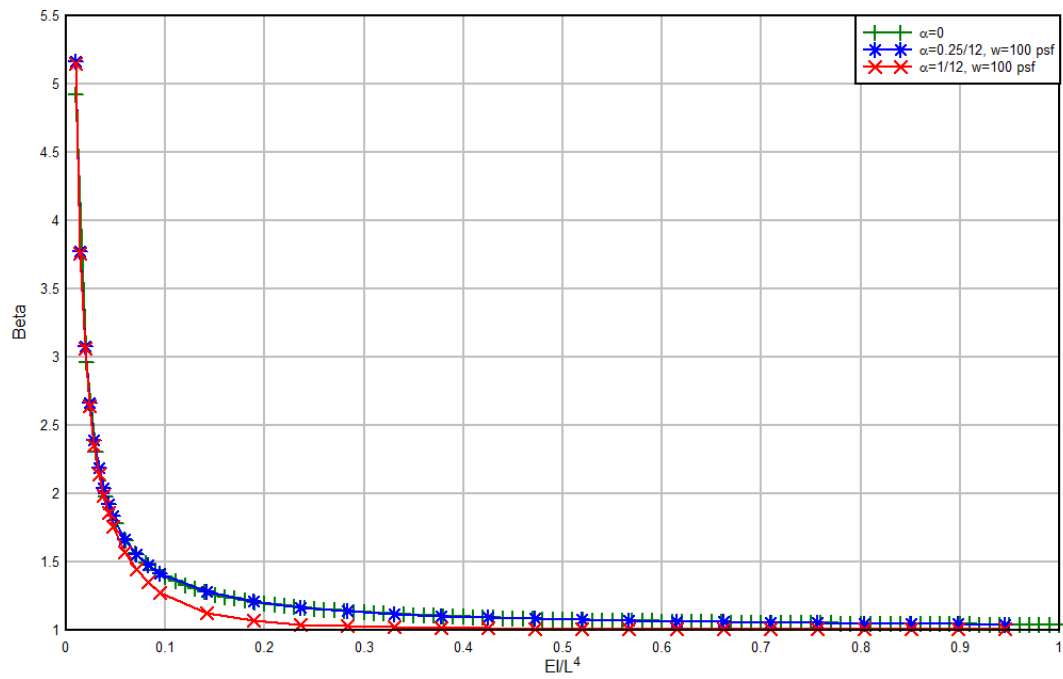


Figure 78: Beta vs  $EI/L^4$  for Flat Roof and Roofs with 100 psf Dead Load and Varying Slope

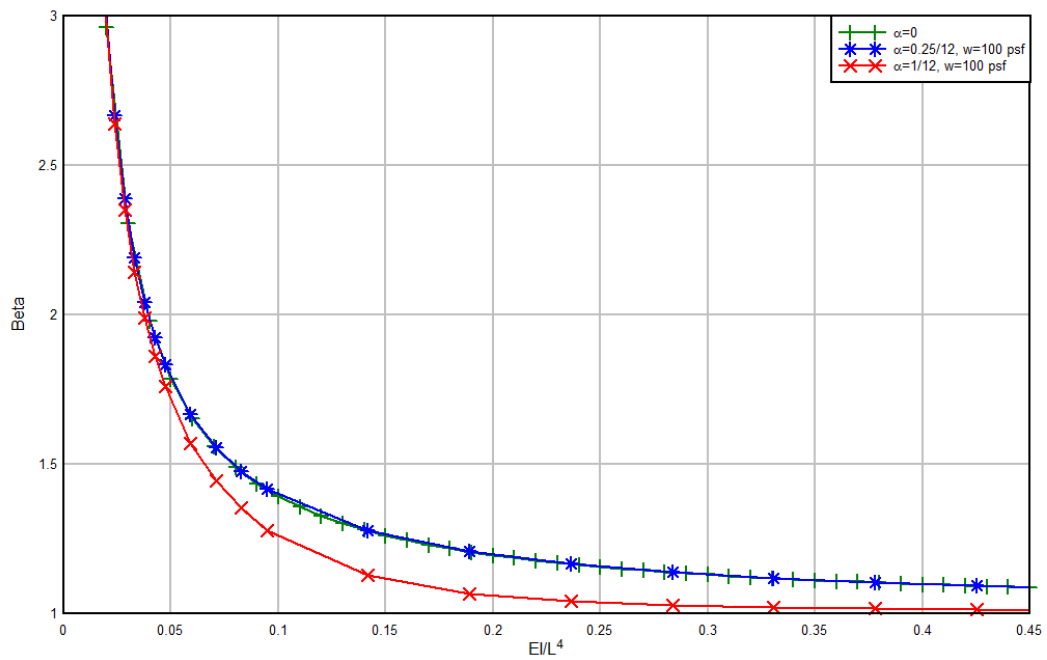


Figure 79: Expanded View of Bottom-Left Corner of Figure 78

The effect of roof slope on beta values is more closely explored in Figure 80, which displays beta vs secondary drain height, for varying roof slopes, with a constant dead load of 30 psf among all roofs. As with Figure 75, the black reference line denotes the flat roof beta value associated with the  $EI/L^4$  value that is common among all roofs. As secondary drain height increases, beta values converge towards the flat roof beta value. Convergence occurs at a rate that is inverse to the roof slope.

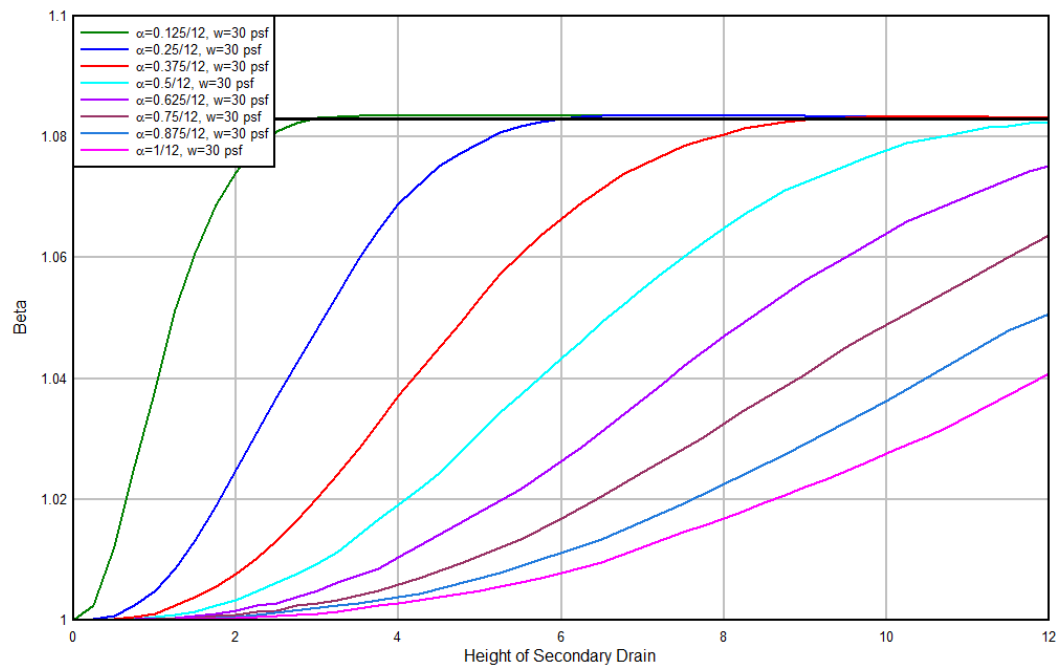


Figure 80: Beta vs Secondary Drain Height for Roofs with 30 psf Dead Load and Varying Roof Slopes

#### 4.7.4-Experimental Beta

The experimental beta value was calculated for the uniform input ponding test, and was found to be 1.032. Theoretical beta for the test set up was 1.035, and percent difference between the two was 0.23%. It should be noted that while this experimental beta aligned well with expectations, further comparisons are needed to ensure the validity of beta.

## Chapter 5 – Summary of Results and Conclusions

### 5.1-Summary of Work Done

As ecoroofs become more widespread throughout the United States, it becomes more important that an understanding of their structural behavior be developed and codified, in order to ensure that designs featuring them are efficient and safe. Over the course of this research, which builds on the research done by Travis Kraupa (2014) and Kim Kilroy (2015), a full scale ecoroof specimen and a one-dimensional shake table capable of subjecting the ecoroof to lateral motions was constructed. Four tests and one calibration were conducted, examining the drainage behavior of the roof and the structural effects of that behavior. Two tests examined behavior under small ponding loads, and two tests investigated the roof's behavior when subject to free-draining rain events. A hydraulically loaded roof model was then used to investigate second-order effects associated with impounded water, and a moment amplification factor to account for second-order effects was developed.

### 5.2-Experimental Conclusions

- Structural effects, such as moments and stress, that result from a rain event, up to and including a 1-hr event with a 60 year return period, and act on a free-draining extensive ecoroof, are of a small, generally negligible magnitude.
- Residual displacements that are imposed on a free-draining extensive ecoroof after a rain event up to and including a 1-hr event with a 60 year return period, are of a small enough magnitude such that any second-order effects are negligible.
- A standard extensive ecoroof does not saturate during an event with a 60 minute duration and 100 year return interval, if it possesses a typical water content before the event begins.
- Ecoroofs are able to reach steady state flow at a variety of flow rates.



- How the roof is loaded can affect the magnitude of the force effects it is subject to. Despite the maximum downslope parapet wall water elevation for the uniform input test being larger than that for the flooding input test, the flooding input test created larger force effects (displacements, moments, ect) despite an ostensibly smaller load acting on the roof.
- Downslope maximum support displacements were between 26% and 33% of the maximum displacement at the midpoint, while maximum upslope displacements were between 16% and 23% of the maximum midpoint displacement.
- The unit weight of the extensive ecoroof nearly doubled when it saturated, with an initial psf of 34.1 and a saturated psf of 60.6

### 5.3-Analytical Conclusions

Note: All discussion of moment amplification due to second-order effects only considers one iteration of second-order effects due to hydraulic loading.

- Flat roof moment amplification due to second-order effects is independent of dead and rain load, and is governed by modulus of elasticity ( $E$ ), moment of inertia ( $I$ ), span length ( $L$ ), tributary width, ( $t_w$ ), and the specific gravity of the fluid that is occupying the roof ( $\gamma_w$ ).
- There is little difference between moment amplification due to second order effects for flat roof with identical structural properties ( $E$ ,  $I$ ) and geometry (span length, tributary width) as a roof with a slope of 0.25/12.
- Moment amplification factor due to second order effects for a roof with identical  $E$ ,  $I$ , span length, and tributary width as a flat roof will converge towards the flat roof's moment amplification factor as the height of water impounded on the roof (or secondary drain height) increases.

- As water is able to occupy more of the span of a sloped roof, the second-order moment amplification response of the roof increasingly resembles the second-order moment amplification response of a flat roof.
- Increasing slope more effectively mitigates second-order effects than decreasing dead load.
- Span length is the most important characteristic to consider when addressing moment amplification due to second-order effects.

#### 5.4-Design Recommendations

- Adapt the definition of Transient Water Live Load provided by ASTM 2397 to include the water required to saturate ecoroof planting material from a drained state, instead of restricting Transient Water Live Load to the amount of water that can saturate the drainage layer.
- When calculating rain load, the exposed surface of the ecoroof planting medium should be identified as the datum, in order to successfully use 8.3-1 from ASCE 7-10.
- If the rain datum is selected as the ecoroof surface, when considering rain load, the transient water live load should be taken into consideration as well, since both loads will occur simultaneously.
- Should other live loads be considered outside of transient water live load, it may be helpful to separate it into a different load category within loading combinations, due to its characteristic occurrence alongside rain loads.

### 5.5-Proposed Future Research

1. Use constructed shake table to conduct full-scale shake table tests to investigate the structural responses of an ecoroof to lateral loading, as would be experienced during a seismic event.
2. Create a database containing information regarding the cause of ecoroof failures, in order to aide in the identification of other areas of risk that should be accounted for when created a structural specification for the design of ecoroofs.
3. Conduct similar drainage tests on intensive ecoroof specimans. Due to the increased depth of planting media, transient water loads have the potential to be much larger than on extensive ecoroofs.
4. Investigate the relationship between snow load and Transient Water Live Load, to determine if Transient Water Live Load should also be considered concurrently with snow load.
5. Repeat the tests from this project with a more reliable temperature correction mechanism to develop a better understanding of longer term ecoroof drainage behavior.
6. Compare the dead load determination according to ASTM E2397 to in-situ ecoroof dead load, to access accuracy of the ASTM process, and evaluate its use as a foundation for the portion of the ecoroof structural specification concerning dead loads.

## References

- ASCE. (2013). *ASCE/SEI 7-10: Minimum Design Loads for Buildings and Other Structures*. Reston, VA: American Society of Civil Engineers.
- ASTM International. (2015). *E2397/E2397M-15: Standard Practice for Determination of Dead and Live Loads Associated with Vegetative (Green) Roof Systems*. West Conshohocken, PA: ASTM International.
- ASTM International. (2015). *E2398/E2398M-15a: Standard Test Method for Water Capture and Media Retention of Geocomposite Drain Layers for Vegetative (Green) Roof Systems*. ASTM.
- ASTM International. (2015). *E2399/2399M-15: Standard Test Method for Maximum Density for Dead Load Analysis of Vegetative (Green) Roof Systems*. West Conshohocken, PA: ASTM International.
- Cheung, G. (2016, June 10). Hong Kong City University green roof collapse contractor faces possible lawsuit. *South China Morning Post*.
- Columbia Green Technologies. (2012). *Green Roof Systems*. Retrieved from Columbia Green Technologies: <http://columbia-green.com/systems/>
- Environmental Services*. (2017, November 12). Retrieved from The City of Portland Oregon: <https://www.portlandoregon.gov/bes/article/547491>
- EPA. (2017, April 25). *Reducing Urban Heat Islands: Compendium of Strategies - Green Roofs*. Retrieved from EPA Web site: <https://www.epa.gov/sites/production/files/2014-06/documents/greenroofscompendium.pdf>
- Fountain, H. (2011, February 18). Green Roof Collapses in Illinois. *The New York Times*.
- Getter, K. L., & Rowe, D. B. (2006). The Role of Extensive Green Roofs in Sustainable Development. *HortScience*, 1275-1285.
- Hutchinson, D., Abrams, P., Retzlaff, R., & Liptan, T. (2003). Stormwater monitoring two ecoroofs in Portland, OR, USA. *Greening Rooftops for Sustainable Communities: Chicago 2003*, (pp. 1-18). Chicago.
- International Code Council. (2014). *2014 Oregon Structural Specialty Code*. Country Club Hills, IL.
- International Code Council. (2017). *2017 Oregon Plumbing Specialty Code*. Country Club Hills, IL.
- Jorg Breuning & Green Roof Service, LLC. (2017). *Green Roof Technology: Form & Function*. Retrieved from [greenrooftechnology.com](http://greenrooftechnology.com)

- Kilroy, K. (2015). *Direct Shear Interface Friction and Linear Motion Shaking Response of Ecoroofs*. Corvallis: Oregon State University.
- Kraupa, T. J., Stuedlein, A. W., Mason, H. B., & Higgins, C. C. (2016). Engineered Ecoroof Systems: Geotechnical Considerations. *Journal of Infrastructure Systems*.
- Li, D., Bou-Zeld, E., & Oppenheimer, M. (2014). The effectiveness of cool and green roofs as urban heat island mitigation strategies. *Environ*, 1-16.
- MacMullan, E., Reich, S., Puttman, T., & Rodgers, K. (2008). Cost-Benefit Evaluation of Ecoroofs. *Low Impact Development for Urban Ecosystem and Habitat Protection*. Seattle: ASCE.
- Magill, J. D., Midden, K., Groninger, J., & Therrell, M. (2011). *A History and Definition of Green Roof Technology with Recommendations for Future Research*. Paper 91: Research Papers.
- USEPA. (2003). *Cooling summertime temperatures: Strategies to reduce urban heat islands*. Washington D.C.: USEPA.
- USEPA. (2017, June 20). *Heat Island Effect*. Retrieved from United States Environmental Protection Agency: <https://www.epa.gov/heat-islands>
- Walberg, M. (2011, February 14). Grass-covered 'green roof' collapses in St. Charles. *The Chicago Tribune*.
- Weiler, S. K., & Scholz-Barth, K. (2009). *Green Roof Systems: A Guide to the Planning, Design, and Construction of Landscapes over Structure*. Hoboken: John Wiley & Sons, Inc.
- Welsh-Huggins, S. J., & Liel, A. B. (2016). A life-cycle framework for integrating green building and hazard-resistant design: examining the seismic impacts of buildings with green roofs. *Structure and Infrastructure Engineering*, 19-33.
- Yang, J., Yu, Q., & Gong, P. (2008). Quantifying air pollution removal by green roofs in Chicago. *Atmospheric Environment*, 7266-7273.

## Appendix A – Shake Table Construction

### Shake Table Frame

For this research, a large one-dimensional shake table was constructed on a 10 in thick concrete pad on the west side of the O.H. Hinsdale Wave Research Laboratory Building at OSU. The table was designed to bring a structure of dimensions approximately 30' x 12' through a 4 ft. range of motion. Two 40 foot W40x324 sections comprised the frame of the table running in the N-S direction. Two W21x111 beams were used as cross beams in the frame. Both beams were 11'-9-7/8" long, with plates that were 9/16" thick welded to each end. Each plate had twelve 1-1/8" diameter holes, which aligned with pre-existing holes in the webs of both W40x324s. The cross beams were bolted through 12 holes on each side, and were spaced 24 feet apart on center. One of the cross beam connections can be seen in Figure A 1 below.



Figure A 1: Northwestern connection between W40x324 and W21x111 crossbeam.



Following the establishment of the frame, the two W40x384 beams were separated by a distance of 12 ft on center.

#### Anchoring Shake Table

After completion of the shake table frame, eight 7/8" steel anchors were placed through the bottom flange of each W40x324 beam. Anchors were placed in groups of four, with each group centered two feet from one of the beam ends. Anchors were designed to work in combination to resist a load of 100 kips that will be exerted by the actuator. Calculations pertaining to anchor design strength can be found in Appendix E. Every group was an 8"x8" square, symmetric about the W40x324 centerline, with an anchor at every corner, as seen below in Figure A 2. Each anchor extended to an 8" depth in the concrete pad.



Figure A 2: Shake Table Anchor Formation



Before the anchors were epoxied, the shake table frame was surveyed, using a Nikon laser total station. Four locations were surveyed, each corresponding to the centerline of the linear motion rails that the shake table would move along. Based on the measured elevations, washers were placed on each group of anchors, between the concrete and the bottom of the W40x324 bottom flange, to shim the beams and create a level surface. Once a level surface was realized, a form was constructed for the west W40x324, and was filled with a high-slump concrete slurry, to create a concrete bearing pad. The eastern W40x324 did not require significant elevation, so a concrete bearing pad was unnecessary. Instead, a hydrostone pad was constructed around the group of anchors in the beam's southern end. After the concrete had set, anchor holes were cleaned and the anchors were epoxied into them using a concrete epoxy adhesive.

#### Shake Table Mechanism

Following the completion of the anchoring system, construction began on the shake table itself. The shake table would move N-S on a THK Linear Motion rail and bearing system. Each rail was 4 feet in length and attached to a steel plate of dimensions 48"x12"x1 1/2". Linear motion rails were not attached directly to the W40x324 beams because it was easier to machine the holes needed to attach the rails in the smaller plates. Two plates and rails were bolted to each W40x324 beam, parallel with the direction of the beam, as displayed in

**Error! Reference source not found..**



Figure A 3: Linear Motion Rail on Top of and in Parallel with W40x324 Shake Table Framing Beam.

A distance of 30' separated the linear motion rail centerpoints in the N-S direction, as shown in the Figure A 4 below.

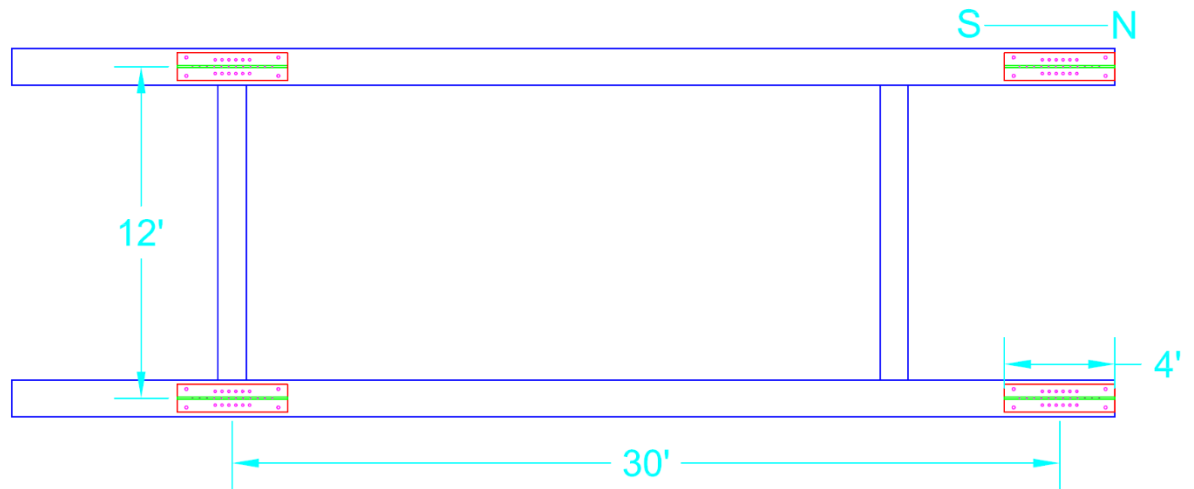


Figure A 4: Linear Motion Rail Layout

On top of each rail rode a THK SHS 25C bearing, and on top of each bearing a bearing plate was attached. Figure A 5 contains the bearing with attached bearing plate on the linear motion rail.



Figure A 5: Linear Motion Bearing Mounted on Linear Motion Rail

#### Shake Table Primary Members

The primary members of the shake table were two W 12x106s that ran N-S and two W21x111s that ran E-W. Both the W12x106s were 31'-9" long, with 22" copes through half of the flange on each end. Additionally, twelve 1-1/16" holes were cut through the web on each end of both beams, at the location of the cope, as can be seen in the **Error! Reference source not found.** below.

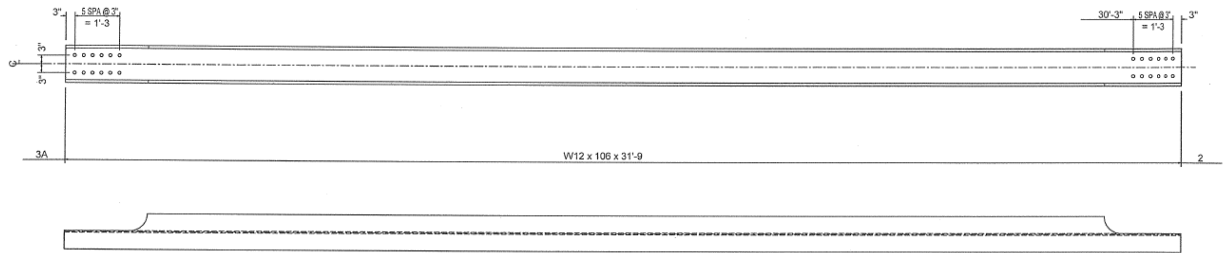


Figure A 6: W12x106 Drawings, Displaying Cope and Hole Arrangement (Drawing Courtesy of Fought and Company)

Each W12x106 rested on its flanges in the N-S direction and was supported by two of the bearing plates, as can be seen in Figure A 7 below.





Figure A 7: Northern End Bearing Plate Supporting One End of a W12x106 Beam

According to ASCE 7-10 (ASCE, 2013), the minimum acceptable roof slope necessary to preclude considering ponding instability during structural design, assuming free drainage, is  $\frac{1}{4}$ " elevation per foot of length. In order to create this slope, 4 steel plates varying in thickness between 1.5 and 2 inches, with a hole pattern identical to that drilled through the webs of the W12x109 members, were placed on the northern coped ends of each beam, such that the holes aligned.

Both W21x111s were 13'9" long. Like the W12x106 section, the two W21x111s were also coped through half the flange on each end, and had twelve 1-1/16" holes cut through the web at each coped location. On the downslope end, a W21x111 was set on top of the W12x106 columns, coped side down, so that the webs of the two beams were in contact, and bolted together. The remaining W21x111 was set atop the aforementioned plates, and secured with lengths of threaded rod. Figure A 8 below shows the downslope connection, while Figure A 9 shows the upslope connection.



Figure A 8: Downslope Connection Between W12x106 and W21x111



Figure A 9: Upslope Connection between W12x106 and W21x111, with Stacking Plates to Create Roof Slope

#### Actualizing the Actuator

Following the completion of the roof structure, a 100 kip actuator was attached to drive the motion of the table. The actuator was attached to the downslope W21x111 and was anchored by a W14x284. The W14x284 was set parallel to the downslope W21x111, with each end of the downward flange resting on a stack of three plates. These three plates served to elevate the W14x284, so that when installed, the actuator could be attached to the center of the W21x111 beam. Additionally, one plate was used as a washer on each end of the upper flange. All plates, both ends of the upper and lower flanges of the W14x284, and the upper flanges of the W40x324 had a square pattern of four 1-5/16" diameter holes drilled, with the holes spaced 8 inches apart. A nut was attached to 1-1/4" threaded rod,



which was then passed through the upper plate washer, upper and lower flanges of the W14x284, the stack of three elevating plates, and the upper flange of the W40x384, following which, a nut and washer were fastened to the lower end of the rod. The set up can be seen in Figure A 10 below.



Figure A 10: Actuator Beam Set-up and Connection

Once the W14x284 was anchored, a large hole was cut in the beam web so that the actuator piston could attach to the downslope W21x111 crossbeam. A square four bolt pattern was used to attach the actuator to both the W14x284 web and W21x111 flange. The connection

between piston and shake table cross beam can be seen below in **Error! Reference source not found.**



Figure A 11: Bolted Connection between Actuator Piston and Shake Table Cross-Beam

## Appendix B – ASTM E2397 In-Depth Explanation and Procedure

### Dead and Live Load Definitions

As mentioned in Chapter 2, ASTM E2397 (ASTM International, 2015), defines dead load associated with an ecoroof as “weight under drained conditions after new water additions by rainfall or irrigation as ceased (this includes the weight of retained and captured water” and defines the live load associated with an ecoroof as “weight when rainfall or irrigation is actively occurring and the drain layer is completely filled with water. **The difference in weight between the first and second conditions, approximated by the weight of transient water in the drain layer, is considered a live load.**” Table A 1, shown below, indicates the loads associated with different ecoroof components, and provides instructions on how to calculate the loads, in accordance with the applicable ASTM standards. Unless otherwise indicated, processes are from ASTM E2397 (ASTM International, 2015).

Table A 1: Ecoroof Dead and Live Load Component Calculations According to ASTM E2397

Component	Dead Load			Live Load
	Component Weight (psf)	Retained Water (psf)	Captured Water (psf)	Transient Water (psf)
Non-absorptive sheet	Weigh dry 4 in x 4 in section. Multiply weight by 9 to convert to psf.	N/A	N/A	N/A
Fabrics	Weigh dry 4 in x 4in piece of fabric. Multiply weight by 9	Immerse sample in water for 15 minutes, and drain over #30	N/A	N/A

	to convert to psf.	sieve for 15 minutes. After draining, weigh. Subtract initial sample weight, and multiply by 9 to convert to psf.		
Growth Media (granular)	Unit weight: Maximum Media Density (MMD), calculated according to ASTM E 2399 (ASTM International, 2015) multiplied by the thickness of the media layer in feet.		N/A	N/A
Drain Layer (absorptive mat)	Weigh dry 4 in x 4in piece of mat, and multiply by 9 to convert to psf.	Immerse sample in water for 24 hrs. Allow mat to drain for 2 hours over #30 sieve. Weigh mat, then subtract initial weight, and multiply by 9 to convert to psf.	N/A	Immerse sample in water for 24 hours and weigh immediately. Subtract sample weight after it has been allowed to drain to for 2 hours, and multiply by 9 to convert to psf.
Drain Layer (granular)	Unit weight: MMD, calculated according to ASTM E2399 (ASTM International, 2015)		N/A	Determine Air-Filled Porosity (AFP)

	multiplied by the thickness of the media layer in feet.			according to ASTM E2399 (ASTM International, 2015). Restrict drainage to impound water in drain layer. Multiply AFP by the average height of impounded water in the drainage layer.
Drain Layer (geocomposite)	Weigh dry 6 in x 6 in section. Convert to psf.	N/A	Multiply the unit water capture volume, $R_w$ , determined according to ASTM E2398 (ASTM International, 2015) by 62.4 lbs/ft <sup>3</sup> .	Multiply drain layer thickness by 62.4 lbs/ft <sup>3</sup> and subtract the weight of captured water.
Drain Layer (granular/geocomposite hybrid)	Add the Unit Media Retention Volume, $R_m$ , determined according to ASTM E2398 (ASTM International, 2015) to the thickness of the granular media to determine the Effective Thickness, ET. Multiply ET by the MMD, determined according to ASTM E2399 (ASTM International, 2015).		Multiply $R_w$ , determined according to ASTM E2398 (ASTM International, 2015) by 62.4 lbs/ft <sup>3</sup> .	Determined AFP according to ASTM E2399 (ASTM International, 2015). Multiply by ET. Add geocomposite drain layer thickness and granular layer thickness to this quantity. Subtract ET, and multiply by 62.4

			Subtract weight of captured water.
--	--	--	------------------------------------

It should be noted that ASTM E2397 (ASTM International, 2015) also includes a process to calculate dry density of granular materials during dead load determination. Dry density not mentioned in the above table because dead load due to dry granular materials will be less conservative than the dead load due to water immersed and drained granular materials.

#### ASTM E2399/E2399-15 Calculation Summarization

**Dry Density Calculation:** Place a sieve disk in a cylinder and weigh. Fill cylinder with material, and deal 6 blows with a Proctor hammer. Measure compacted sample's initial height and calculate initial volume. Weigh the cylinder and sample, and subtract the weight of the cylinder to determine initial sample weight. Dry density is the initial sample weight divided by the initial volume. Convert to lbs/ft<sup>3</sup> (ASTM International, 2015).

**Maximum Media Density (MMD) Calculation:** After dry density calculation has been completed, immerse cylinder and sample in a water bath with water of 68°F for 24 hrs. Once this period of time has passed, remove the cylinder from the water, and allow it to drain for 2 hrs. Weigh the cylinder and sample, and subtract the cylinder's weight to determine the sample weight. Measure the final sample thickness. Calculate MMD by dividing the sample weight by the initial sample volume, determined during the dry density calculation (ASTM International, 2015).

**Maximum Media Water Retention (MMWR):** MMWR is the difference between MMD and Dry Density, expressed as a percentage of water density. It is calculated using the following formula:

$$MMWR = 100 * \frac{(MMD - D_{dry})}{62.4} \quad (B.1)$$

Where MMD is Maximum Media Density (lb/ft<sup>3</sup>),  $D_{dry}$  is Dry Density (lb/ft<sup>3</sup>), and 62.4 lbs/ft<sup>3</sup> is the unit weight of water (ASTM International, 2015).

Air-Filled Porosity (AFP): AFP is calculated using the following formula:

$$AFP = TP - MMWR \quad (B.2)$$

where TP is the total porosity, as a volume percent, and MMWR is the Maximum Media Water Retention, or moisture content at Maximum Media Density, also as a volume percent (ASTM International, 2015).

#### Note on Retained Water

According to the ASTM standard, retained water for growth media is calculated by multiplying MMWR by the thickness of the media layer. However, because MMWR is the moisture content present at MMD, then when the unit weight of granular material is calculated by multiplying MMD by the thickness of the granular layer, it includes the weight of retained water. This is why the “component weight” and “retained water” columns are merged for granular materials in **Error! Reference source not found.**

#### Note on Granular Drain Layer Live Loads

Live load for granular drain layers is determined by calculating the available pore space when the material is assumed to be at a natural state of saturation associated with the MMD, and multiplying the available pore space by the average height of water in the drain layer when the drain is restricted. It seems that it would be more conservative to assume that the drain layer would be entirely saturated, with the average height of impounded water equaling the layer thickness.

#### ASTM E2398/E2398M-15a Calculation Summarization

Unit Water Capture Volume,  $R_w$ , Calculation: Procure a sample of the geocomposite drain layer that is at least 6 in by 6 in. Weigh sample. Fill receptacles in sample with water.

Weigh sample again. Measure the distance between the center of adjacent receptacles, both along the length and width of the sample. Repeat the test, inclining the sample to the same degree that the intended ecoroof will possess.  $Rw$ , is calculated using the following formula:

$$Rw = \frac{2.31 * Ww}{N * X * Y} \quad (B. 3)$$

where  $Ww$  is the difference between the dry weight of the sample, and the weight of the sample when it is filled with water.  $N$  is the number of receptacles on the sample,  $X$  is distance between center of receptacles along the sample width,  $Y$  is the distance between center of receptacles along the sample length, and  $Rw$  is in units of  $\text{ft}^3/\text{ft}^2$ . The factor of 2.31 is the product of the conversion factor of  $144 \text{ in}^2/\text{ft}^2$ , divided by the unit weight of water,  $62.4 \text{ lb}/\text{ft}^3$ , which allows for the conversion from units of  $\text{lb}/\text{in}^2$  to  $\text{ft}^3/\text{ft}^2$  (ASTM International, 2015).

Unit Media Retention Volume,  $Rm$ , Calculation: First, create a barrier around the outside edges of the sample. Weigh the sample, and measure the inner dimensions that the barrier creates. Fill the geocomposite with sand until it is entirely and evenly covered. Weigh, and calculate the unit weight of the sand. Unit Media Retention Volume,  $Rm$ , is then calculated using the following formula:

$$Rm = 144 * \frac{Ws}{xy * \gamma} \quad (B. 4)$$

where  $Rm$  is the Unit Media Retention Volume in  $\text{ft}^3/\text{ft}^2$ ,  $Ws$  is the difference between the weight of the sample filled with sand and the weight of the sample when empty, in lbs,  $x$  is the width of the barrier, in inches,  $y$  is the length of the barrier, in inches, and  $\gamma$  is the unit weight of the sand in  $\text{lb}/\text{ft}^3$ . 144 is a factor to convert  $\text{ft}^3/\text{in}^2$  to  $\text{ft}^3/\text{ft}^2$ , with  $144 \text{ in}^2$  equaling  $1 \text{ ft}^2$  (ASTM International, 2015).



## Appendix C – Analysis and Discussion of Kim Kilroy’s Research

### Direct Shear Interface Friction Testing

During the preceding phase of this project, Kim Kilroy conducted a series of direct shear interface tests on the different interfaces of ecoroof components. These tests were conducted to determine whether it was more likely that shear failure occurs in ecoroof soil or among the other ecoroof components, and the accompanying friction angle and coefficient of friction. Shear failure is of interest, because should it occur, a large mass of soil could move, subjecting parapet walls and portions of the structural system to substantially increased loads. Tests were conducted in two conditions: while interface was dry, and while it was submerged by water, in order to mimic the expected conditions that an ecoroof would be exposed to. The following Table A 2 displays the results of the direct shear interface testing.

Table A 2: Direct Shear Interface Friction Testing Results for Dry and Submerged Ecoroof Components

Direct Shear Interface Friction Testing						
Material	Dry			Submerged		
	Interface Friction Angle (degrees)	Adhesion Intercept		Interface Friction Angle (degrees)	Adhesion Intercept	
		kPa	psi		kPa	psi
smooth (TPO) membrane / insulation board	24.0	-0.01	-0.001	21.5	0.02	0.003
rough membrane / insulation board	33.8	0.11	0.016	29.0	0.01	0.001
smooth (TPO) membrane / root barrier	8.75	0.72	0.104	10.2	0.03	0.005
rough membrane / root barrier	21.1	-0.03	-0.004	13.4	0.19	0.028
root barrier / insulation board	17.1	0.00	0.00	15.8	0.01	0.001
insulation board / insulation board	19.2	0.32	0.046	18.9	-0.03	-0.004
insulation board / Tremco drain mat & filter fabric	17.0	0.04	0.006	16.3	-0.03	-0.004
Tremco drain mat & filter fabric / loose soil	20.0	0.30	0.044	24.3	0.88	0.128
Tremco drain mat & filter fabric / dense soil	29.2	0.26	0.038	28.6	0.62	0.090

According to Kraupa, the minimum mobilized friction angle for tested ecoroof specimens was 38.5 degrees (Kraupa, Stuedlein, Mason, & Higgins, 2016). As can be seen from the above table, the maximum interface friction angle of the Tremco drain mat & filter fabric/loose soil is 24.3 degrees, while the maximum interface friction of the Tremco drain mat & filter fabric/dense soil is 29.2 degrees. Due to the interface friction angle of the soil being larger than either of the maximum friction angles at the drain mat/soil interface, the soil would be expected to displace as a block. Additionally, as can be seen from , smooth (TPO) membrane/root barrier interface has the lowest interface friction angle for both the

dry and submerged conditions, with coefficients of 8.75 degrees and 10.2 degrees respectively. Consequently, it can be expected that sliding along that interface will occur before sliding on any other interface. In order to ensure that the full-scale tests were conducted according to the most adverse expected design conditions, a TPO membrane and root barrier were selected for use in the full-scale ecoroof.

#### Small Scale Linear Motion Shake Table Testing

In addition to the direct shear interface friction testing, Kilroy also investigated the response of ecoroof sections to earthquake motions, using a small shake table. This testing examined if soil decouples from ecoroofs, and what intensity measures should be used to describe the decoupling. Two saturation states, two soil placements, characterized as "loose" and "dense", and three roof slopes were considered during the testing.

Ecoroof models were subjected to motions with 0.1 g, 0.5 g, 1 g, and 2 g amplitude acceleration pulses, with periods of 0.1, 0.25, 0.5, and 1 seconds. Soil decoupling was measured by comparing the displacement of the soil relative to the displacement of the shake table.

Experimental results indicated that "regardless of the slope of the ecoroof the best soil and moisture conditions to limit soil displacement across all accelerations is the dry, dense condition." (Kilroy, 2015). This finding is in line with expectations because it would be expected that saturated soil would have an increased tendency to flow in comparison to dry soil, while soil particles would be less likely to be held in place for the loose, dry, configuration. Additionally, it was found that dry, loose soil actually underwent larger displacements than submerged soil when larger accelerations (between 762 cm/sec<sup>2</sup> and 1,016 cm/sec<sup>2</sup> depending on roof slope) were present.

After testing was completed, it was determined that velocity was the most accurate intensity measure to be used to describe soil decoupling, and it was found that the greater the velocity, the greater the soil's relative displacement from the table. Acceleration was also considered, however, "clustered displacements uncorrelated to roof slope at low accelerations resolve to expected trends when examined with respect to velocity." (Kilroy, 2015). More specifically, it was also found that soil began to decouple from the roof when roof velocities reached approximately 20 cm/sec (8 in/sec). As mentioned above, soil relative displacement increases relative to table velocity. Moreover, soil relative displacement also generally increased as roof slope increased, as can be seen in Figure A 12 below.

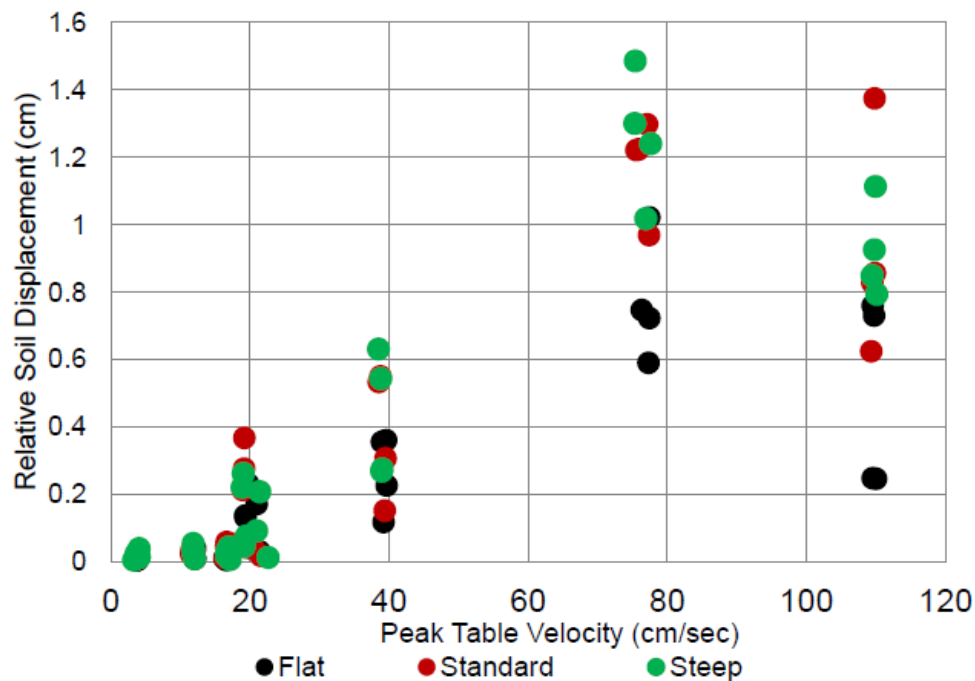


Figure A 12: Relative Soil Displacement vs Peak Table Velocity (from Kim Kilroy's Thesis)

The model ecoroof sections that were tested possessed parapet walls, used to determine the stresses that parapet walls were exposed to during the shaking motions. It was found that the maximum average pressure exerted on the parapet walls ranged from 0.54 psi for a flat roof with dry, dense, soil to 7.37 psi for a steep roof with submerged soil (either dense or loose). Additionally, it was found that the conditions of the roof (soil density, roof slope, and water presence), had a greater effect than the motion applied to the roof. Through the range of motions tested, shown below in **Error! Reference source not found.**, the maximum average pressure exerted on the parapet walls ranged from 4.18 psi to 7.37 psi.

Table A 3: Motion Type and Corresponding Mean and Maximum Average Pressures

Motion	Mean Average Pressure		Maximum Average Pressure	
	(kPa)	(psi)	(kPa)	(psi)
0.1 sec period / 0.1 g acceleration	7.31	1.06	36.75	5.33
0.1 sec period / 0.5 g acceleration	8.76	1.27	38.82	5.63
0.1 sec period / 1 g acceleration	10.89	1.58	39.58	5.74
0.1 sec period / 2 g acceleration	20.06	2.91	50.54	7.33
0.25 sec period / 0.1 g acceleration	5.65	0.82	30.75	4.46
0.25 sec period / 0.5 g acceleration	6.34	0.92	31.37	4.55
0.25 sec period / 1 g acceleration	23.72	3.44	50.81	7.37
0.5 sec period / 0.1 g acceleration	5.65	0.82	30.82	4.47
1 sec period / 0.1 g acceleration	8.83	1.28	28.82	4.18

Finally, in the computation modelling done by Walsh-Huggins and Liel, it was found that increasing the size of structural members corresponding to the added mass due to the ecoroofs appears to compensate for the seismic effects of the additional mass (Welsh-Huggins & Liel, 2016).

## Appendix D – Derivation of Formula Used to Determine Mechanical Strain

Derivation of expression for mechanical strain (strain due to loading)

$$\varepsilon_v = \varepsilon_t + \nu \varepsilon_{mech} \quad (D.1)$$

Where:

$\varepsilon_v$  = strain measured by Poisson gages

$\varepsilon_t$  = strain due to temperature

$\nu$  = Poisson's ratio

$\varepsilon_{mech}$  = mechanical strain due to load

$$\varepsilon_{strain} = \varepsilon_t + \varepsilon_{mech}$$

Where:

$\varepsilon_{strain}$  = strain measured by "strain" gage

Rearranged for  $\varepsilon_t$ :

$$\varepsilon_t = \varepsilon_{strain} - \varepsilon_{mech} \quad (D.2)$$

Substituting equation 3 into equation 1:

$$\varepsilon_v = \varepsilon_{strain} - \varepsilon_{mech} + \nu \varepsilon_{mech} \quad (D.3)$$

Rearranging equation 4 to solve for  $\varepsilon_{strain}$ :

$$\varepsilon_{strain} = \varepsilon_v + \varepsilon_{mech} - \nu \varepsilon_{mech} \quad (D.4)$$

Factor  $\varepsilon_{mech}$  out of the last two terms:

$$\varepsilon_{strain} = \varepsilon_v + \varepsilon_{mech}(1 - \nu) \quad (D.5)$$

Finally, solve for  $\varepsilon_{mech}$ :

$$\varepsilon_{mech} = \frac{\varepsilon_{strain} - \varepsilon_v}{(1 - \nu)} \quad (D.6)$$

